TÉCNICO LISBOA

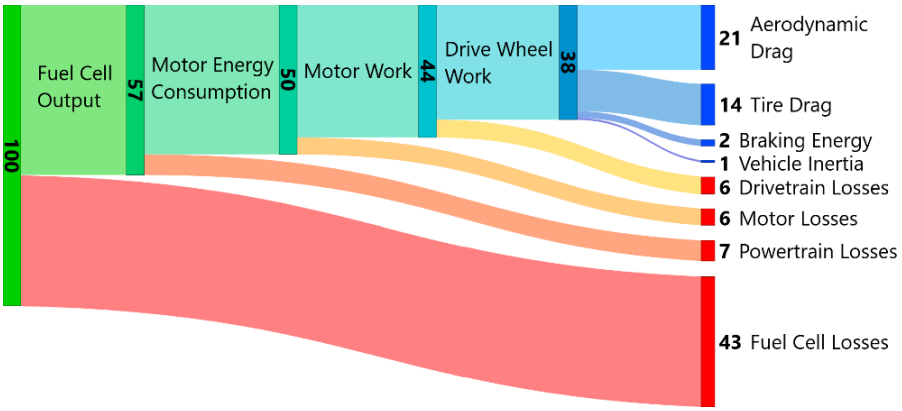

Development of the Powertrain System for a Shell Eco-marathon Fuel Cell Electric Vehicle

António Maria Maia Marques Líbano Monteiro

Thesis to obtain the Master of Science Degree in

Mechanical Engineering

Supervisors: Prof. João Manuel Pereira Dias

Dr. Rui Pedro da Costa Neto

Examination Committee

Chairperson: Prof. Edgar Caetano Fernandes

Supervisor: Prof. João Manuel Pereira Dias

Member of the Committee: Prof. Paulo José da Costa Branco

October 2021

Acknowledgements

Many were the people that helped me in one way or another in my journey through Instituto Superior Técnico. As such, I am grateful to everyone and I would like to personally thank those who helped me during the writing of this thesis:

First, I would like to express my sincere gratitude to Prof. João Dias and Prof. Rui Costa Neto, for their guidance, assistance and unwavering support at every stage of the development of this M.S. thesis.

I would also like to thank Professor Paulo Branco for all the help he gave me and for always being available to discuss new ideas and to answer my many questions on his white board.

I am grateful to all my friends and family for always being there to encourage me and to push me in times of idleness. A big special thanks to Pedro Schvetz and Rafael Prior, with whom I shared part of my time in IST.

I am also very thankful to all the fantastic members of Técnico Fuel Cell, my time in the team as Team Leader and as a member was a unique experience that I will never forget.

I am heartily thankful to my parents for the constant support and patience throughout these years, and to my siblings, Leonor and Manuel, for the encouragement and inspiration.

Finally, I would like to give a very special thanks to my constant companion and partner, Teresa, for always being there for me and for going above and beyond in everything these past wonderful 6 years.

Abstract

Nowadays, the transport sector is highly developed and continues growing; good news for the economy, but a threat to the environment on account of its heavy dependence on fossil fuels. This is where hydrogen can be fundamental in decarbonizing transport as a green fuel for sustainable transport methods like fuel cell electric vehicles.

The main goal of this work is the design of an efficient powertrain for a FCEV as well as the development of a method for generating fuel efficient driving strategies. This work is integrated in a larger student's project called Técnico Fuel Cell that aims to promote alternative ways of sustainable transportation with the design and manufacture of a small urban vehicle to compete in the Shell Eco-marathon, one of the world's most renowned energy efficiency competitions.

The backbone of the work developed in this dissertation is a computational model programmed in MATLAB to accurately simulate the vehicle's behaviour. This model is then used with a genetic algorithm to optimize the powertrain design and the driving strategy, so that maximum fuel efficiency is achieved. With this method, considering a vehicle with conservative specifications, a fuel efficiency of 370.2 km/m^3 of hydrogen was simulated for the competition's 2016 London track – just 5% less than that year's winning result, which was 39% higher than the second place. This result demonstrates the capabilities of the developed optimization method and highlights the importance of such models in the development process of the current and future vehicles of Técnico Fuel Cell.

Keywords: fuel cell electric vehicle; vehicle model; powertrain design; driving strategy; energy efficiency optimization; Shell Eco-marathon.

Resumo

O crescimento do setor do transporte, apesar de positivo para a economia, representa uma ameaça para o ambiente, já que é altamente dependente dos combustíveis fósseis. É neste panorama que o hidrogénio poderá ser fundamental na descarbonização dos transportes, alimentando veículos sustentáveis como carros elétricos a pilha de combustível.

Este trabalho foca-se no desenvolvimento de um grupo propulsor eficiente para um veículo elétrico movido por uma pilha de combustível, bem como na criação de um método destinado a gerar estratégias de condução de baixo consumo de combustível. Este trabalho está integrado na equipa Técnico Fuel Cell, cujo objetivo é promover a mobilidade sustentável através do desenvolvimento e fabrico de um pequeno veículo urbano para competir na Shell Eco-marathon.

A base do trabalho desenvolvido nesta dissertação é um modelo computacional em MATLAB, desenvolvido para simular o comportamento do veículo em torno do circuito selecionado. Este modelo é posteriormente utilizado com um algoritmo genético para otimizar o grupo propulsor e a estratégia de condução para que a máxima eficiência seja alcançada. Com este método, e considerando um veículo com características médias comparativamente com outras equipas, foi simulada uma autonomia de 370,2 km/m^3 de hidrogénio para a pista de 2016 em Londres. Esta autonomia seria apenas 5% inferior à obtida pela vitória desse ano, que foi 39% superior à do segundo qualificado. Este resultado demonstra o potencial do método de otimização desenvolvido e revela a importância de aplicar este tipo de modelos no processo de desenvolvimento dos veículos da equipa Técnico Fuel Cell.

Palavras-chave: veículo movido a pilha de combustível; modelo do veículo; dimensionamento do grupo propulsor; estratégia de condução; otimização da eficiência energética; Shell Eco-marathon.

Table of Contents

List of Figures

List of Tables

List of Abbreviations

BEV	Battery Electric Vehicle
BLDC	Brushless Direct Current
CG	Centre of Gravity
DC	Direct Current
EDLC	Electric Double-Layer Capacitor
EMF	Electromotive Force
EUDC	Extra Urban Driving Cycle
FC	Fuel Cell
FCEV	Fuel Cell Electric Vehicle
GA	Genetic Algorithm
GHG	Greenhouse Gases
HEV	Hybrid Electric Vehicle
ICE	Internal Combustion Engine
IM	Induction Motor
LULUCF	Land Use, Land-Use Change and Forestry
MCCM	Modified Constant Current Model of a BLDC motor
MCDM	Multi-Criteria Decision Making
NCV	Net Calorific Value
OP	Optimization Problem
OS	Optimization Strategy
PEM	Polymeric Electrolyte Membrane or Proton Exchange Membrane
PMSM	Permanent Magnet Synchronous Motor
PSO	Particle Swarm Optimization
RM	Reluctance Motor
SAE	Society of Automotive Engineers
SC	Supercapacitor
SEM	Shell Eco-marathon
SOC	State of Charge
TFC	Técnico Fuel Cell

List of Symbols

Roman symbols

A_F	Frontal area of the vehicle
a_x	Acceleration of the vehicle along its longitudinal axis
b	Longitudinal distance from the front axle to the centre of gravity
B	Motor damping coefficient
c	Longitudinal distance from the rear axle to the centre of gravity
C	Capacitance
C_α	Tire cornering stiffness
C_D	Aerodynamic drag coefficient
D_a	Aerodynamic drag force
d_k	Length of the track section k
e	Projection of the centre of rotation on the vehicle's longitudinal axis
E_{FC}	Energy output of the fuel cell
E_{H_2}	Energy of the hydrogen consumed
E_M	Energy consumed by the electric motor
E_{SC}	Energy stored in the supercapacitor
$E_{SC_{in}}$	Energy input of the supercapacitor
$E_{SC_{out}}$	Energy output of the supercapacitor
F_c	Centrifugal force
f_r	Rolling resistance coefficient
F_r	Wheel rolling resistance force
F_t	Lateral force generated by the misaligned traction force
F_x	Force in the longitudinal direction (tractive force)
F_{xL}	Tractive force of the rear left wheel
F_{xR}	Tractive force of the rear right wheel
F_y	Tire lateral force
F_z	Tire load normal to the road
h	Height of the centre of gravity
i	Iteration number
I	Centre of rotation of the vehicle
I_d	Motor average input current
I_e	Motor current that generates the electromagnetic torque

J	Total moment of inertia on the motor
J_M	Rotational inertia of the motor's shaft
J_t	Rotational inertia of the transmission
J_w	Rotational inertia of the wheels and axles shafts
K_{fp}	Excitation coefficient for the flat section of the phase EMF waveform
k_Q	Commutation impact coefficient
K_t	Motor torque constant
k_ω	Coefficient of decrease in rotational speed
L	Wheelbase
L_s	Phase inductance
m	step commutation number
M	Mass of the vehicle
M_t	Moment generated by the misaligned traction force
N	Number of active sections
N_t	Numerical gear ratio of the transmission
N_w	Number of driving wheels
p	number of pole pairs
P_M	Electrical power of the electric motor
r	Radius of the tires
R	Turn radius
R_x	Rolling resistance force
R_s	Phase resistance
t	Track width
t	Run time at track distance x
t_{lap}	Time duration of one lap
T	Tractive cornering force
T_a	Torque on the axle
T_e	Electromagnetic torque
T_L	Load torque
T_M	Torque output of the motor
T_t	Torque at the transmission
U_d	Motor average input voltage
v	Vehicle velocity
v_f	Velocity of the air flow relative to the vehicle
V_{SC}	Voltage of the supercapacitor

$V_{SC\,max}$	Maximum voltage of the supercapacitor
W	Weight of the vehicle
W_l	Dynamic weight on the front axle
W_r	Dynamic weight on the rear axle
$W_{\theta x}$	Weight of the vehicle along the longitudinal axis
$W_{\theta z}$	Weight of the vehicle along the vertical axis
x	Distance travelled
x_{lap}	Distance of one lap
x_k	Location of the track section k

Greek symbols

α	Wheel slip angle
α_{cond}	Temperature coefficient of resistance of a conductor
α_M	Angular acceleration of the motor's shaft
α_w	Angular acceleration of the wheels
β	Angle that positions the turn centre on the vehicle's longitudinal axis
δ	Ackermann angle (average of the front wheels steer angles)
η_{DCDC}	Efficiency of the DC-DC converter
η_{FC}	Efficiency of the fuel cell
η_t	Efficiency of the transmission
η_{SC}	Efficiency of the supercapacitor
θ	Grade angle of the road
μ_t	Friction coefficient between the tire and the road surface
ρ	Density
ω	Rotor angular velocity
ω_a	Axle angular velocity
ω_M	Motor angular velocity
ω_{nl}	Moto no-load speed

1 Introduction

We live in an age of never-before-seen mobility. It has become so intertwined with our economy and everyday lives that it can be considered as a pillar of modern society. This fact was made clear by the COVID-19 pandemic, which shook and disrupted the economies and lives of people all around the world.

In Europe, as with any sizeable economy, transport is a vital sector for and of the economy. It plays a fundamental role in every other sector by providing goods and services to citizens and businesses, and by allowing workers and raw materials to reach industries across the territory. Transport activity in Europe is very high and still growing, with estimates suggesting that by 2050 passenger and freight transport will increase 42% and 60%, respectively [1]. This is excellent news for the economy but, without real changes to the means of transport we use today, it will pose a serious, if not insurmountable, obstacle for EU's objective of being the world's first climate-neutral[1] continent by 2050.

As can be observed in Figure 1.1, generated with data from [2], the total Greenhouse Gases (GHG) emissions produced in the EU-27+UK have been declining for the past few decades. However, and contrary to the pattern, a steady increase in both mobility sectors[2] has been recorded, namely in the transport sector, which is expected to soon surpass the energy industries as the most greenhouse gases emitting sector of all.

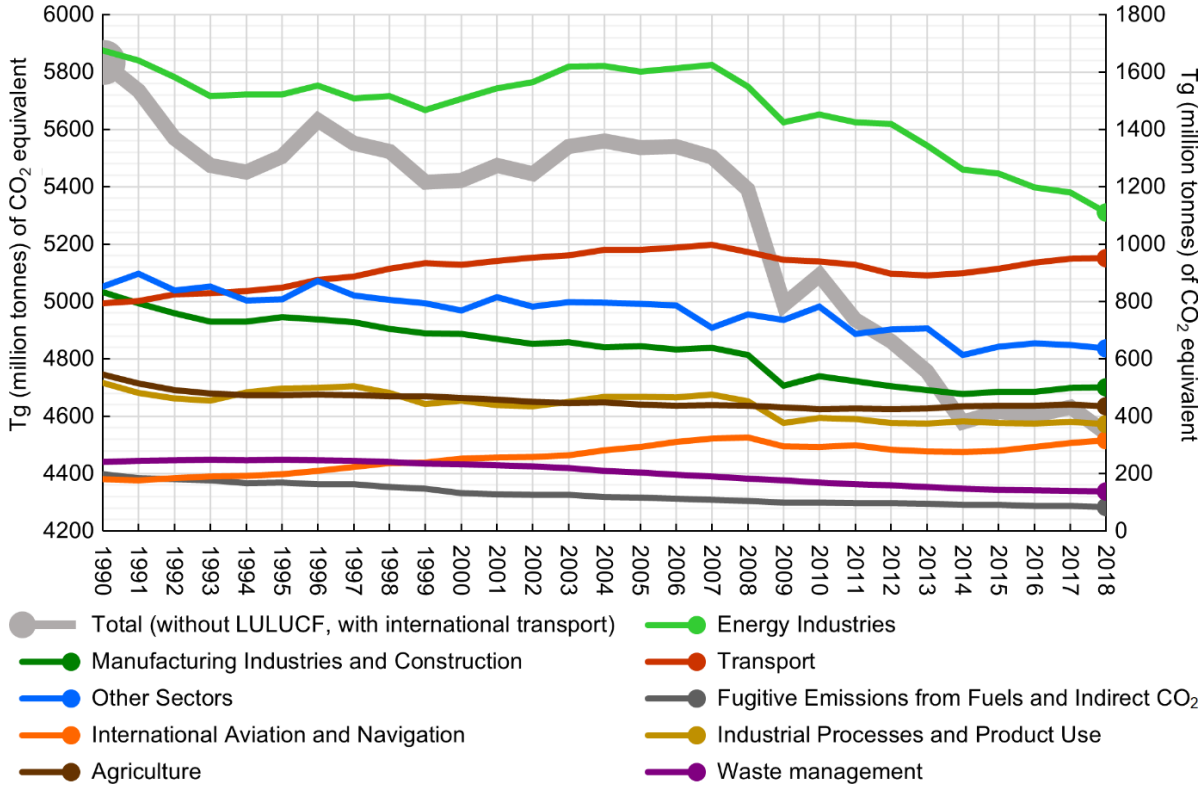

Figure 1.1 - GHG emissions by sector in the EU-27+UK.

[1] The GHG emissions produced are balanced by methods of removing those gases from the atmosphere, be it through carbon capture and storage technologies (CCS) or the planting of new forests.

[2] Transport and international aviation and navigation sectors.

By further inspecting the data from these two sectors [2], Figure 1.2 shows that, in 2018, more than two-thirds (68.7%) of the GHG emissions in Transport (including international aviation and navigation) were caused by road transport alone, and in turn 60.4% of those emissions came from passenger cars.

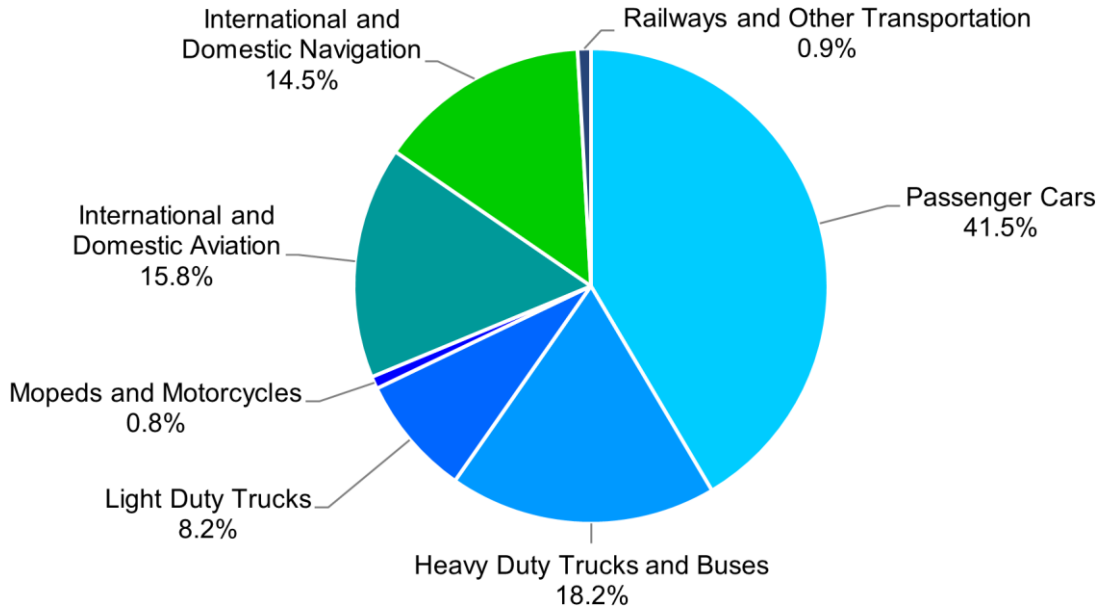

Figure 1.2 - Transport (with international aviation and navigation) GHG emissions in the EU-27+UK, 2018.

The fact that so much of the EU-27+UK's GHG emissions are concentrated, and still rising, in these sectors is worrying due to the ever-increasing demand, but it can also be an opportunity to significantly reduce the emissions if new sustainable technologies are developed and adopted. This is where programs and competitions like the ones behind this master thesis can make a big difference by challenging engineering students to find solutions and answers to the sustainable mobility problem and push forward the limits of green mobility.

1.1 Hydrogen as an Energy Carrier

Hydrogen is the simplest and most abundant element in the Universe. It has one of the highest specific energies of any fuel (around 2.8 times that of gasoline [3]) and can be used to deliver and/or store large amounts of energy, which can be transformed directly into electricity using fuel cells [4]. When produced from renewable energy sources, e.g., solar, wind, hydroelectric, biomass and geothermal, hydrogen is a green fuel that emits only water vapour and heat as a by-product of its use. Hence, it can play a fundamental role in a more sustainable energy supply by decarbonizing transport and industries and also enabling a higher and more efficient penetration of renewable energy sources in the grid by potentially solving the intermittency dilemma of solar, wind and excess energy situations.

It should be noted that hydrogen is considered an energy carrier and not an energy source. This is because it does not typically exist in nature in its molecular form, H_2, and must be produced from compounds that contain it, e.g., electrolysis of water and natural gas reforming.

1.2 Global Context

The work developed in this master thesis is a fundamental part of a bigger project; the design, development and manufacture of a hydrogen fuel cell vehicle. The project first appeared as a challenge made by Professor João Dias to a group of students from Instituto Superior Técnico and resulted in the creation of the team called Técnico Fuel Cell. The challenge also aimed to create a hub of knowledge and talent for both the students and university in a time of great interest and investment in hydrogen and fuel cell technologies. So far, other than the present work, two more thesis were developed by former team members dedicated to the project: one on the vehicle suspension system [5] and the other on its aerodynamics and structural frame [6].

The present thesis is integrated in the Powertrain Department of TFC and its scope is the development of the vehicle's powertrain system, i.e., the analyses of the forces, energy needs, constraints and all the other factors relevant to the design and selection of the components and the architecture of the systems.

1.2.1 Técnico Fuel Cell

The TFC team was formed in early 2019 when a group of about 15 Mechanical Engineering students answered the mentioned challenge and gave the first steps to make the team known and recognized by IST. As the team evolved and the ideas of what was to be accomplished began to take shape, the team became officially recognized as TFC - Técnico Fuel Cell and its main goals were established:

1. The design, development and manufacture of an urban concept electric vehicle powered by a hydrogen fuel cell, to participate in sustainability and efficiency competitions, namely the Shell Eco-marathon (SEM);
2. To make Técnico Fuel Cell a household name of our institution in the fields of efficient and sustainable mobility and hydrogen fuel cell technologies;
3. And finally, to assemble a team of talented and ingenious students that inspire others to join the project, refreshing the team's talent pool and giving it continuity year after year.

As of the time of the writing of this master thesis the team is composed of 22[3] students from different courses and years (Figure 1.3), that cooperate in a joint effort to make Técnico Fuel Cell's dreams and vision become a reality.

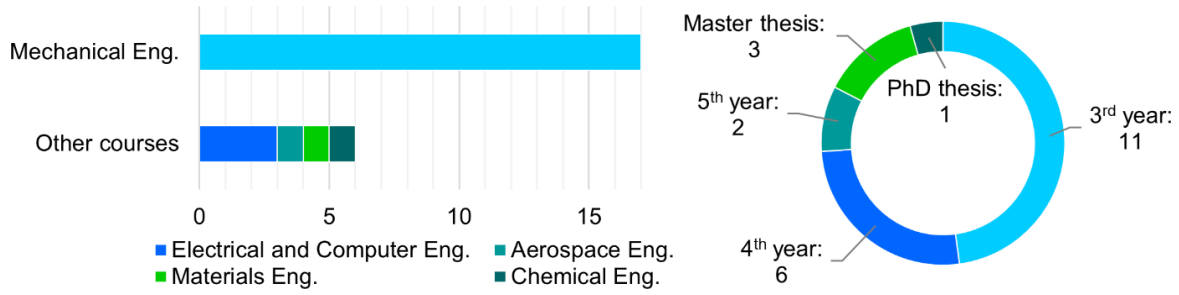

Figure 1.3 - TFC's student distribution by course and year.

[3] 15/01/2021

1.3 Shell Eco-marathon Competition

Shell Eco-marathon is one of the world's most renowned energy efficiency competitions. It is a unique global programme where teams of students of science, technology, engineering and maths build their own vehicles and compete against similar teams for the highest energy efficiency.

All teams must strictly adhere to the Shell Eco-marathon's rules and regulations to design and build their cars for the competition. The rules are updated every year and contain all the technical specifications, safety requirements and information on energy categories and vehicle types, among other things.

In this master thesis, the 2021 Official Rules [3] will be followed. The most relevant regulations to take into consideration during the development of a hydrogen urban concept are compiled in Appendix A.

1.3.1 Vehicle and Energy Types

To compete, participants must select one from two different vehicle classes and three energy categories.

The classes (Figure 1.4)**:**

- Urban Concept – Closer in appearance and functionality to modern passenger cars, these vehicles are larger than the Prototypes, but are also lightweight and very efficient. Vehicles in this class have four wheels that must be in constant contact with the road and are equipped with several auxiliaries common to road vehicles, e.g., lighting system, windscreen wipers, etc.
- Prototype – Very small, ultra-lightweight and highly aerodynamic, these vehicles are designed to achieve the highest efficiencies. Vehicles in this class usually have only three wheels.

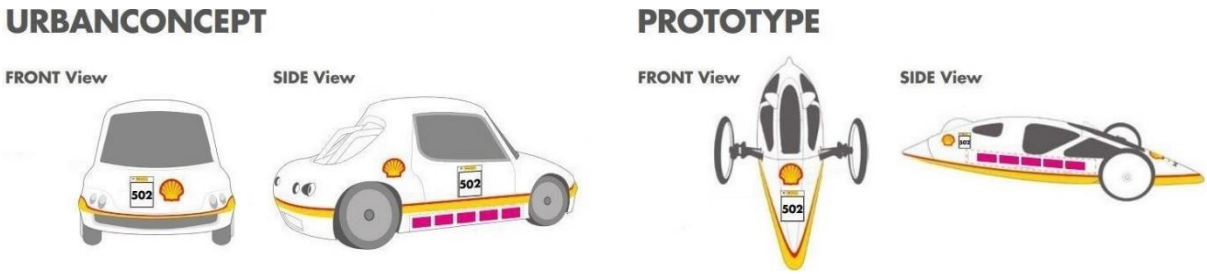

Figure 1.4 - Shell Eco-marathon vehicle classes, adapted from [3].

The energy categories:

- Internal combustion engine powered by gasoline, diesel or ethanol.
- Battery-Electric
- Hydrogen Fuel Cell

1.3.2 Competition Format

The main Shell Eco-marathon competition format is "The Mileage Challenge", which is where the work developed in this thesis will be focused on. The goal is to achieve a valid run using the least amount of energy and, for Urban Concepts, the challenge is also focused on "stop and go" driving. Therefore, vehicles competing in this class are required to do a full stop per lap and resume driving, unaided.

The “Driver’s World Championship” is a competition for the most energy-efficient Urban Concept vehicles from all regions. This challenge is a more traditional “race”, where each competing vehicle is given a limited amount of fuel based on its Mileage Challenge results and must be the first to cross the finish line to win.

1.3.3 Race Track

The Shell Eco-marathon Europe main event often changes location from one year to the next. The track routes are usually completely different from year to year and are only revealed weeks before the competition day. For this reason, it is impossible to know which circuit the team’s vehicle will have to face and, consequently, what the powertrain will have to be capable of. To tackle this uncertainty, the London 2016 route shown in Figure 1.5 was selected, as it is one of the most demanding circuits of the last few competitions, guaranteeing that the vehicle will be capable of handling any race track given.

Figure 1.5 - London track map (SEM Europe 2016) [7].

To achieve a valid run, the vehicle must complete 8 laps around the 2244 metres long track in under 43 minutes, stoping once per lap as is stated in the rules for the Urban Concept class.

The track elevation is also provided, which is a valuable piece of information to accurately model the vehicle’s performance and energy consumption. It can also be used to develop an optimized driving strategy to go around the track more efficiently. The track elevation map is shown in Appendix B.

The final results of the 2016 competition for the Urban Concept Hydrogen class, in the track shown, are displayed in Table 1.1. These will be the main results used for comparing the simulated energy consumption achieved by the vehicle model developed in this thesis.

Table 1.1 - Final results: Urban Concept Hydrogen (SEM Europe 2016), adapted from [8].

Rank	Team n°	Team name	Country	Organization	Competition category	Energy type	Best attempt (km/m3)
1	601	La joliverie Polytech Nantes	France	Polytech Nantes	UrbanConcept	Hydrogen	389.3
2	607	Smart Power Urban	Poland	Silesian University Of Technology	UrbanConcept	Hydrogen	280.9
3	612	Green Team Twente	Netherlands	University Of Twente	UrbanConcept	Hydrogen	268.1
4	602	TUS Team	Bulgaria	Technical University Of Sofia	UrbanConcept	Hydrogen	229.2
5	605	HIDROIST	Turkey	Istanbul University	UrbanConcept	Hydrogen	195.9
6	606	HAN Hydromotive	Netherlands	Hogeschool Van Arnhem En Nijmegen	UrbanConcept	Hydrogen	181.2
7	608	ENSEM-ECO-MARATHON	France	Ensem Vandoeuvre-Les-Nancy	UrbanConcept	Hydrogen	145.4

1.3.4 Energy Conversions

As mentioned in the powertrain competition rules in Appendix A, for non-purely electric vehicles, it is necessary to convert the consumption of different energy types to be able to present a coherent global consumption result for the vehicle's energy efficiency. It is also sometimes useful to compare the energy consumptions of the different energy categories. This is done by converting the energy consumptions to km/L of gasoline equivalent, using the Shell FuelSave Unleaded 95 Gasoline NCV (Table 1.2).

Table 1.2 - Net Calorific Value of the different SEM fuels [3].

Energy Type	NCV by Mass [kJ/kg]	Fuel Density* [kg/L]
Shell FuelSave Unleaded 95 Gasoline	42900	0.7646
Hydrogen (H_2)	119930	8.380×10^{-5}

*At 15 ºC and 1 atm.

For example, to convert a hydrogen fuel consumption in km/m^3 of hydrogen to km/L of gasoline equivalent, equation (1.1) is used:

$$Fuel\ Cons.\,(km/L) = \frac{Fuel\ Cons.\,(km/m^3)}{1000} \cdot \frac{\rho_{Gasoline} \cdot NCV_{gasoline}}{\rho_{Hydrogen} \cdot NCV_{Hydrogen}} \tag{1.1}$$

where required values for density, ρ, and for NCV are given in Table 1.2

1.4 Objectives

The work developed in this master thesis has four major goals: the development of a complete and detailed model of the vehicle from the fuel cell to the wheels that can be used to accurately simulate its behaviour on a track; the selection/creation of an effective strategy to control the vehicle's velocity on a circuit and to use that strategy to develop a highly fuel-efficient driving strategy around the selected track, using a heuristic optimization algorithm to reach an optimal solution; to use all the knowledge and tools previously developed to design the best and most efficient powertrain possible, to select the optimum fuel cell and electric motor for the vehicle, and also to provide all the data needed to select other components, e.g., supercapacitor and transmission, and to build the powertrain; lastly, to use the final vehicle model to study the sensitivity of the fuel consumption to the change of several parameters,

e.g., vehicle mass, efficiency of components, quality of the tires, etc, to highlight where the focus should be on to further optimize the vehicle in future works.

To achieve the proposed objectives and to ensure that the best decisions are taken so that the results and conclusions drawn from the work are as close to reality as possible, a comprehensive study is developed around the following points: the powertrain and its main components; the technical solutions used by other SEM teams; and on the subject of vehicle dynamics.

1.5 Thesis structure

Following the present introductory chapter, where the global context of the project, the competition and the objectives of the present work are discussed, the dissertation is organized in five more chapters.

The second chapter presents a brief study of the technologies behind the powertrain of a hydrogen fuel cell vehicle, as well as a review on the technical solutions used by other teams competing in SEM;

The third chapter gives a deep understanding on all the principles and equations behind the forces acting on the vehicle; the tractive force and the three resistive forces (rolling resistance, grading force and aerodynamic drag). Two models are also introduced, one for the tire drag when cornering and the other to estimate the energy consumed by the electric motor (where the motor technology is also selected). All the principles, equations and models presented in this chapter are used in the original models developed in later chapters of the thesis.

The fourth chapter describes in detail the models developed in this work, starting with all the assumptions used. Of the three models described, one is for the vehicle dynamics (motor to wheel model) and simulates the behaviour of the vehicle on the track and estimates the energy consumption of the electric motor; the other two are for the powertrain (fuel cell to motor models) and simulate the energy flow in through the powertrain components to estimate the hydrogen consumption of the fuel cell. The control strategy required to operate the more complex of the powertrain models (the parallel active hybrid) is also described in its assigned section.

The fifth chapter describes the optimization of the driving strategy, the powertrain design and also presents a sensitivity analysis study of the fuel efficiency in relation to selected parameters. The chapter starts with the optimization problem formulation followed by the optimization strategy and algorithm used to solve it; afterwards, a comprehensive analysis on several design aspects of the powertrain is done to reach the final powertrain design, which is then used to calculate the final optimized driving strategy. Having the optimized driving strategy, the final fuel consumption is validated in comparison to a generic average velocity strategy and then is compared to the official results obtained by other teams in SEM. The chapter ends with a sensitivity analysis study on the following parameters: vehicle mass, quality of the tires, temperature of the motor and the efficiencies of the DC-DC converters and supercapacitor.

The final chapter presents the main conclusions drawn from the work developed in this thesis, also summarizing achievements and failures of relevance. Finally, recommendations are given to further optimize the vehicle's fuel efficiency and on how to improve the fidelity of the models for future work.

2 Technology & State-of-the-art Review

This chapter will focus on the basic principles and knowledge critical to the quality and the scientific rigour of the work developed in the thesis. The first and second sections of the chapter are focused on the powertrain's main components, as well as the possible configurations that they can assume, while the third discusses the drivetrain components. On the last section, several thesis and articles from other Shell Eco-marathon teams will be reviewed in an attempt to identify the state-of-the-art technologies and methods behind the vehicles that our team will compete against.

2.1 Powertrain Key Components

The powertrain of a vehicle encompasses every component that converts the power from a source, e.g., hydrogen fuel cell, battery or engine, into movement. More precisely for a hybrid FCEV, the main components are the fuel cell, the electric motor, the supercapacitor, the DC/DC converters and finally the drivetrain, which includes every other component from the transmission to the driving wheels.

In the following sections, a brief analysis of the fundamentals and state-of-the-art of each of these components will be presented. The drivetrain key components will be briefly discussed in a separate section and, for that reason, will not be included below.

2.1.1 Fuel Cell

A fuel cell is an electrochemical device that converts the chemical energy of a fuel directly into electrical energy and heat. Its operation is similar to an electrochemical battery, however, unlike a battery the energy storage and power are not in the same volume, as the reactants are fed into the cell and, as long as fuel is provided, it can produce electrical power uninterruptedly, as is exemplified in Figure 2.1.

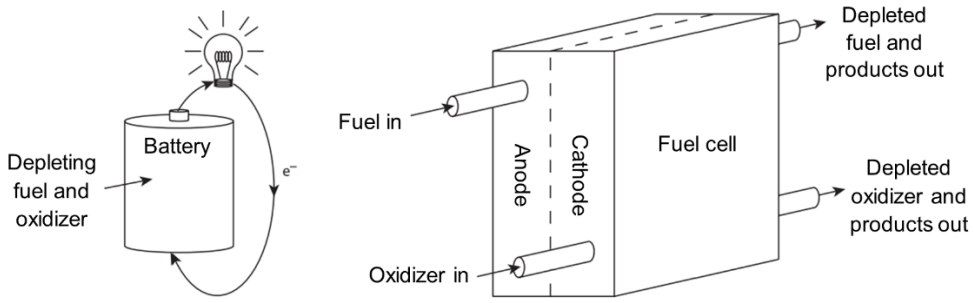

Figure 2.1 - Basic comparison of a battery and a fuel cell, adapted from [9]

There are many different fuel cell technologies, e.g., polymer electrolyte membrane fuel cell, alkaline fuel cell, solid oxide fuel cell, among others [9], yet the general working principle and main components are basically the same: the fuel, most commonly hydrogen, is supplied to the anode, where it releases electrons under the catalyst and the oxidizer, generally oxygen from air, is fed to the cathode where it combines with the fuel's electrons and positive ions, completing an oxidation-reduction reaction.

The electrons, under the potential difference created by the two electrodes, flow through the external circuit generating the DC current, whereas the positive ions pass directly through the electrolyte to the cathode. A detailed schematic of a generic fuel cell is shown below in Figure 2.2.

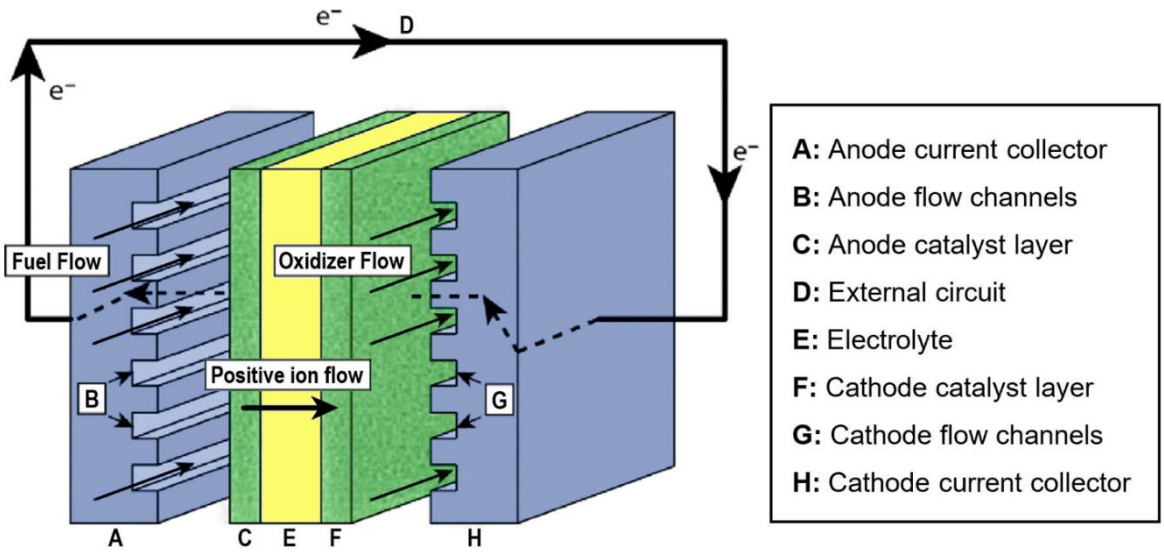

Figure 2.2 - Schematic of a generic fuel cell, adapted from [9].

The overall redox is divided into two semi-reactions that take place on physically separate locations, the oxidation on the anode and the reduction on the cathode. For a hydrogen fuel cell the redox semi-reactions are as follows:

oxidation reaction of hydrogen at the anode:

$$H_2 \leftrightarrows 2H^+ + 2e^- \qquad E_a^0 = 0\ V \tag{2.1}$$

reduction reaction of oxygen at the cathode:

$$\frac{1}{2}O_2 + 2H^+ + 2e^- \leftrightarrows H_2O \qquad E_c^0 = 1.23\ V \tag{2.2}$$

Therefore, the overall redox reaction is:

$$H_2 + \frac{1}{2}O_2 \leftrightarrows H_2O \qquad E^0 = 1.23\ V \tag{2.3}$$

where E^0 represents the theoretical potential of the electrochemical cell based reaction at equilibrium, or also the maximum the reversible open-circuit voltage of the cell, calculated at 25 ºC and 1 atm [10].

The cell voltage-current curve, known as polarization curve, is given by the equilibrium potential, diminished by irreversible losses, often referred to as the overvoltages or polarizations. The typical curve, including the major irreversible losses, for a hydrogen PEM fuel cell is shown in Figure 2.3.

The cell voltage E can be written as in Eq. (2.4), when it is connected to an external load R.

$$E = E^0 - [(\eta_{ct})_a + (\eta_c)_a] - [(\eta_{ct})_c + (\eta_c)_c] - iR_i = iR \tag{2.4}$$

where:

$(\eta_{ct})_{a,c}$ = activation polarization or charge-transfer overvoltage, at the anode and cathode;

$(\eta_c)_{a,c}$ = concentration polarization at the anode and cathode;

i = operating current of cell on load;

R_i = internal resistance of the cell.

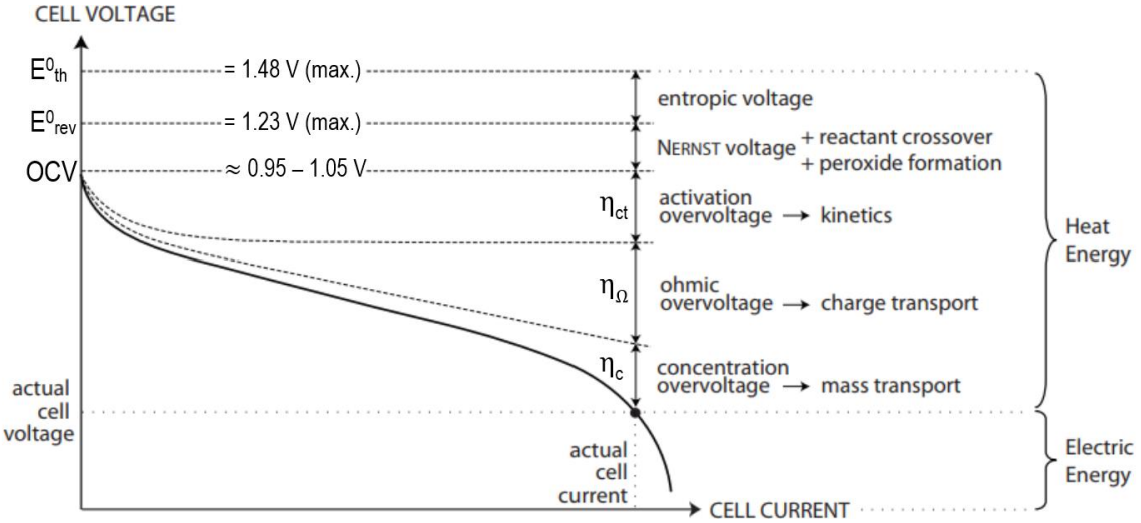

Figure 2.3 - Polarization curve of a hydrogen PEM fuel cell, with major loss contributions. The "actual" cell voltage and current are for nominal power output, which in a fuel cell is often near its maximum power output.

Theoretically, a single fuel cell is capable of achieving any required current and power by simply increasing the size of the active electrode area and reactant flow rates. However, the voltage produced by a single cell is limited by the electrochemical potential of the reacting species which, for realistic operation conditions, is always lower than 1 V [9]. To solve this, several individual cells are connected in series to achieve higher voltages, forming a stack like the one illustrated in Figure 2.4. For this configuration, the total current of the stack is proportional to the active electrode area of each cell and the total voltage is the sum of the individual cell voltages.

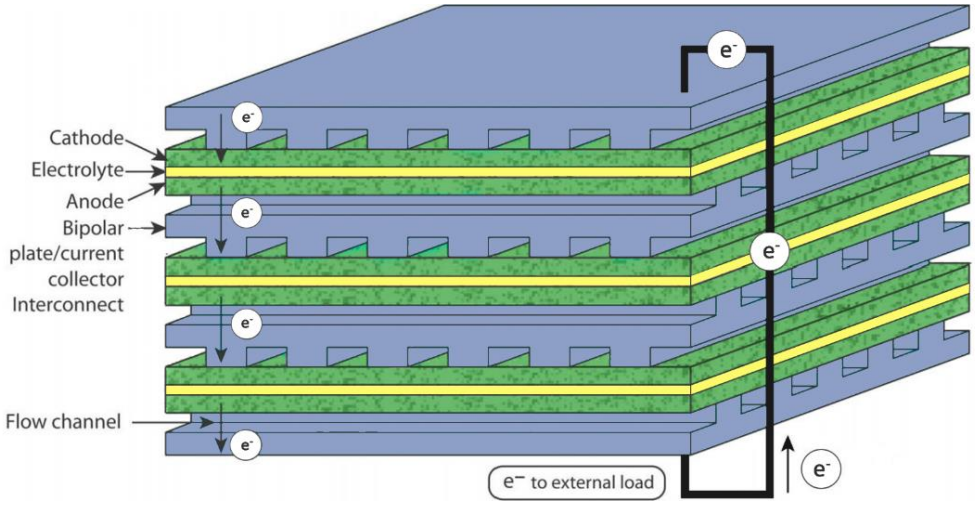

Figure 2.4 - Schematic of a fuel cell stack in series configuration, adapted from [9].

By far, the most common fuel cells used today are of the polymer electrolyte membrane technology (PEM). This is especially true in the mobility sector, where the characteristics of PEMFC's make them an attractive choice for vehicles and other portable applications.

Some of the key advantages and disadvantages of PEMFC's are listed below:

Advantages

- Solid electrolyte – there is no risk of leakage;
- Low operating temperature (under 100 ºC) – safe and easily installed on a vehicle;
- High efficiency (40% to 60%) over a wide range of ambient temperatures (-20 ºC to 70 ºC) with new advances aiming to push the efficiency to higher levels;
- Rapid start-up – low warm-up time before being fully operational;
- High specific power – compact system;
- Good transient response;
- Extremely low recharge time (< 5 min);
- Near zero CO_2 emissions regarding the system and its operation.

Disadvantages

- The membrane must be kept hydrated – poor hydration will lead to membrane deterioration and ultimately cell degradation;
- Uses platinum on the catalyst – makes the fuel cell sensitive to poisoning from trace amounts contaminants like CO and ammonia;
- Requires the use high purity hydrogen (above 98%);
- Difficult cold-start in low temperature conditions;
- Absence of refiling stations makes the implementation in transportation very difficult.

2.1.2 Electric Motor

Electric motor-driven systems are responsible for more than half of the electricity consumed globally in all end-use sectors (buildings, industry, transport and agriculture) [11]. The end-use distribution of final electricity consumption in 2014 can be seen in Figure 2.5.

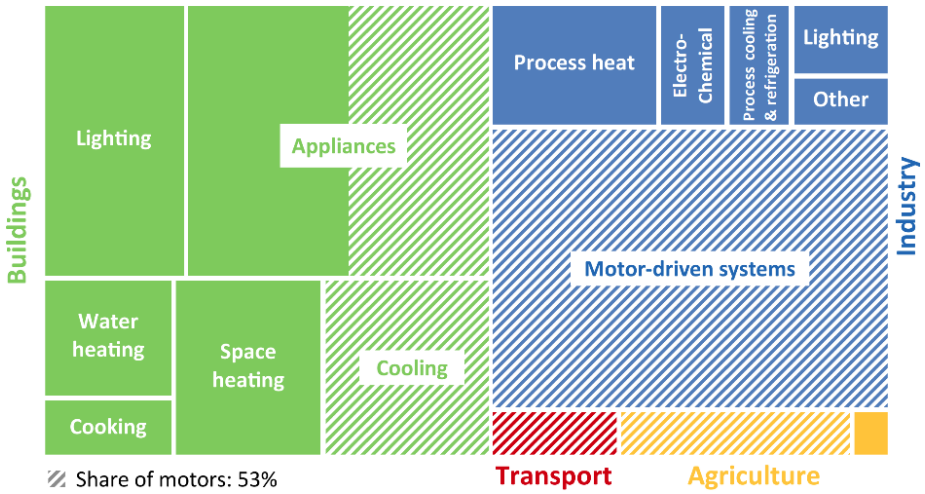

Figure 2.5 - Global total final electricity consumption by end-uses, 2014. Image from [12]

Of all the types of electric motors technologies available, the most common and widely used are the induction motors (IM), also known as asynchronous motors. However, in more recent years permanent magnet motors (BLDC – Brushless Direct Current and PMSM – Permanent Magnet Synchronous Motors) have been increasing in popularity. This is especially true in the automotive sector, where in 2019 82% of electric vehicles used permanent magnet motors, increasing from 79% in 2015 [13].

PMSM and BLDC motors are basically the same, the only difference lies in the distribution of the windings on the stator and the resulting sinusoidal or trapezoidal back EMF[4] (Electromotive Force) and phase current. The output torque of a sinusoidal motor is smoother than that of a trapezoidal motor, however, this comes with an added cost, the PMSM needs more copper for the windings and requires a considerably more complex controller, making it fairly more expensive than the BLDC motor.

The brushless DC motor is often grouped with the ordinary brushed DC motor, not only because both use a DC supply, but also their speed/torque characteristics are very similar [14], [15]. However, this name can be deceiving because a BLDC is actually an AC motor, where the DC supply is converted to an alternating current of variable frequency in an electronic commutator. Hence, this type of motor is also called "electronically commutated motor" or "self-synchronous AC motor", among other names.

The main advantages of BLDC motors are discussed below in higher detail. It should be noted that, apart from the "ease of control", all these advantages are the same, if not better, for PMSM:

Advantages

- Very high efficiency – Permanent magnet motors are among the most efficient of all electric motors [16]. This results from the use of permanent magnets for excitation, which consume no power, and the absence of mechanical commutators and brushes that cause friction losses. Between the PMSM and the BLDC motor, the first can achieve slightly higher efficiencies because it has a smoother torque and suffers no losses due to torque ripples;
- High power density – With the recent introduction of the high-energy-density rare-earth magnets[5], it became possible to achieve higher torques, increasing motor power without increasing the weight;
- Ease of control – The control of a BLDC motor is very simple. The PMSM, on the other hand, needs a considerably more complex and expensive controller;
- Ease of cooling – Since there is no current circulating in the rotor of a permanent magnet motor, it does not heat up. The majority of the heat produced by the motor is on the stator, which is easy to cool because it is static and on the motor's periphery. Furthermore, considering that the motor has a high efficiency, less energy is lost as heat and so the cooling needs are lower than other less efficient motors;
- Low maintenance, great longevity and reliability – The absence of brushes or other mechanical commutators eliminates the need for regular maintenance and reduces the risk of failure associated with these elements. Since there is no wear of any parts other than the bearings, the longevity is limited only by winding insulation, bearings and magnet life length.

The only major disadvantage of BLDC motors is their higher cost, compared to other motors of the same power. This results from using expensive rare-earth magnets, e.g., neodymium and samarium-cobalt magnets, in the rotor and higher manufacturing costs [17]. However, comparing a BLDC motor operating in combination with an electronic commutator with an induction motor controlled with an inverter, if energy efficiency is taken into account, the BLDC motor can be the cheapest of the two options [18].

[4] Back Electromotive Force is a voltage generated on the stator windings by the rotor's magnetic field that opposes the main voltage supply, according to Lenz's Law. The three main factors that affect it are the angular velocity of the rotor, the magnetic field generated by the rotor magnets and the number of turns in the stator windings [17].

[5] Rare-earth magnets are powerful permanent magnets made from alloys of rare-earth elements. First developed in the 70s and 80s, rare-earth magnets are the strongest type of permanent magnets known, typically two or three times stronger than the regular ferrite or ceramic magnets. The name "rare-earth" can be misleading, as some of these metals can be as abundant in the earth's crust as tin or lead.

The basis of operation of BLDC and PMSM motors is the same and is shown in Figure 2.6. The direct current from a DC source is directed to the coils on the stator according to a commutation pattern. In turn, the current passing through the coils generates a magnetic field that attracts or repels the permanent magnet rotor, according to their polarity. To make the torque steady, three or more coils are used, as exemplified in Figure 2.6 (d) for a BLDC motor.

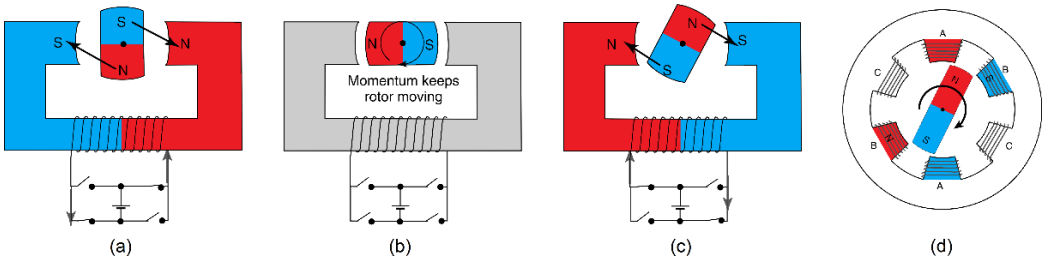

Figure 2.6 - Operation of a single coil of a BLDC motor (a, b, c) and diagram of the arrangement of three coils on the stator (d), adapted from [14].

For BLDC motors to work correctly, the electronic commutator must energize the correct coils at the appropriate time, according to a defined commutation pattern. Since the switching between coils is discrete, it is not necessary to measure the rotor position angle continuously; it is sufficient to determine the time instant when the rotor enters the “sections” where the coils should be switched on or off, which is usually accomplished using hall sensors[6]. On the other hand, for PMSM the control is considerably more complex since it requires the use of sinusoidal alternating currents to energize the windings.

2.1.3 Supercapacitor

Supercapacitors, also commonly known as ultracapacitors, are energy-storage devices characterized by a much higher specific power but a much lower energy density compared to electrochemical batteries. Due to their very high power densities, that can reach up to 5 kW/kg [15], [19], supercapacitors can play a big role in electric and hybrid mobility as a quasi-instantaneous, high-power energy source or sink, namely for acceleration, going up hills and regenerative braking. However, as a result of their low energy densities (10 times inferior than batteries), supercapacitors are not suitable as energy-storage for BEVs and HEVs by themselves and must be used as an auxiliary power source for other energy-storage technologies, such as fuel cells or lithium-ion batteries. The use of such hybrid energy-storage systems enables the decoupling of specific energy and specific power requirements, creating the opportunity to design better and more optimized systems. One perfect example of this is fuel cell - supercapacitor hybrids, where full advantage can be taken of the fuel cell’s very high energy density, with the supercapacitor making up for its lack of power density and inability to store energy on the go. For a better appreciation of the position of fuel cells and supercapacitors, as well as other modern energy-storage devices, according to energy and power density, see Figure 2.7.

[6] Hall Effect Theory: If an electric current carrying conductor is placed in a magnetic field, its charge carriers experience a transverse force which tends to push them to one side of the conductor. This is most evident in a thin flat conductor. This build-up of charge on the side edges of the conductor balances the magnetic influence, producing a measurable voltage across the two sides of the conductor, which is named the Hall effect after Edwin H. Hall who discovered it in 1879 [17].

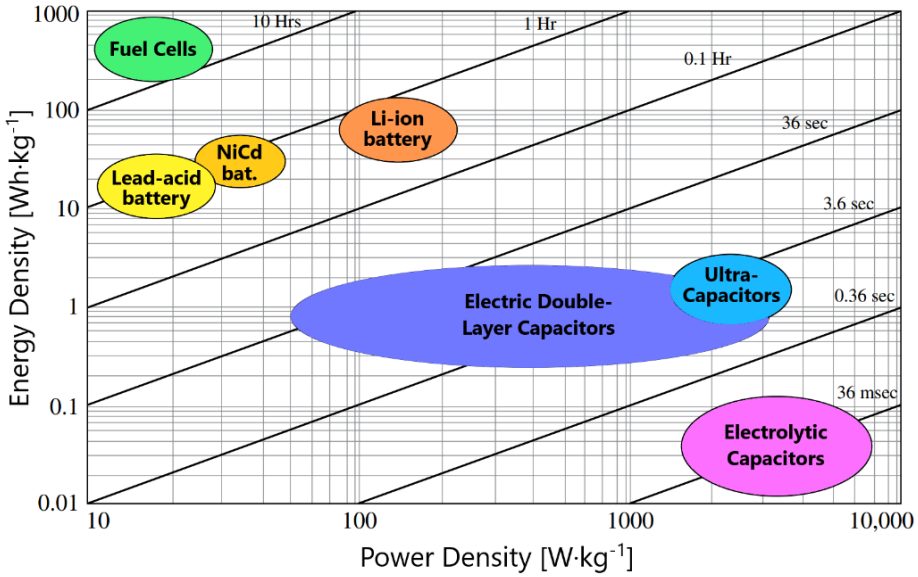

Figure 2.7 - Ragone plot for several modern energy-storage devices, adapted from [20].

The large majority of supercapacitors today use the Electric Double-Layer Capacitor (EDLC) technology [16], [21]. For increasing capacitance, ELDCs normally use thin, porous, often carbon-based electrodes with very high specific surface areas (1000 m^2/g to 3000 m^2/g [16], [22]) which are bathed in a liquid electrolyte instead of being in contact with a solid dielectric material as in normal capacitors. This electrolyte can be either an aqueous or organic based solvent and is the medium through which the ions diffuse. An insulating, ion-conducting membrane (referred to as the separator) is used to separate the electrodes, yet still allow the free movement of the ions in the electrolyte.

In an ELDC, energy is stored via charge separation. When the supercapacitor is subjected to a potential, the electrolyte ions diffuse toward the electrodes and accumulate on the interface between the electrode's surface and the electrolyte, forming the Helmholtz double layers. Most of the energy is stored electrostatically in these layers, where on one side are the accumulated electrolyte ions and on the other the attracted charge of the electrode. The structure of an Electric Double-Layer Capacitor and a diagram of the Helmholtz Double Layer of the electrode-electrolyte interface is shown in Figure 2.8.

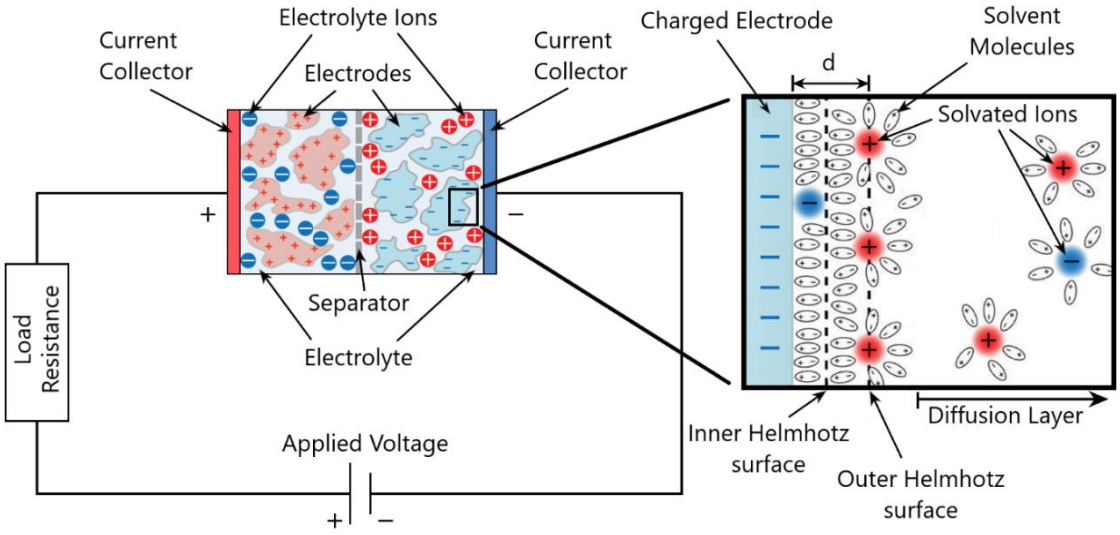

Figure 2.8 - Structure of an ELDC with a diagram of the Helmholtz Double Layer for the negatively charged electrode, adapted from [21], [22].

One of the limiting factors of ELDCs is the electrolyte's low maximum working voltage, above which it eventually starts to decompose chemically, e.g., the water in an aqueous electrolyte starts to decompose into hydrogen and oxygen at voltages slightly above 1.2 V [16]. For this reason, and since the stored energy in a SC is proportional to the square of the voltage, organic electrolytes that offer a wider voltage window (as high as 3.5 V) are universally used in commercially available supercapacitors [23].

The energy stored, E_{SC}, in a supercapacitor can be expressed as equation (2.5):

$$E_{SC} = \frac{1}{2} \cdot C \cdot {V_{SC}}^2 \tag{2.5}$$

where C is the capacitance in Faraday and V_{SC} is the supercapacitor voltage.

Compared to conventional capacitors, the extremely larger energy storage capacities of ELDCs come from the very high capacitances that these devices can reach. This results from the capacitance being proportional to the electrode's huge surface area, as well as it being inversely proportional to the distance between the charges, which can be as thin as one molecule in an ELDC (distance d of Figure 2.8) [16].

Other than the already mentioned high power density, supercapacitors boast several other advantages:

Advantages

- Very high efficiency – Supercapacitors are highly efficient devices, easily achieving efficiencies higher than 95% for a wide range of operating conditions. Since supercapacitors have a very low internal resistance, they produce almost no heat;
- Exceptional cycle life – The energy storage mechanism of a supercapacitor is a highly reversible process. Therefore, it is easily capable of more than a million of charge/discharge cycles with minimal performance impact;
- Improved hybrid operational life – When coupled with other energy-storage devices, supercapacitors can satisfy the transient loads and/or peak power needs, reducing the amount of work of other energy-storage devices and significantly improving their lifespan;
- High flexibility – Supercapacitors have no memory effects, cannot be over-discharged, can be held at any voltage below their rating and can operate at a wide range of temperatures (-40ºC up to +65ºC). If kept within its ranges of voltage and temperature, no maintenance is required.

2.1.4 DC/DC Converter

The advent of power electronics and power semiconductors has enabled the great advances seen in the BEV, HEV and FCEV automotive industry in the last two decades. Today, the use of power electronic converters is widely used in electric powertrains, be it in the form of electric motor controllers, voltage regulators, charging systems, etc. The main function of these converters is to perform the necessary power conversions that maximize the functionality from electromechanical devices, energy sources and electric loads [24]. Since these components are often connected between the powertrain's energy source and electromechanical device, the converter's efficiency directly impacts the overall vehicle efficiency, cooling needs, power demand and cost.

Power electronic converters perform electrical power conversion efficiently by periodically switching the input power on and off in a circuit, using semiconductor devices to act as switches. Energy storage devices, such as inductors or capacitors, are used to smoothen the sharp-edged waveform created by the on-off switching. Modern DC-DC converters can easily achieve efficiencies above 90% [24], [25].

In the powertrain developed in this thesis, other than the motor controller which is basically a DC-AC converter, DC-DC converters are used to change voltage levels as required so the powertrain components can work effectively together, e.g., if the supercapacitor has a maximum voltage of just a few volts, a boost converter is needed to connect it to a higher voltage electric motor. The boost converter is one of the three basic types of DC-DC converters:

Buck converter – Converts power from a high voltage to a lower one;

Boost converter – Converts power from a low voltage to a higher one;

Buck-boost converter – Converts power from an input voltage to a lower or higher output voltage.

If regenerative braking is to be used, the DC-DC converter that is connected to the energy storage unit must be bi-directional to accept current in both directions.

2.2 Powertrain Configurations

There are many different possible configurations for a fuel cell powered powertrain; from the most simple and basic, where the fuel cell is directly connected to the electric motor, to more complex systems that make use of one or more energy-storage technologies that work together with the fuel cell in a hybrid configuration. For the powertrain discussed in this thesis, besides the fuel cell, the only energy-storage technology permitted in the SEM rules (Appendix A) must be of the capacitor type, i.e., a supercapacitor.

This section presents the four main configurations applicable to the vehicle and its intended use; one uses the fuel cell as the sole energy source and three are FC-SC hybrids. All the considered topologies make use of at least one DC-DC converter between the FC and the electric motor to allow for the motor supply voltage to be constant despite the changing voltage of the fuel cell. It should be noted that, if the motor load and fuel cell voltage ranges overlap, the DC-DC converter should be able to operate in buck/boost mode, i.e., it must be able to lower or elevate the output voltage as needed.

The advantages and shortcomings of each configuration are also discussed in this section, including a brief discussion of the expected efficiencies of the four systems. The nomenclature and suggested topologies are based on article [19].

2.2.1 Active FC powered system

The simplest of all the considered topologies is seen in Figure 2.9; it relies on the fuel cell alone to satisfy all the load needs of the vehicle. A single, unidirectional DC-DC converter is used between the fuel cell and the load. This configuration has the advantages of being the most simple and cheap of the options, however, the downside is that there is not much room for optimization. For example, it is impossible to

maintain the power output of the fuel cell constant at its highest efficiency point, independently of the load power needs, and no energy recuperation can be used.

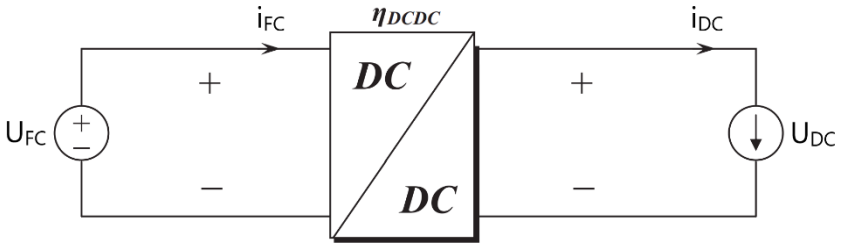

Figure 2.9 - Active FC powered system, adapted from [19].

2.2.2 Semi-active hybrid topologies

In the semi-active hybrid configurations, the fuel cell is used together with a supercapacitor and one DC-DC converter, in three possible configurations. The two of interest (Figure 2.10) for the vehicle's powertrain are:

Parallel semi-active hybrid (case a) – The supercapacitor is used directly connected in parallel to the fuel cell and will act as a buffer to the FC's change in voltage, i.e., if more power is requested from the fuel cell, its voltage will tend to drop according to its polarization curve (example in Figure 2.3) and the supercapacitor will step in, resisting the change in voltage and enabling the fuel cell to work longer near its optimum point. The same is valid opposite case, where the fuel cell's voltage will tend to rise for a drop in the load requested, resulting in the supercapacitor absorbing part of the current from the fuel cell, resisting the change in voltage.

Note: This configuration requires a bi-directional DC-DC converter to use energy recuperation.

Fuel Cell semi-active hybrid (case b) – The supercapacitor is connected in parallel with the load and will act as a load voltage stabilizer. In this case, if the fuel cell is capable of delivering sufficient power to the load and the output voltage of the DC-DC converter is constant, the supercapacitor will do very little in terms of energy storage.

The main disadvantage of semi-active hybrids, compared to the active FC topology, is the added complexity, cost and energy loss of the DC-DC converter.

Other limitation shared by these two configurations is the limited use of the supercapacitor stored energy, since its voltage cannot be freely changed and is determined by terminal voltage of the fuel cell (case a) or the DC-DC converter (case b), which means very little energy from the SC is used.

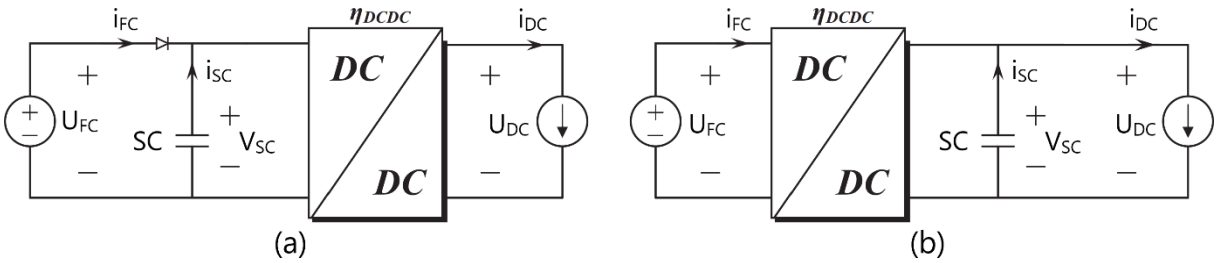

Figure 2.10 - (a) Parallel semi-active hybrid and (b) FC semi-active hybrid, adapted from [19].

2.2.3 Parallel active hybrid configuration

In active hybrids, in addition to the fuel cell and supercapacitor, two DC-DC converters are used in the powertrain, in three possible configurations. Of these, according to A. Kuperman in [19], the parallel active hybrid shown in Figure 2.11 is by far the optimal active hybrid configuration, since it combines the advantages of the other two active hybrids and offers the lowest energy losses of the three. Hence, only the parallel active hybrid topology will be studied as a possible solution for the vehicle's powertrain.

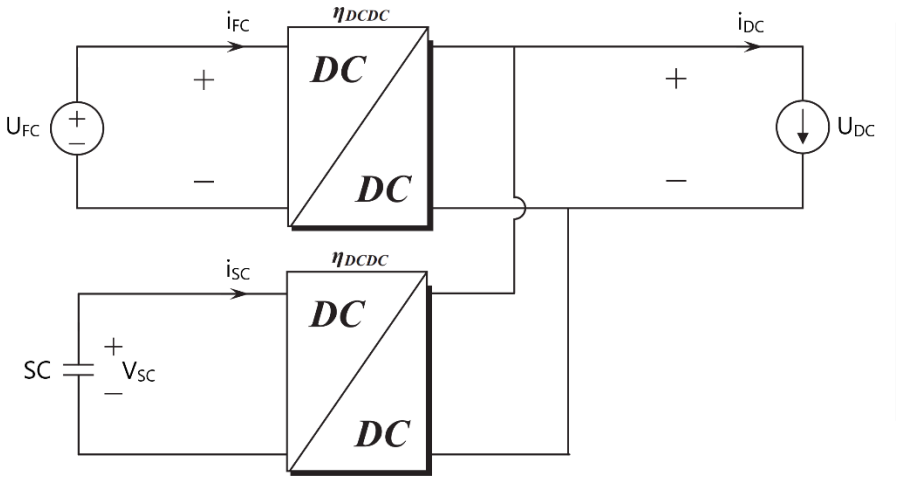

Figure 2.11 - Parallel active hybrid configuration, adapted from [19].

The major advantage shared by all active hybrids over the semi-active hybrids shown, is the much larger supercapacitor voltage operating range, which typically fluctuates between 50% and 100% of its rated voltage, allowing the usage of 75% of the total energy capacity of the supercapacitor. This fact can be easiliy demonstrated with equations (2.6) and (2.7) , developed from Eq. (2.5):

$$E_{SC_{max}} - E_{SC_{min}} = \frac{1}{2} \cdot C \cdot {V_{SC_{max}}}^2 - \frac{1}{2} \cdot C \cdot \left(0.5 \cdot V_{SC_{max}}\right)^2 \tag{2.6}$$

$$E_{SC_{max}} - E_{SC_{min}} = 0.75 \cdot \frac{1}{2} \cdot C \cdot {V_{SC_{max}}}^2 \tag{2.7}$$

The main disadvantage of active hybrids is the use of one extra DC-DC converter, which makes the powertrain considerably more complex, more expensive, and introduces an aditional source of energy loss. However, the advantage of having a lot more energy of the supercapacitor available, allows for the fuel cell to be used almost exlusively at it's maximum efficiency output power, compensating for the other sources of energy loss and possibly even making the parallel active hybrid outperform the other configurations.

2.3 Drivetrain

The drivetrain is an integral part of the powertrain. It comprises the components responsible for the transmission of mechanical power from a source, like an electric motor or engine, to the wheels. In the vehicle developed in this thesis, the transmission, which in itself is composed of several components, the wheel hub and the tires are all included in the drivetrain. All these components are briefly discussed in this section.

2.3.1 Transmission

The transmission is the main mechanical part of the drivetrain, it includes the gearbox, the clutch and the driveshafts. For the vehicle discussed in this thesis, the transmission system can be a combination of a store-bought gearbox connected to roller chains, toothed belts and/or purposefully made gears, or even an axle with a universal joint. A type of clutch system may have to be used if it is judged that regenerative braking can play a significant role in saving energy and that it should be used in the vehicle.

2.3.2 Freehub

Freehubs are a type of freewheel used in high performance bikes. The main function of this component is to deliver torque in one direction while allowing the wheel to spin freely in the other. There are many different mechanisms used to achieve this, the most common being the pawl-style freehub, like the example shown in Figure 2.12.

Figure 2.12 – Schematic of a pawl-style freehub with four spring loaded pawls.

This type of mechanism is subject to some residual friction while freewheeling due to the contact between the pawls and the outside toothed case, which is what causes the familiar clicking noise these components are known for. There are some more high-end models that use magnets or other more complex mechanisms for engaging and disengaging the hub, which almost eliminate friction while freewheeling. However, these are generally considerably more expensive and harder to find.

In terms of how much torque freehubs can handle, it is safe to assume that they can handle the torque output of the vehicle since professional sprint cyclists can produce torques higher than 200 Nm on the pedals [26], [27] which, after the torque reduction due to the gear ratio, should generate a similar or even higher torque on the hub than what is delivered by motor of the vehicle.

2.3.3 Tires

Tires play a major role in fuel efficiency competitions and can make or break a team's chance of claiming a spot on the podium. For example, in 2014, teams competing in Shell Eco-marathon Americas using the specially designed fuel-efficient Michelin tires won all nine classes of the competition [28]. This has been the trend for the past years, where most of the teams winning the SEM competitions are equipped with Michelin's ultimate energy-efficient tires.

These tires are the perfect choice for any team aspiring to achieve the highest fuel efficiency. If the team cannot acquire or afford these tires, there are other possible low rolling resistance solutions like round or triangular profile tires for mopeds or motorbikes. However, these types of non-flat profile tires can severely affect traction and cornering performance and must be thoroughly tested before being safely used on the track.

2.4 Technical Solutions SEM Teams Use

Since Técnico Fuel Cell is a new team building their first car, it cannot yet rely on past experience for guidance. Therefore, some reports, papers and thesis from other competing teams are reviewed in this section, to have some form of benchmark for the vehicle components, weight and a target for the fuel efficiency it is to achieve. This research is also of high importance to, not only investigate the success of solutions and methods employed by the adversary but, more importantly, to scrutinize where other teams failed to avoid making the same mistakes.

2.4.1 Spiros IV – KTH Royal Institute (2011) [29]

Hydrogen fuel cell Urban Concept with a series hybrid powertrain. It uses a supercapacitor as an energy buffer that allows the fuel cell to work with higher efficiency at moderate power and stores energy produced in regenerative braking. It achieved a 5th place with a fuel efficiency of 59.8 km/kWh (166.9 km/m^3 of hydrogen). The team used the same bullet-shaped body seen in Figure 2.13 for several years.

Driving Strategy – No significant optimization of the driving strategy was done.

Figure 2.13 - Spiros (2008) same body as Spiros IV.

2.4.2 HydRU R3– University of Ruse Angel Kanchev (2018) [30]

Urban Concept with a simple hydrogen fuel cell powered powertrain. It uses two efficient Maxon RE 50 DC motors (200 W) mounted side by side in a fixed-ratio gearbox, in parallel configuration. It achieved a 5th place in SEM Europe with a fuel efficiency of 116.0 km/m^3 of hydrogen. The vehicle has an aluminium chassis and a fibreglass body, seen in Figure 2.14.

Driving Strategy: No significant optimization of the driving strategy was apparently done.

Figure 2.14 - HydRU R3 (2018).

2.4.3 PureChoice - Norwegian University of Science and Technology (2008) [31]

Urban Concept with a very simple hydrogen fuel cell powertrain. The fuel cell provided all the power needed for propulsion and it did not use a supercapacitor, which means no regenerative braking was used. The vehicle, seen in Figure 2.15, was of monocoque construction using carbon fibre and weighed an impressively low 69 kg. It achieved 223.4 km/m^3 of hydrogen, winning a second place.

Figure 2.15 - PureChoice in the 2008 SEM competition.

2.4.4 Fuel Fighter – Norwegian University of Science and Technology (2017) [32]

Urban Concept powered by a 48V Lithium-Ion battery. It uses two Maxon DC motors (RE 50 and RE 65) to power the rear wheels, independently. Each motor is connected to its wheel with a belt drive system of fixed gear ratio.

Driving Strategy: Even though the vehicle has two driving wheels, it works mainly as a 1WD car. The motors are always used independently at 80% of their maximum power, according to the simple average velocity driving strategy described below, in Table 2.1:

Table 2.1 - Driving strategy for the DNV GL Fuel Fighter 2017 vehicle.

Motor	$v \leq 36$ km/h			$v > 36$ km/h
	F_D* > 50 N or initial launch	$F_D \leq 50$ N	Sharp turn or pit stop	
500 W	On	Off	Off	Off
120 W	Off	On	Off	Off

*F_D is the total drag force acting on the vehicle.

Eco-marathon results: Due to a series of vehicle malfunctions the team was unable to achieve a valid result: On the first try, the press fitted nylon pulley of the belt drive system loosened from the hub; on the second, there were troubles with the battery management system and one of the mirrors fell because the adhesive failed; on the third, the controller of the RE65 motor fried; Finally, at the beginning of the fourth and final try, the newly built motor controller malfunctioned and, as a result, the motor produced a large torque and destroyed the pulley and hub mechanism.

The vehicle, seen below in Figure 2.16, has a highly aerodynamic monocoque of carbon fibre.

Figure 2.16 – DNV GL Fuel Fighter (2017)

2.4.5 Smarter – Chalmers University of Technology (2009) [33]

Urban Concept with an ICE series hybrid powertrain. It uses two Maxon RE 65 DC motors (250 W) to power the rear wheels, individually. Both motors can be used for regenerative braking.

Transmission System: A simple two-stage transmission with sprockets and roller chains was used on each wheel to gear down the motor output.

Control System: The ICE was controlled by simply turning it on or off if the supercapacitor's voltage was too low or reached its maximum.

Driving Strategy: No optimization of the driving strategy was studied. The velocity between the required stops was assumed constant, regardless of the track topography.

Eco-marathon Results: No valid results were achieved. For the first try the vehicle was not ready in time. In the second, after two laps, the driver had to do an emergency stop due to under voltage in the supercapacitor, which later was explained by extra load caused by the excessive wobbling of the wheels. The third and last attempt ended on the first lap, when the front left wheel sprung loose from the system.

During the attempts it was observed that it was impossible to maintain a constant velocity, not only were some of the corners too sharp but the track was also shared with multiple teams doing their attempts.

The vehicle is of monocoque construction and was left unpainted to avoid the addition of unnecessary weight, leaving the characteristic criss-crossed pattern of the carbon fibre visible in Figure 2.17.

Figure 2.17 - Smarter during the 2009 SEM competition in Lausitz, Germany.

2.4.6 Elba - KTH Royal Institute (2017) [34], [35]

Urban Concept with an ICE parallel hybrid powertrain. It has the unusual characteristic of having two electric motors, where both the motors and the engine can deliver power to the wheels and only one is used for regenerative braking. One is a Maxon RE 50 DC (200 W) motor and is responsible for the cruising operation, whereas the other, a Dunkermotoren BG 95x80 BLDC motor (1044 W), is responsible for the acceleration of the vehicle and for regenerative braking.

Control System: A hierarchical three-layer optimal control was developed. The top-layer computes the optimal driving strategy in advance, the middle-layer finds the best instantaneous torque split of the three propelling components and the bottom-layer controls component level states according to the torque split defined. The DC motor was always preferred to the BLDC, as it was assumed it is more efficient in all working conditions, which may be untrue.

Driving Strategy: An optimization of the driving strategy was developed. The topography information of the track was used to generate an optimal velocity profile and to take advantage of opportunities to recharge the supercapacitor from the ICE and/or regenerative braking, while running downhill.

Eco-marathon results: Due to failure of a component in the engine during the 6th lap, no valid attempt was possible. However, with the new improvements made to Elba, the fuel consumption was expected to improve by up to 50%, when comparing to 2015, where the team was able to secure a 7th place with a fuel consumption of 95.6 km/L.

The Elba (Figure 2.18), is the successor of the Spiros car discussed in Section 2.4.1. Its lines are more curved than the Spiros and the rear of the vehicle ends in a less abrupt way, improving its aerodynamics.

Figure 2.18 - Elba during the 2017 SEM Europe competition.

2.4.7 Green Team Twente – University of Twente [36]

One team that has been excelling for the past few years, in the hydrogen fuel cell Urban Concept class, is University of Twente's Green Team Twente. It has won one World Championship, three first places and two third places. The vehicles that achieved the wins are presented in Table 2.2, the last shown in Figure 2.19. Unfortunately, other than the weights and efficiencies, no further information was found any of the team's vehicles.

Table 2.2 - Winning vehicles of Green Team Twente [36].

Vehicle	Year	Awards Won	Weight [kg]	Fuel Efficiency	
				[km/m^3][1]	[km/L][2]
Aurora 2	2018-2019	WChamp, 1st	106	242.5	791.5
H2 Infinity	2016-2017	1st	114	277.8	906.7
H2.Zero	2015-2016	3rd	114	268.1	875.0
UTmotive	2012-2013	3rd	85	245.1[3]	800[3]
	2011-2012	1st	100	209.4[4]	683.4

[1] Official energy efficiency result.
[2] Kilometre per litre of gasoline equivalent.
[3] Taken from the team's website.
[4] Converted from km/kWh, which were the units used at the time.

Figure 2.19 - University of Twente's AURORA 2, taken from the team's website [36]

2.4.8 Discussion

A compilation of the main traits of relevance from the vehicles discussed in the previous sections is presented in Table 2.3. The main characteristics considered are the powertrain class and configuration, electric motor type and power, if it can use regenerative braking and vehicle weight (without driver).

Table 2.3 - Powertrain characteristics of Urban Concept vehicles.

Team	Energy Class	Hybrid	Motor Type	Power [W]	Regen.	Weight [kg]
Spiros IV	Hydrogen FC	Yes	BLDC	500	Yes	135
HydRU R3	Hydrogen FC	No	2 x DC	2 x 200	No	130
Purechoice	Hydrogen FC	No	-	-	No	69
Fuel Fighter	Battery	No	2 x DC	200 + 250	No	90
Smarter	ICE	Series	2 x DC	2 x 250	Yes	74
Elba	ICE	Parallel*	DC+BLDC	200 + 1044	Yes	90

*The Internal Combustion Engine can also provide mechanical power to the wheels.

In the review of the literature on the other SEM vehicles and with the information compiled in Table 2.3, the following observations were done:

- From the five vehicles that the electric motors used were known, only one did not use a DC motor, using instead a BLDC motor of 500 W while the other four vehicles all used Maxon DC motors (known for being the most efficient DC motors in the market), often two of different powers (the RE 50 DC – 200 W and the RE 65 DC – 250 W). Another interesting observation is that all the four vehicles that opted to use DC motors used two motors, which is probably due to the fact that the DC motors used do not have enough power for the vehicle alone;
- From all the electric vehicles, which includes hydrogen FC, only the one with the sole BLDC motor used regenerative braking since all the others were not hybrids, i.e., did not have any energy storage devices. Both the ICE hybrids used regenerative braking;
- The average power of the vehicles that have electric propulsion only (Elba is not included) and the motor power is known, is approximately 463 W;
- The average weight of the investigated vehicles is 106 kg, with values ranging from 69-135 kg;
- Finally, the average fuel efficiency of the three hydrogen fuel cell vehicles found on the literature was 168.8 km/m^3, while the average of the Green Team Twente's vehicles was considerably higher at 248.6 km/m^3.

3 Vehicle Dynamics and Motor Model

The subject of “vehicle dynamics” is the study of the movements of vehicles on a road surface, where the motions of interest are acceleration, braking, ride and turning. The dynamic behaviour is determined by studying the forces that are imposed on the vehicle and its components with the purpose of predicting the resulting response, i.e., the previously mentioned “movements”. The forces that act on the vehicle can be narrowed down to three sources: the tires, gravity and aerodynamics [37]. A more complete theoretical background on vehicle dynamics is presented in Appendix C

The coordinate system used is the SAE vehicle axis system [38] and the terminology adopted is based on the one used in [37]. A detailed description of the axis system is presented in Appendix D.

3.1 Free-body Diagram

The first step for analysing any vehicle’s dynamics behaviour is the sketching of its free-body diagram, along with all the significant forces acting on it, under arbitrary conditions. For the vehicle studied, the free-body diagram with respect to the x-z plane is as seen in Figure 3.1, where the forces shown are mainly those of interest to the longitudinal analyses developed throughout this work.

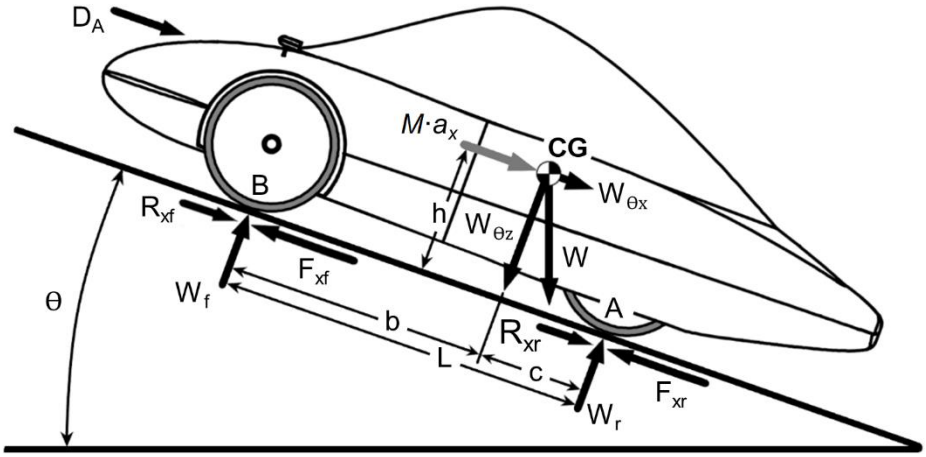

Figure 3.1 - Arbitrary forces acting on a vehicle free-body diagram, x-z plane.

The forces acting on the vehicle are:

W - Weight of the vehicle acting at its CG; it is equal to its mass times the acceleration of gravity. On an incline (θ), W is split in $W_{\theta x}$ and $W_{\theta z}$, along the vehicle’s x and z-axis, respectively.

$W_{r,l}$ - Dynamic weights of the axles experienced by the tires on the contact points A and B. The subscript “r” and “f” denote the rear and front wheel, respectively.

F_x - Tractive force of the tires acting in the longitudinal direction of the vehicle.

R_x - Rolling resistance of the tires along its x-axis. It acts on the tire’s contact patch and always opposes the direction of the vehicle’s movement.

D_a - Aerodynamic drag force acting on the body of the vehicle. It is assumed that the force is applied at the same height "h" of the centre of gravity.

$M \cdot a_x$ - Inertial force known as "d'Alembert force[7]" caused by the acceleration of the vehicle. It acts on the centre of gravity in the opposite direction of the acceleration. It can be convenient for dynamics calculations when the vehicle is accelerating along the road.

3.2 Dynamic Axle Loads

Determining the axle loads is important to analyse the traction limits of the vehicle., i.e., the maximum acceleration and braking. To calculate the load on one axle, a simple application of Newton's Second Law (Appendix C) is required, as is exemplified below for the front axle:

Assuming the front wheels remain in contact with the ground and applying a static equilibrium using d'Alembert's principle, the sum of the moments around point A must be equal to zero.

Since the moments about point A are positive in a clockwise direction (SAE axis system – Appendix D) we obtain:

$$W_f \cdot L + (D_a + W_{\theta x} + M \cdot a_x) \cdot h - W_{\theta z} \cdot c = 0 \tag{3.1}$$

Solving Eq. (3.1) for W_f and applying the same steps for point B, the equations for the axle loads become:

$$W_f = W \cdot \cos\theta \cdot \frac{c}{L} - (D_a + W \cdot \sin\theta + M \cdot a_x)\frac{h}{L} \tag{3.2}$$

$$W_r = W \cdot \cos\theta \cdot \frac{b}{L} + (D_a + W \cdot \sin\theta + M \cdot a_x)\frac{h}{L} \tag{3.3}$$

To determine the maximum traction available at the tires for a rear-wheel-drive vehicle Eq. (3.3) is used to calculate the dynamic weight on the rear axle and then the following expression is applied:

$$F_{x\,max} = \mu_t \cdot \frac{W_r}{0.5 \cdot N_w} \tag{3.4}$$

where μ_t is the friction coefficient between the road surface and the tires and N_w is the number of wheels doing the work, i.e., for a rear-wheel-drive car where only one wheel does work, the maximum traction is half of what it would be for a similar car with two driving wheels. It should be noted that for mechanical braking (negative tractive force) the four wheels of the vehicle are used.

The friction coefficient depends heavily on the tire characteristics, type of road surface and on the road conditions. However, since the vehicle is to be used only in concrete or asphalt roads, the conservative friction coefficient values of 0.8 and 0.5 will be used for dry and wet roads, respectively.

[7] The d'Alembert's principle is an alternative form of Newton's Second Law stated by Jean le Rond d'Alembert that, in effect, reduces a problem in dynamics to one in statics. D'Alembert's form states that the force F acting on a body plus the negative of its mass M times acceleration a is equal to zero: $F - M \cdot a = 0$. Meaning the body is in equilibrium under the action of a real force F and a fictitious (or inertial) one $-M \cdot a$.

3.3 Longitudinal Vehicle Model

In reality, vehicles not only travel on a level road but also up and down slopes and around corners. To model the vehicle's motion, a simpler straight two-dimensional road where there are no corners can be considered [22]. This model is focused on the vehicle's performance when accelerating, cruising and braking while on a road with variable grade. This is done by applying Newton's Second Law along the longitudinal axis of the vehicle (Figure 3.1), resulting in the equilibrium presented in equation (3.5):

$$F_x - \underbrace{(R_x + W_{\theta x} + D_A)}_{\text{Resistive Forces}} = M \cdot \alpha_x \tag{3.5}$$

where:

$$F_x = F_{xr} + F_{xf} \tag{3.6}$$

$$R_x = R_{xr} + R_{xf} \tag{3.7}$$

3.3.1 Tractive Force

The tractive force generated by the electric motor for accelerating or braking is studied to a higher degree than the tractive force developed by the disk brakes. After all, when using friction brakes, all the kinetic energy is dissipated in the form of heat and lost, while using the motor as a brake some of that energy can be recovered. For this reason, when attempting to achieve the highest efficiency the use of the disk brakes should be avoided when possible and used only as a last resort.

For the case where the electric motor provides the tractive force, the two possible scenarios of interest are shown in Figure 3.2. In (a) the motor generates the torque that "pushes" the vehicle and in case (b) it creates a torque opposite to the direction of rotation of the shaft, resulting in a braking force.

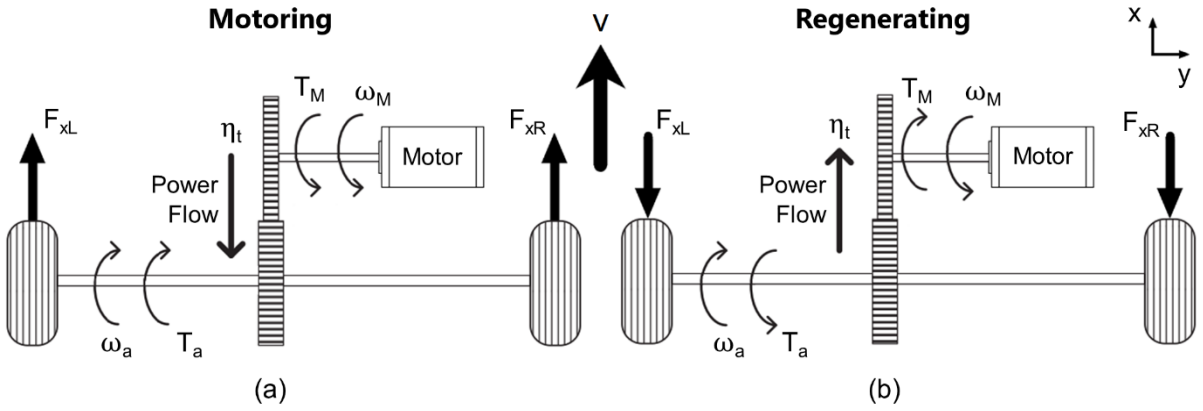

Figure 3.2 - Vehicle motoring (a) and braking/regenerating (b), adapted from [24]

ω_a	- Axle angular velocity ;	F_{xL}	- Tractive force on the left wheel [N];
ω_M	- Motor angular velocity ;	F_{xR}	- Tractive force on the right wheel [N];
T_a	- Torque on the axle;	η_{DCDC}	- Efficiency of the transmission;
T_M	- Torque output of the motor;	v	- Vehicle forward velocity.

Starting with the electric motor and considering the motoring case (a), the torque provided by the motor to the transmission can be determined by application of Newton's Second Law with equation (3.8):

$$T_t = T_M - J_M \cdot \alpha_M \tag{3.8}$$

where:

T_t = Torque at the transmission (motor side) [N·m];

J_M = Rotational inertia of the motor's shaft [kg·m^2];

α_M = Angular acceleration of the motor's shaft [rad/s^2].

The torque delivered to the axle and wheels that ultimately provides the tractive force at the road (sum of the left and right tractive forces) is amplified by the gear ratio of the transmission with some reductions from the inertia of the driveline components and transmission. The equations for this are:

$$T_a = (T_t - J_t \cdot \alpha_M) \cdot N_t \tag{3.9}$$

$$F_x \cdot r = T_a - J_w \cdot \alpha_w \tag{3.10}$$

where:

J_t = Rotational inertia of the transmission (as seen from the motor side);

N_t = Numerical gear ratio of the transmission;

r = Radius of the tires [m];

J_w = Rotational inertia of the wheels and axle shafts;

α_w = Angular acceleration of the wheels (same as the axle).

The relation of the motor and wheels rotational accelerations can be easily determined by the transmission ratio.

$$\alpha_M = N_t \cdot \alpha_w \tag{3.11}$$

Knowing that the vehicle acceleration, a_x, is equal to the wheel rotational acceleration times the tire radius and combining the above equations (3.8) to (3.11) it is now possible to solve for the tractive force available on the ground:

$$F_x = \frac{T_M \cdot N_t}{r} - [(J_M + J_t)N_t^2 + J_w]\frac{a_x}{r^2} \tag{3.12}$$

Finally, the effect of the inefficiencies due to mechanical and viscous losses in the transmission can be approximated by adding an efficiency value in the first term on the right-hand side of equation (3.12) [37]. It should be noted that until this point the equations above were valid for both the motoring and braking cases, (a) and (b), but with the inclusion of the efficiency value in the expressions for the tractive force when motoring and braking become.

Motoring tractive force – case (a):

$$F_x = \frac{T_M \cdot N_t \cdot \eta_t}{r} - [(J_M + J_t)N_t^2 + J_w]\frac{a_x}{r^2} \tag{3.13}$$

Braking tractive force[8] – case (b):

$$F_x = \frac{T_M \cdot N_t}{r \cdot \eta_t} - [(J_M + J_t)N_t^2 + J_w]\frac{a_x}{r^2} \tag{3.14}$$

Therefore, the tractive force that can be obtained from the electric motor for both cases is described by equations (3.13) and (3.14). These equations can be divided in two components:

1. The first term on the right-hand side represents de steady-state[9] tractive force available to overcome the resistive forces and accelerate the vehicle or to oppose its movement and brake.
2. The second term on the right-hand side represents the "loss" of tractive force due to the inertia of the rotor, transmission and drivetrain components. It should be noted that if the car is maintaining a constant velocity this component is equal to zero.

3.3.2 Rolling Resistance

One of the major sources of resistance to movement of the vehicle is the rolling resistance of its tires. In fact, at low velocities it is the primary motion resistance force, which means that it should be one of the main causes of energy loss in the team's vehicle and one of the primary focus of investment and optimization for achieving the highest energy efficiency.

There are many mechanisms responsible for the rolling resistance, e.g., energy loss due to deflection of the tire sidewall and thread elements, tire slip, air drag, road imperfections, to name a few. Modelling all these phenomena would be impractical so the empirical equation (3.15) is commonly applied:

$$R_x = f_r \cdot W \cdot \cos\theta \tag{3.15}$$

where:

f_r = Rolling resistance coefficient;

For some situations, i.e., when accelerating and braking, the dynamic weight of the vehicle on the front and rear axis may be used to calculate the rolling resistance. However, for the purpose of estimating the vehicle's performance, this would complicate the calculation without offering any significant improvements in accuracy [37].

[8] When braking, the lower the transmission´s efficiency the highest the braking force but, on the other hand, the least torque will reach the motor for recovering energy in regenerative braking.

[9] A mechanical model is referred to a "steady state" when all the variables are constant in time.

3.3.3 Grading Force

The grading force is simply the result of the pull exerted by earth's gravity on the vehicle while on an inclined road. Since gravity pulls the vehicle straight down, the horizontal plane from which the grading angle, θ, is measured is its perpendicular. This force opposes forward motion when the vehicle is climbing (θ is positive) and aids it when it is descending (θ is negative).

$$W_{\theta x} = W \cdot \sin\theta = mg \cdot \sin\theta \tag{3.16}$$

3.3.4 Aerodynamic Drag

The aerodynamic forces on a body are caused by the interaction of its surface with the surrounding flow in two distinct ways; one is usually referred to as form or pressure drag and the other as skin or viscous friction drag. In a vehicle, form drag is usually responsible for most of the aerodynamic force and is caused by the pressure difference that occurs due to flow separation at the back of the vehicle; viscous friction drag is generally much smaller and results from the sheer stress in the boundary layer on the surface of the vehicle's body.

To determine the force caused by aerodynamic drag it is necessary to use a semi-empirical model because, even in the simplest of cases, the flow around a body is extremely complex. Therefore, equation (3.17) is commonly used to characterize the aerodynamic drag:

$$D_A = \frac{1}{2}\rho \cdot {v_f}^2 \cdot C_D \cdot A_F \tag{3.17}$$

where:

C_D = Aerodynamic drag coefficient; v_f = Relative velocity of the air flow;

A_F = Frontal area of the vehicle; ρ = Air density.

The drag coefficient, C_D, is determined empirically for the vehicle, the frontal area, A_F, is the area of the vehicle as seen from the front to account for the size of the car and the rest of equation (3.17) accounts for the dynamic pressure of the air.

If conditions change considerably from the standard sea-level pressure and temperature, the density should be corrected for the new conditions, as described in Appendix E.

3.4 Tire Drag when Cornering

The previous section introduced the main forces that affect the vehicle's movement, considering a simple model where motion is always in a straight line. This simplification is good for approximating the phenomena described Section 3.3, however it does not account for the drag caused by the tires when cornering, which can be several times higher than the "straight-line" rolling resistance given by Eq. (3.15), for cruising-speed cornering.

3.4.1 Low-speed Turning

First, it is interesting to do a brief mention of the vehicle's behaviour for low-speed cornering, where no lateral forces act on the vehicle. The geometry that results from cornering with pure rolling of the wheels, as seen in Figure 3.3, is called Ackermann Steering and results in no extra tire drag. For this situation, equation (3.15) given in Section 3.3.2 is sufficient for modelling the vehicle and cornering can be ignored.

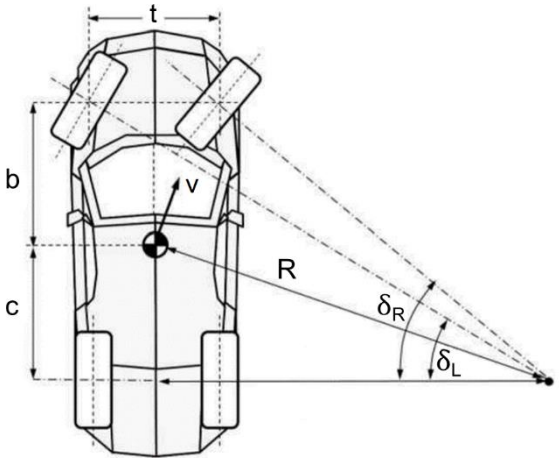

Figure 3.3 - Low-speed turning, adapted from [39].

δ_L, δ_R - Left and right steering angles; b, c - Axles distances from the CG;

R - Turn radius; t - Track width.

For the proper geometry and assuming small angles, the average of the front steer angles is defined as the Ackermann angle:

$$\delta = {}^{L}/_{R} \tag{3.18}$$

3.4.2 Cruising-speed Cornering

At higher speeds, lateral acceleration will be present and, to counteract this, the tires must develop lateral forces. Consequently, the slip-angle α appears at each tire making the lateral force (also called cornering force) F_y contribute to the overall tire drag, as seen in Figure 3.4.

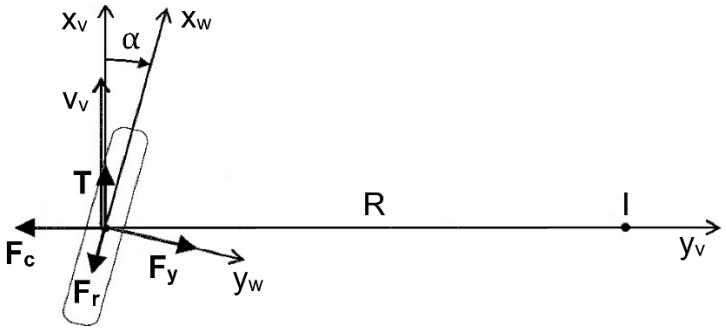

Figure 3.4 - Tire under cruising-speed cornering, adapted from [40]

x_v, y_v - Vehicle coordinate system; F_r - Wheel rolling resistance force;

x_w, y_w - Wheel coordinate system; T - Tractive cornering force;

F_y - Tire lateral force; α - Wheel slip angle;

F_c - Centrifugal force; I - Centre of rotation.

The tractive cornering force T is equal and in the opposite direction of the total tire drag, keeping the vehicle's velocity constant.

To calculate the impact cornering has on the tire drag, it is essential to first determine the relation between the slip angle and the magnitude of the lateral force produced by the tire. At a given tire load, F_z, the cornering force grows with slip angle. For small slip angles, the relation is linear and can be described by:

$$F_y = C_\alpha \cdot \alpha \tag{3.19}$$

The constant, C_α, known as the "cornering stiffness", is the slope of the curve for F_y versus α at α=0 (Figure 3.5). The cornering stiffness is dependent on many variables, e.g., tire size, tire type (radial or bias-ply), wheel width, tread, to name a few. For a given tire, the load and the inflation pressure are the main variables and speed does not strongly influence the forces produced by the tire [37].

Equation (3.19) is straightforward and very useful for modelling vehicles under normal conditions, however, for larger slip angles the relation ceases to be linear and it becomes inaccurate. Hence, it is often necessary to resort to experimental or empirical methods to estimate the curve F_y versus α.

3.4.3 Magic Formula

One of the most well-known and widely used empirical models is Pacejka's "Magic Formula" model, where a set of equations using parameters specific to the tire approximate its behaviour.

The basic equation for the lateral force versus slip angle curve given by Pacejka is [41]:

$$F_y = \mathrm{D} \cdot \sin\left[\mathrm{C} \cdot \tan^{-1}\left(\mathrm{B} \cdot \alpha - \mathrm{E}(\mathrm{B} \cdot \alpha - \tan^{-1}(\mathrm{B} \cdot \alpha))\right)\right] \tag{3.20}$$

where:

$$C_\alpha = \mathrm{p_{Ky1}} \cdot F_{zn} \sin\left[\mathrm{p_{Ky4}} \tan^{-1}\left(\frac{F_Z}{\mathrm{p_{Ky2}} \cdot F_{zn}}\right)\right] \tag{3.21}$$

The factors B, D, E and the cornering stiffness, C_α, are calculated with parameters given by the manufacturer for the Magic Formula (like C, $\mathrm{p_{Ky1}}$, $\mathrm{p_{Ky2}}$, $\mathrm{p_{Ky4}}$ and F_{zn}) or can be estimated experimentally through regression techniques. The equations and parameters are listed in Appendix F.

The curves and cornering stiffness coefficients for three load situations for Michelin's Urban Concept tires, designed for Shell Eco-marathon, are given in Figure 3.5. The plots were calculated with Pacejka's model with parameters provided by Michelin for the tire, for an inflation pressure of 4 bar. The straight grey line is given for comparison as it follows the linear model of Eq. (3.19), for the 600 N load.

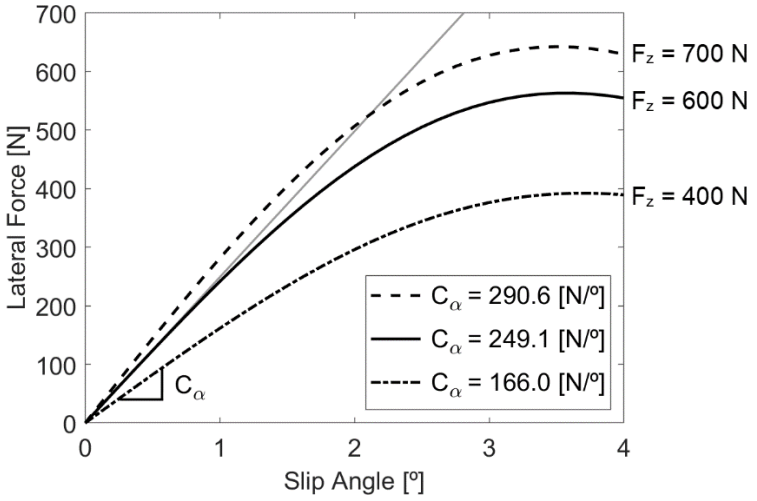

Figure 3.5 - Tire cornering force properties for Michelin Urban Concept 95/80 R16.

3.4.4 Bi-cycle Vehicle Model

To estimate the tire drag generated by cornering, three models were considered: the uni-cycle (Figure 3.4), the bi-cycle and the 4-wheel model. Of these, the bi-cycle model, seen in Figure 3.6, was chosen because it gives results almost as good as the 4-wheel model and is less complex. The uni-cycle model, even if it is the simplest, was disregarded because it produces results around 20% higher than the other two models [40].

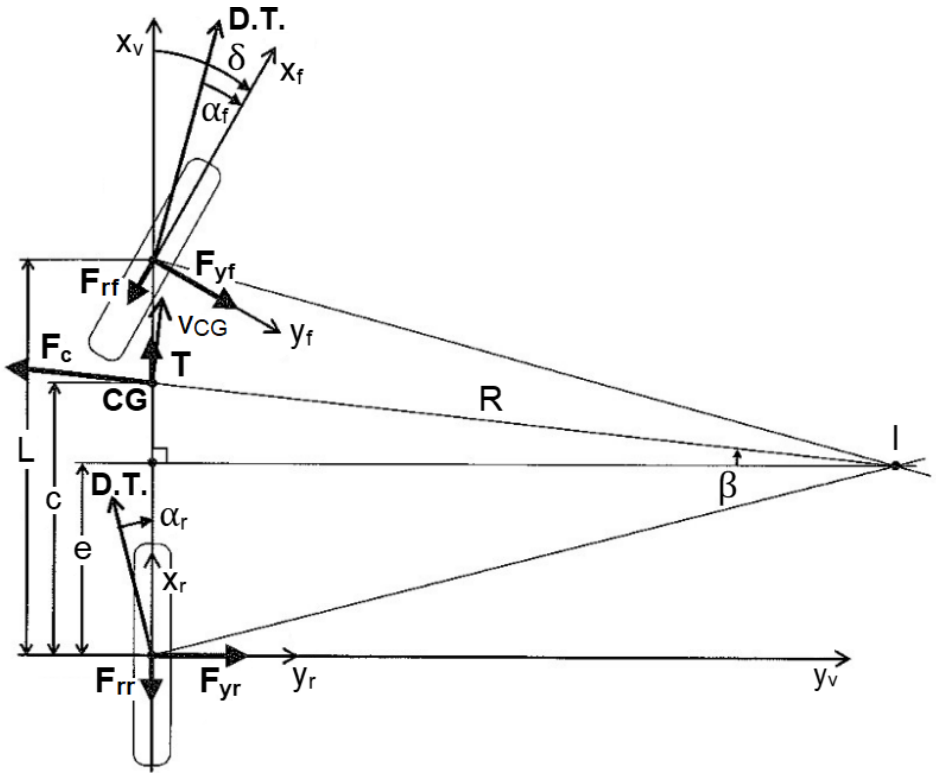

Figure 3.6 - Free-body diagram of the bi-cycle vehicle model, adapted from [40].

D.T. - Direction of travel of the wheel;
e - Projection of the centre of rotation;
x_f, y_f - Front wheel coordinate system;
x_r, y_r - Rear wheel coordinate system;

The bi-cycle model is a good approximation for the vehicle's turning mechanics because the turn radius is always much larger than the track width and small angles can be considered, thus, the left and right steer angles can be substituted by their average, the Ackermann angle Eq. (3.18), and the front and rear wheels can be represented by one wheel per axle, in the vehicle's longitudinal plane of symmetry.

Note: In the one wheel per axle simplification, the lateral tire forces on each axle have to be multiplied by two to account for the tractive effort of both wheels.

The knowns of the problem are:

1. The vehicle characteristics: mass M, wheelbase L and the position of the centre of gravity CG on the vehicle's x-axis, c;
2. The tire characteristics: cornering stiffness C_α and the rolling resistance coefficient;
3. Cornering conditions: turn radius R and the vehicle velocity v_{CG}.

The unknowns are:

1. The steer angle δ;
2. The angle β that positions the turn centre I on the vehicle's x-axis;
3. The front and rear slip angles, α_f and α_r, respectively;
4. The tire forces: normal loads F_{zf} and F_{zr}, lateral forces F_{yf} and F_{yr} and the rolling resistance forces F_{rf} and F_{rr};
5. The tractive cornering force T, necessary to maintain the vehicle at constant velocity.

Simplifications:

1. Infinitely rigid chassis that connects the front and rear wheels;
2. Road with no inclination (θ = 0);
3. No aerodynamic force (D_a = 0);
4. Vehicle velocity is constant.

The problem can be solved using the following steps and equations, adapted from [40]:

(1) Calculate the centrifugal force:

$$F_c = \frac{M \cdot {v_{CG}}^2}{R} \tag{3.22}$$

(2) Calculate the normal loads for the front and rear tires with Equations (3.2) and (3.3), taking into account the mentioned simplifications;
(3) Calculate the cornering stiffness of each wheel using Eq. (3.21);
(4) Calculate the rolling resistance forces of the wheels with Equation (3.15) (using the normal loads for the front and rear tires instead of $W_{\theta z}$);

At this point, there are still seven unknowns: α_f, α_r, F_{rf}, F_{rr}, F_{yf}, F_{yr} and T. Hence, it is necessary to solve the equations from step (5) to (7) simultaneously.

(5) For the geometric relationships:

$$\tan(\delta - \alpha_f) = \frac{L - e}{R \cdot \cos\beta} \tag{3.23}$$

$$\tan(\alpha_r) = \frac{e}{R \cdot \cos\beta} \tag{3.24}$$

$$\sin\beta = \frac{c - e}{R} \tag{3.25}$$

(6) For the lateral behaviour of the tires apply equation (3.20) to the front and rear wheels and multiply it by two, to account for the tractive effort of both wheels;

(7) For the vehicle equilibrium equations in the road plane:

$$T - F_{rr} - F_{rf} \cdot \cos\delta + F_c \cdot \sin\beta - F_{yf} \cdot \sin\delta = 0 \tag{3.26}$$

$$F_{yr} - F_{rf} \cdot \sin\delta - F_c \cdot \cos\beta + F_{yf} \cdot \cos\delta = 0 \tag{3.27}$$

$$-c \cdot F_{yr} + (L - c)\left(F_{yf} \cdot \cos\delta - F_{rf} \cdot \sin\delta\right) = 0 \tag{3.28}$$

Solving the system of equations using Matlab, we get the tractive cornering force T, which is equivalent to a resistive force that incorporates both the effects of tire drag due to cornering and rolling resistance. In fact, for an infinitely large turn radius (straight road), δ and β are zero and Eq. (3.26) becomes:

$$T = F_{rr} + F_{rf} \tag{3.29}$$

Remembering that F_{rr} and F_{rf} are the rolling resistances of the front and rear tires, we can see that in this situation T is equal to R_x from equation (3.7).

In Figure 3.7, the tire drag results of the bi-cycle model, for various vehicle velocities and turn radii, are presented for a 170 kg vehicle (with driver) equipped with the already mentioned Michelin Urban Concept tires. The aerodynamic drag curve for a vehicle with a frontal area of 0.9 m^2 and an aerodynamic drag coefficient of 0.18 is also shown for comparison.

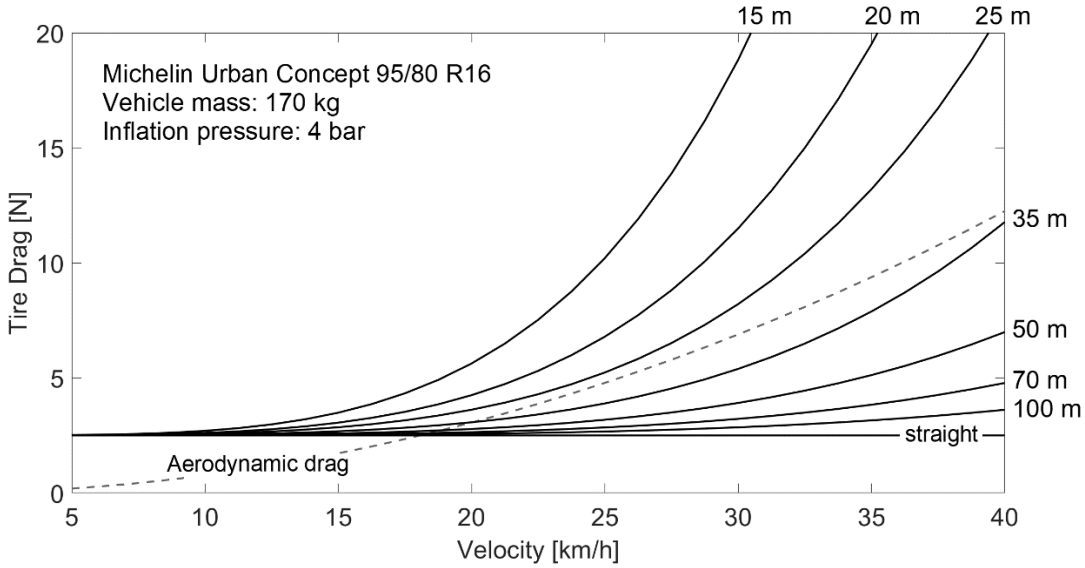

Figure 3.7 - Tire drag given by the bi-cycle model for different speeds and turn radii.

The results of the bi-cycle model clearly show that the tire drag is much higher when cornering than when moving in a straight line. In fact, for a velocity of 35 km/h a turn radius of only 50 m doubles the drag force produced by the tires, when comparing to a straight road. This confirms that an accurate dynamic model of the vehicle is essential for the development of an effective driving strategy to reduce the hydrogen consumption as much as possible.

3.5 Electric Motor Energy Consumption

To estimate the energy consumption of the vehicle, an appropriate model of the electric motor must be used. The model is fundamental to establish the relationship between the rotational mechanical energy of the drive system and the electrical energy of the powertrain. However, since different machines require different models to simulate how they work, it is necessary to first determine the motor technology to be used. Hence, the first sub-section is dedicated to the method used to select the best motor technology for the vehicle, while the ones after that are for describing the chosen model.

3.5.1 Motor Technology Selection

To select the best motor technology for the vehicle, the main pros and cons of relevance, i.e., efficiency, power density, control complexity, cost and maintenance, were evaluated for several motor technologies suitable for this type of applications. Then, a Multi-Criteria Decision Making (MCDM) table (Table 3.1) was built to assist with the selection of the best motor technology. The weights of the used criteria were selected in accordance to their importance for the mission of the vehicle, as well as the feasibility of the project. The selected criteria values for each motor type were selected by the author based on the comparison of datasheets from real motors and on the references [17], [18], [42]–[45].

Table 3.1 - Multi-Criteria Decision Making table to choose the motor technology for the vehicle.

Criteria		**Type of Motor**				
	wt.[1]	**DC**	**IM**	**RM**	**BLDC**	**PMSM**
Efficiency	5	1	2	3	4	5
Power Density	4	2	3	3	4	5
Control Complexity	3	5	2	4	4	2
Cost	2	4	5	4	3	1
Maintenance	1	1	5	5	5	5
	Score:	37	43	52	**59**	58

[1] Weight of each criterion (from 1 – Not Important to 5 – Very Important).

* Criteria are evaluated from 1 – Poor to 5 – Excellent.

* DC – Brushed DC motor; IM – Induction Motor; RM – Reluctance Motor.

According to the MCDM Table 3.1, the best type of motor for the vehicle is a permanent magnet BLDC motor. This choice was corroborated by the “selection of the optimum motor technology” table from [46], where permanent magnet motors, namely the BLDC, were also the clear winners (filled table in Appendix G). However, it should be noted that in both tables the PMSM also had a very high rating and, if cost is disregarded, it even surpasses the BLDC as the best choice for the vehicle.

Based on the scores of Table 3.1, as well as what was discussed in Section 2.1.2, the type of motor selected for the vehicle is of the brushless DC technology. Ergo, the corresponding model of a BLDC motor is discussed in the following sections.

3.5.2 BLDC Motor Market Study

To select which brushless DC electric motors to evaluate, an extensive search of many brands and models was done, narrowing the final selection to three Dunkermotoren BLDC motors of different power outputs. This brand was selected due to its offer of high quality and efficient BLDC motors, at a reasonable price. Another reason for selecting this brand is the fact that they sell directly to consumers, which is often a limitation for other brands, who only sell if a minimum number of motors are ordered, e.g., Sonceboz CPM90 BLDC motor could be an excellent choice for the vehicle, however, the brand only offers its motor to applications with an annual potential of more than one thousand units.

The three BLDC motors selected to be compared in terms fuel efficiency, using the methods later developed in this master thesis, are the 24 V versions of Dunkermotoren’s BG 95X80, BG 95X40 and BG 75X50, with powers outputs of 1000, 701 and 431 Watts, respectively. The motors are shown in Figure 3.8 and the main specifications for each motor are shown in Appendix H.

Figure 3.8 - Dunkermotoren BLDC motors: BG 95X80 (a), BG 95X40 (b) and BG 75X50 (c), images from [47].

The electrically commutated motors use Hall sensors for rotor position detection, have three-phases and use an 8-pole neodymium magnet on the rotor. One other plus of using a Dunkermotoren motor is the large offer of attachments like controllers, gearboxes and motor brakes of high quality and efficiency.

3.5.3 Introduction to Brushless DC Motor Models

The majority of models presented throughout the literature simulate the full motor-commutator circuit, shown in Figure 3.9, and describe the full operation of the motor with precision (examples of these

models in [48]–[50]). However, these types of models are not suitable for the vehicle model developed in this work, as they are characterized by a relatively long computational time and would make the simulations and optimizations extremely slow.

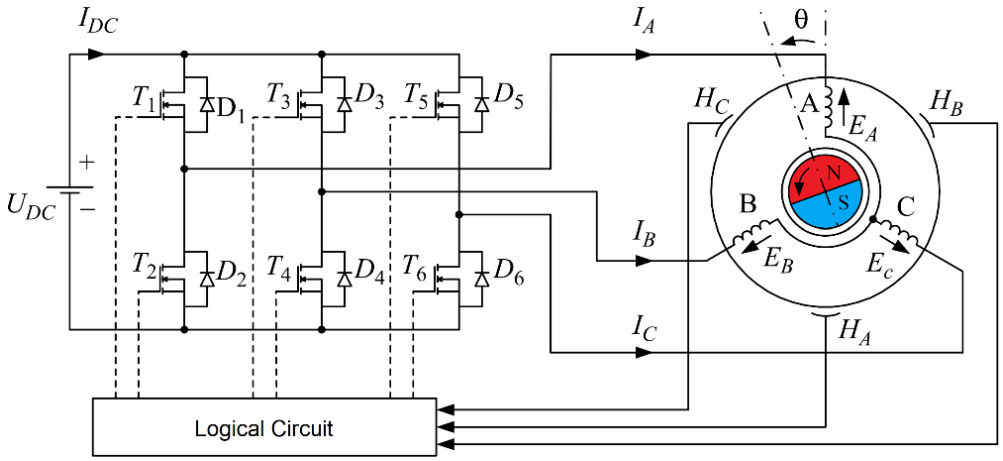

Figure 3.9 – Schematic of a three-phase, one pole pair BLDC motor, including the electronic commutator and hall sensors, adapted from [51].

U_{DC}	- DC supply voltage;	E_k	- Back EMF of phase k;
I_{DC}	- DC supply current;	θ	- Rotor position.
A, B, C	- Three phases of the BLDC motor;	T_{1-6}	- Transistors;
I_k	- Current of phase k;	D_{1-6}	- Diodes;

To by-pass the computing time problem, a simplified functional model that only shows the relationships between current, voltage, load torque and rotational speeds for transient states can be used instead. These types of models are useful for simulations that do not take the effects occurring inside the motor-commutator system into consideration.

Since BLDC motors are similar to brushed DC motors with electronic commutation instead of brushes, the constant current equivalent circuit model for the DC motor is sometimes used for the BLDC motor. However, this overly simplistic approximation, which does not take commutation into consideration, is not recommended because the resulting torque-speed characteristics can significantly differ from the real BLDC motor [52]. To correct this, K. Krykowski proposes a modified constant current model (MCCM) based on the same DC motor model, that takes into account the impact of inductance on the torque-speed characteristics of the BLDC motor [52].

3.5.4 BLDC Motor Modified Constant Current Model

The model for the BLDC motor developed in this section is based on the before mentioned modified constant current model proposed by K. Krykowski.

A BLDC motor with the structure shown in Figure 3.9 can be simplified as a constant current equivalent model with the structure shown in Figure 3.10. This model assumes that the common 120-degree commutation (shown in Appendix I) is used, and that two of the phases are always connected. Therefore, the circuit resistance, inductance and back EMF appear as duplicated.

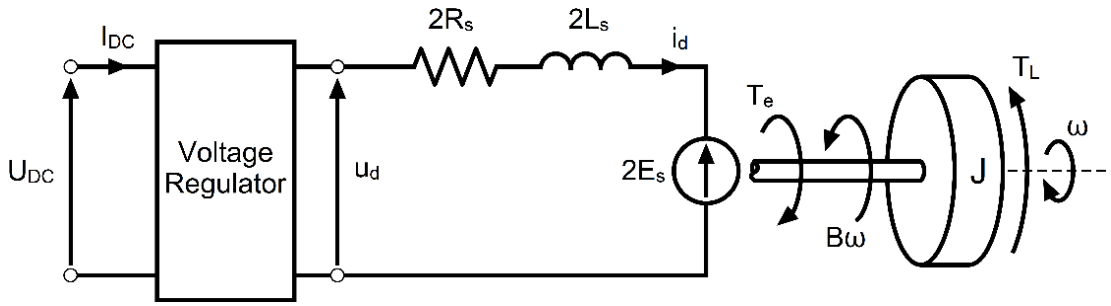

Figure 3.10 - BLDC motor as a special case of DC motor.

u_d	- Motor input voltage;	T_e	- Electromagnetic torque;
i_d	- Motor input current;	T_L	- Load torque;
E_s	- Phase back EMF;	J	- Total moment of inertia;
R_s	- Phase resistance;	B	- Motor damping coefficient;
L_s	- Phase inductance;	ω	- Rotor angular velocity.

The relationship between instantaneous current and voltage for this motor can be written as:

$$u_d = 2 \cdot R_s \cdot i_d + 2 \cdot L_s \frac{di_d}{dt} + 2 \cdot E_s \tag{3.30}$$

$$E_s = E_{fp} = K_{fp} \cdot \omega \tag{3.31}$$

where E_{fp} is the back EMF voltage and K_{fp} the phase excitation coefficient for the flat portion of the phase EMF waveform (Appendix I).

Additionally, the mechanical system of Figure 3.10, representing the motor, the drivetrain and all the forces acting on the vehicle, can be described by the following relation:

$$T_e = T_L + B \cdot \omega + J \frac{d\omega}{dt} \tag{3.32}$$

Simplifying equation (3.30), for the case of an ideal motor with negligible inductance impact where the motor current and voltage can be considered as average values, it becomes:

$$U_d = 2 \cdot R_s \cdot I_d + 2 \cdot K_{fp} \cdot \omega \tag{3.33}$$

and the following relation is true:

$$T_e = 2 \cdot K_{fp} \cdot I_d \tag{3.34}$$

In a real motor, however, when commutation occurs, the phase currents do not change instantly in the step-like manner shown in Appendix I, but rather rise and decrease following an exponential curve, causing additional voltage drops. In addition to this, during commutation the energy stored in the phase winding that disconnects is recuperated and current (known as freewheel current) flows back to the motor through the body diode, until its voltage becomes equal to the back EMF voltage [53] (example

of this shown in Appendix J. Hence, the current generating electromagnetic torque I_e is greater than the average input current I_d calculated for the DC circuit, and Eq. (3.34) is rewritten as:

$$I_e = \frac{T_e}{2 \cdot K_{fp}} > I_d \tag{3.35}$$

The commutation voltage drops can be taken into account by adding a commutation impact coefficient, which estimates the ratio between commutation and resistance voltage drops:

$$k_Q = \frac{U_{comm}}{U_R} \tag{3.36}$$

Assuming that the motor speed remains approximately constant during commutation, Eq. (3.36) can be defined as follows [52]:

$$k_Q = \frac{m \cdot p}{2 \cdot \pi} \cdot \frac{\omega \cdot L_s}{2 \cdot R_s} \tag{3.37}$$

where m is the step commutation number and p the number of pole pairs.

Using the commutation impact coefficient (3.37) in Eq. (3.33), it becomes:

$$U_d = 2 \cdot R_s \cdot \left(1 + k_Q\right) \cdot I_e + 2 \cdot K_{fp} \cdot \omega \tag{3.38}$$

The relation between current in the motor I_e and the average current I_d can be approximated by:

$$I_d = k_\omega \cdot I_e \tag{3.39}$$

where k_ω is the coefficient of decrease in rotational speed compared to the ideal motor:

$$k_\omega = \frac{1}{1 + \frac{m \cdot p \cdot L_s}{4 \cdot \pi \cdot K_{fp}} \cdot I_e} \tag{3.40}$$

The excitation coefficient for the flat portion of the phase back EMF waveform can be estimated as:

$$K_{fp} = \frac{1}{2} \frac{U_{dn}}{\omega_{nl}} \tag{3.41}$$

where U_{dn} is the nominal voltage and ω_{nl} is the no-load speed of the motor.

The remaining values needed for the model, except the motor's viscous damping coefficient B, can be retrieved from the motor's datasheet or can be obtained from the vehicle's model or components.

The motor damping coefficient can be estimated using equation (3.42) that ensures that, in no-load conditions, a current equal to the no-load current I_{nl} is consumed when the motor is rotating at the no-load speed ω_{nl} [54]:

$$B = \frac{K_t \cdot I_{nl}}{\omega_{nl}} \tag{3.42}$$

where K_t is the motor torque constant given by the manufacturer.

3.5.5 BLDC MCCM Discussion

Using the modified constant current model with a known motor angular velocity ω and input current I_d, if perfect current control is assumed, it is possible to estimate everything needed for the dynamic model of the vehicle. The main values to be obtained from the model are the load torque, which is used in Section 3.3.1 to determine the tractive force, and the input voltage that, multiplied with the input current, gives the motor power consumption. Having the motor torque, angular velocity and input power, it is trivial to calculate the energy consumed by the motor and its efficiency. To showcase the model's results, the Dunkermotoren BLDC motor BG 95x80 dCore efficiency map, simulated by the modified constant current model, is shown below in Figure 3.11.

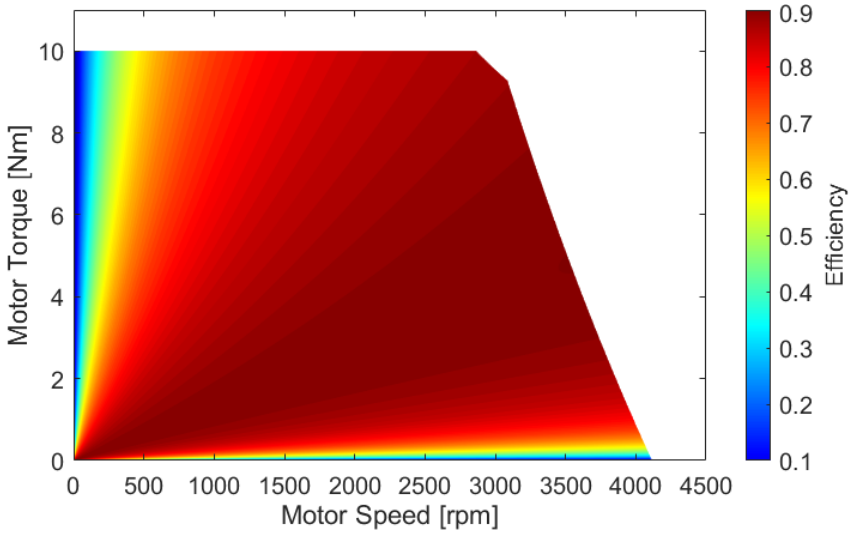

Figure 3.11 - Efficiency map of a Dunkermotoren BG 95x80 dCore, generated with the BLDC MCCM.

The technical data used was obtained from the motor's data sheet, given on Dunkermotoren's website [55]. The values used are: U_{dn} = 24 V, N_n = 3890 rpm, N_{nl} = 4150 rpm, I_{nl} = 4.2 A, R_s = 6.5 mΩ, L_s = 0.0185 mH, K_t = 0.06 Nm/A, p = 4, m = 6 and T_{Lmax} = 10 Nm. It should be noted that R_s and L_s are the phase resistance and inductance, which are half of the terminal resistance and inductance values given in the datasheet.

The values simulated by the model for the nominal and no-load rotational speeds are equal to: N_n = 3806 rpm and N_{nl} = 4116 rpm. These values differ from those given in the motor's data sheet by approximately 2% and 1%, respectively. These results, and the ones presented in [52] for nominal and below nominal voltages, show that the model is accurate and gives a good approximation of the real motor operation for various conditions.

It can be observed in Figure 3.11 that the efficiencies predicted by the model for very low torques and speeds are not accurate. This can result from it not including other types of energy loss like eddy current and hysteresis losses, which could contribute to decrease the efficiency for these working conditions. However, in the vehicle's case, the motor should operate at close to nominal torques and speeds most of the time, where the model is most accurate. Even so, the author recommends that a comprehensive study of the acquired electric motor is done in a testbench to obtain the characteristic curves and parameters of the motor, so the model can be validated and fine-tuned if needed.

4 Vehicle Model

The vehicle model was developed using MATLAB (abbreviation of “matrix laboratory”), a powerful tool for data analysis, algorithm development and model creation. For this model, it was opted for the use of MATLAB’s scripts and functions, instead of the more user-friendly Simulink. This decision was made to keep the model simple and its computing time fast, to later make use of heuristic optimization algorithms to find an optimal solution for the driving strategy. It was assumed that using these algorithms with Simulink would be too time consuming.

4.1 Model Features

The main objective of the developed model is to accurately simulate the dynamic behaviour and energy consumption of the vehicle running on a real track, from the fuel cell to the tires. The simulation is split in two models: the main one simulates everything from the motor to the wheel and is responsible for calculating the velocity profile of the vehicle, as well as estimating the energy consumed by the electric motor; the second model runs together with the main model, receiving data from it to simulate the rest of the powertrain, from the fuel cell to the motor, and estimate the hydrogen consumption.

The second objective is the use of the developed model to develop an optimal driving strategy around the track, for the lowest energy consumption. This is crucial to achieve fuel efficiency results that can compete with Shell Eco-marathon’s the top teams.

The third and final goal of the model is to use its simulating capabilities to analyse the impact that modifications to the vehicle’s characteristics, e.g., vehicle mass, aerodynamic coefficient and tire rolling resistance, have on the energy consumption. A valuable tool for the selection of components and to evaluate where efforts should be invested to achieve higher energy efficiencies.

To develop an accurate model that describes the behaviour of the vehicle realistically, it is necessary to know or estimate the characteristics of the vehicle, e.g., vehicle mass, tire performance, aerodynamics, wheelbase, etc, and also detailed information of the track is required, i.e., slope and radius of turn of the corners along the circuit.

4.2 Assumptions

Other than the assumptions already mentioned throughout Chapter 3, several other simplifications were made to avoid needlessly overcomplicating the model, delivering easier to interpret results and faster simulation running times.

The assumptions used are divided in two parts; one for the vehicle system and control and the other for the racetrack and other external factors:

1. Vehicle:

a. The driver perfectly executes the pre-determined driving plan;
b. The powertrain always provides the necessary current-voltage conditions for the electric motor to work as intended;
c. The rolling resistance coefficient is assumed to be constant during the whole drive;
d. Iterations are calculated in steps of 1 metre and all the variables and conditions are assumed to be constant in each iteration;
e. The motor "pushes" the vehicle exactly in the distance of the pre-defined sections;
f. The motor current control is perfect and is constant along each section;
g. The behaviour of the electric motor is described by the modified constant current model of Section 3.5.4;
h. When the motor is not being used, the drive wheels are completely disconnected from the drivetrain to avoid the friction losses of the transmission and the electric motor;
i. The bi-cycle model of Section 3.4.4 is adopted to calculate the vehicle's cornering drag.

2. Track:

a. Only one lap around the track is simulated. This assumption is a good approximation due to the race's repetitiveness (the vehicle must stop near the finish-line every lap);
b. The track is treated as single line. Hence, all its characteristics can be referenced to the lap distance from the start-line;
c. Apart from corners, where the path or "racing line" takes advantage of the track width to lengthen the radius of turn, the vehicle follows approximately the centreline of the racecourse;
d. The length of the racing line is equal to that of the track;
e. The characteristics of the track are calculated in steps of one metre;
f. The atmospheric conditions are constant at standard sea-level pressure (1 atm) and 15 ºC;
g. The road surface is dry;
h. Negligible wind, i.e., the aerodynamic drag felt by the vehicle is caused by its movement alone;
i. Smooth road surface and in good condition;
j. The driving line is approximated by linearly interpolating the data points along its route;
k. The turn radius is calculated for the available points and is linearly interpolated for every metre.

4.3 Track Model

To create the track model to be used in the vehicle model, the method described in Appendix K was developed for the SEM 2016 London track. The final 3D track model with all the generated data to be used in the vehicle model is shown in Figure 4.1.

Note: The model consists of two vectors that contain all the relevant data along the track at every metre, one for the track slope and the other for the cornering radius.

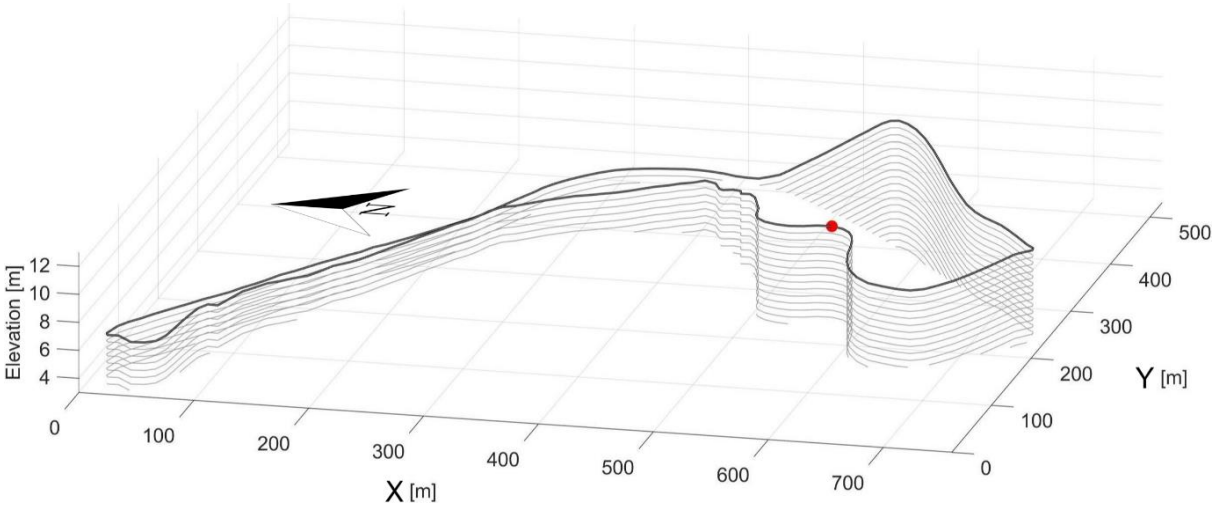

Figure 4.1 - SEM London 2016 3D track model.

4.4 Motor to Wheel Model

Instead of the more usual time-based simulation that similar models use, where the time duration of the iterations is fixed, the model described in this section runs as a function of distance. This is because the track characteristics are known discreetly along the track and, since the lap distance is fixed, it is established as a hard constraint. Time on the other hand is only restricted by the maximum allowed time per lap, e.g., 43 minutes divided by 8 laps for the 2016 London track and is defined as a soft constraint. Hence, as mentioned in assumption 1.d, the analyses of the vehicle dynamics along the track are executed in steps of 1 metre, which gives a good balance of accuracy and computational performance.

Once the vehicle and track specifications of the model are established, the only unknown required to solve the simulation is the motor input current values along the track (duty cycle), which is the design variable used to determine the strategy employed to complete one lap of the circuit. This means that the vehicle velocity profile is calculated from a pre-determined duty cycle strategy for the whole lap that is tailored to the vehicle specifications, track circuit and ambient conditions. Consequently, if any of the data used in the model is changed, e.g., vehicle weight or shape, tires used, dry/wet track, etc, the duty cycle strategy needs to be re-evaluated to adapt to the new simulation conditions.

The method used to optimize the driving strategy and the reason for the selection of the motor input current as the design variable is discussed later in Chapter 5 – Driving Strategy and Powertrain Design.

4.4.1 Vehicle Dynamics Model

Knowing the motor input current at every point of the track, the main variable that is carried over between iterations is the vehicle velocity, i.e., the final velocity of one iteration is the initial of the next. The final lap time and energy consumption are calculated summing the time and energy consumption of all segments of the track.

After defining the duty cycle strategy, i.e., the input current along the track, the first iteration starts with time, distance and velocity equal to zero and, for a generic iteration i with $I_d \neq 0$, the sequence of calculations is as follows:

1. Determine the torque output of the motor T_M (electromagnetic torque T_e minus the motor viscous friction $B\omega$) using the BLDC motor model of Section 3.5.4;
2. Calculate the grading force and aerodynamic drag with equations (3.16) and (3.17), respectively;
3. Determine the tire drag with the bi-cycle model of Section 3.4.4;
   Note: For faster computational times, the tire drag was mapped as a function of turn radius and vehicle velocity. This is further discussed in Section 4.4.2.
4. Find the acceleration by substituting the tractive force equation (Eq. (3.13) for motoring and Eq. (3.14) for braking) into equation (3.5) and solving it for the acceleration. The resulting equation for motoring is shown in equation (4.1):

$$a_x = \frac{T_M \cdot N_t \cdot \eta_t \cdot \frac{1}{r} - (R_x + W_{\theta x} + D_A)}{M + [(J_M + J_t)N_t^2 + J_w] \cdot \frac{1}{r^2}} \tag{4.1}$$

5. Determine the final velocity of the iteration by applying the third equation of motion, Eq. (4.2):

$$v_{i+1} = \sqrt{{v_i}^2 + 2 \cdot a_x \cdot \Delta x} \tag{4.2}$$

At this point it is possible to generate the entire velocity profile of the vehicle along the track. The next steps are required to calculate other useful information about the lap, i.e., energy consumed, lap time, motor power and voltage.

6. Determine the BLDC motor input voltage using Eq. (3.38) of the BLDC constant current model for iteration i and for i+1 using velocities v_i and v_{i+1}, respectively;
7. Calculate the motor electric power for i and i+1 by multiplying the motor's input current with the input voltages, $U_{d\,i}$ and $U_{d\,i+1}$, respectively;
8. The time interval of each iteration is calculated by solving the first equation of motion, Eq. (4.3):

$$\Delta t_i = \frac{v_{i+1} - v_i}{a_x} \tag{4.3}$$

9. The energy consumed by the motor for a one metre segment, $E_{M,i}$, is equal to the integral of the motor's electric power versus time curve, which can be calculated with the area below the curve. For any segment i to i+1, the power versus time graph has a trapezoidal shape and its area can be calculated with:

$$E_{M,i} = \frac{1}{2}\left(P_{M,i} + P_{M,i+1}\right) \cdot \Delta t_i \tag{4.4}$$

10. Finally, the energy consumed by the motor and the lap time are determined by summing the values calculated for all iterations.

$$E_M = \sum_{i=1}^{x_{lap}} E_{M,i} \tag{4.5}$$

$$t_{lap} = \sum_{i=1}^{x_{lap}} \Delta t_i \tag{4.6}$$

where x_{lap} is the final distance of the lap.

Note: The value of x_i goes from 0 to x_{lap} and can be calculated directly from the iteration number (x_i = i - 1). Hence, when the simulation stops at i = x_{lap}, the value of x_i is one metre short of the final race distance. This is so because there are one less track segments than there are distance points.

For a better understanding of the algorithm behind the simulation of the vehicle, the flowchart diagram of Figure 4.2 was drawn. It includes the main processes and flow of information for an easy read of the steps taken to calculate the vehicle's final energy consumption for one lap. It should be noted that the procedures used to plot the vehicle's velocity curve, as well as the power and torque profiles, were not included in the flowchart because they would unnecessarily complicate the diagram without adding any value.

The three shapes used to build the flowchart of Figure 4.2 are the basic and most common symbols for this type of diagrams. These are:

Process (Rectangle): The backbone of any flowchart. Shows a process, task, action or operation to be done.

Input / Output (Parallelogram): Indicates the user data inputs and the outputs of the program.

Decision (Diamond): Indicates a question or branch in the process flow. Used to split the flowchart into multiple possible paths.

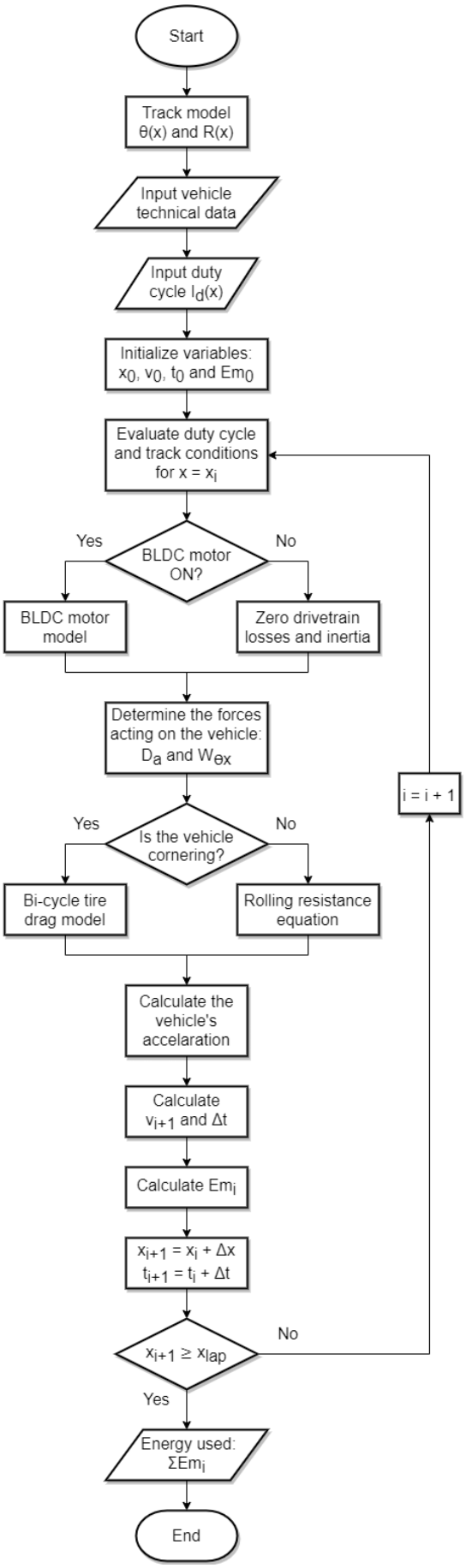

Figure 4.2 - Flowchart of the vehicle's simulation algorithm.

4.4.2 Tire Drag Surface

To avoid solving the full set of equations from Eq. (3.20) to (3.28) for the bi-cycle model each iteration, which includes a system of eight equations to be solved simultaneously, the tire drag was mapped as a function of turn radius and vehicle velocity. To be able to do this simplification, every other variable must be assumed constant, i.e., the distribution of weight on the front and rear wheels is constant and the weight of the vehicle normal to the road does not change with slope angle. However, in the case of the vehicle studied, these simplifications have little to no impact on the overall tire drag. Hence, the resulting map, seen below in Figure 4.3, is very accurate.

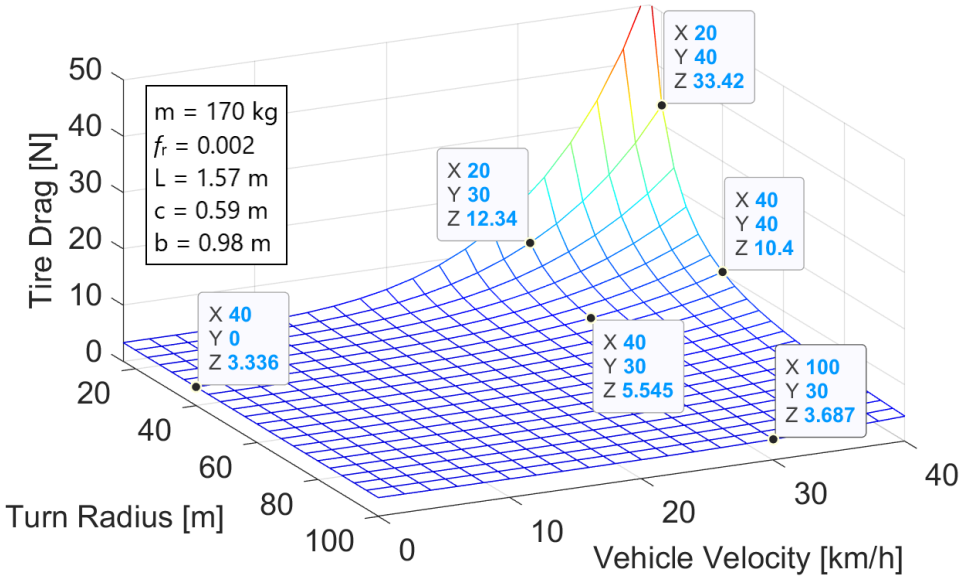

Figure 4.3 - Tire Drag Map in relation to turn radius and vehicle velocity. The coordinates X, Y and Z are the Turn Radius, Vehicle Velocity and Tire Drag, respectively.

To generate the map above, the bi-cycle model was solved for velocities up to 40 km/h (maximum velocity allowed during the race) and for turn radii between 16 and 100 metres. These turn radii limits were chosen because the minimum turn radius of the London 2016 track is around 17 metres and for values above 100 metres the effect of cornering drag is negligible and one can assume the vehicle is traveling in a straight line, where the tire drag is calculated using Eq. (3.15). It should be added that whenever changes are made to the tires, vehicle weight and/or dimensions, a new tire drag map should be calculated with the new specifications.

Applying this method enabled the simulation to run around 10 times faster than when the full bi-cycle model equations were solved.

4.4.3 Dynamics Model Validation

Although often disregarded, the validation of the model is one of the most important steps when building any model. It ensures that the results and conclusions taken from the subsequent simulations are meaningful and can presumably be applied to the real system being simulated.

To validate the model described in 4.4.1, it was compared to the electric vehicle drive model developed in article [56]. This was accomplished by comparing the simulated driving cycle with the one used in the article (EUDC – Extra Urban Driving Cycle), using the same vehicle specifications (Table 4.1) and the same torque profile calculated in the article (Figure 4.4). It should be noted that this thesis' model and the model from the article are in a way the reverse, while the first uses a torque profile to simulate the vehicle velocity the second uses a driving cycle to simulate the torque.

Table 4.1 - Vehicle specifications used for validation [56].

Specification	**Value**
Mass of the vehicle	1500 Kg
Gear Ratio	8
The efficiency of the gear system	97%
The radius of the wheel	0.315m
Motor Inertia Constant	0.02 Kg-m^2
Slope	0
Aerodynamic drag co-efficient	0.4
Coefficient of rolling resistance	0.02
Vehicle Frontal Area	2.2 m^2

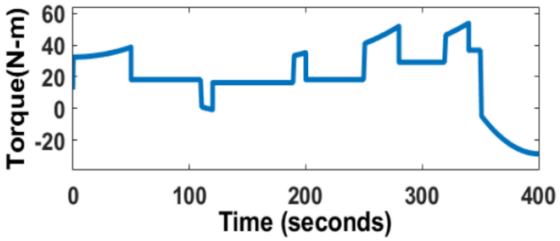

Figure 4.4 - Torque profile used for validation [56].

After doing the required changes for the algorithm to read a torque vector as a function of time instead of distance and inserting the above vehicle specifications and torque profile (blue line) into the program, the driving cycle was simulated. The resulting simulation is shown in Figure 4.5.

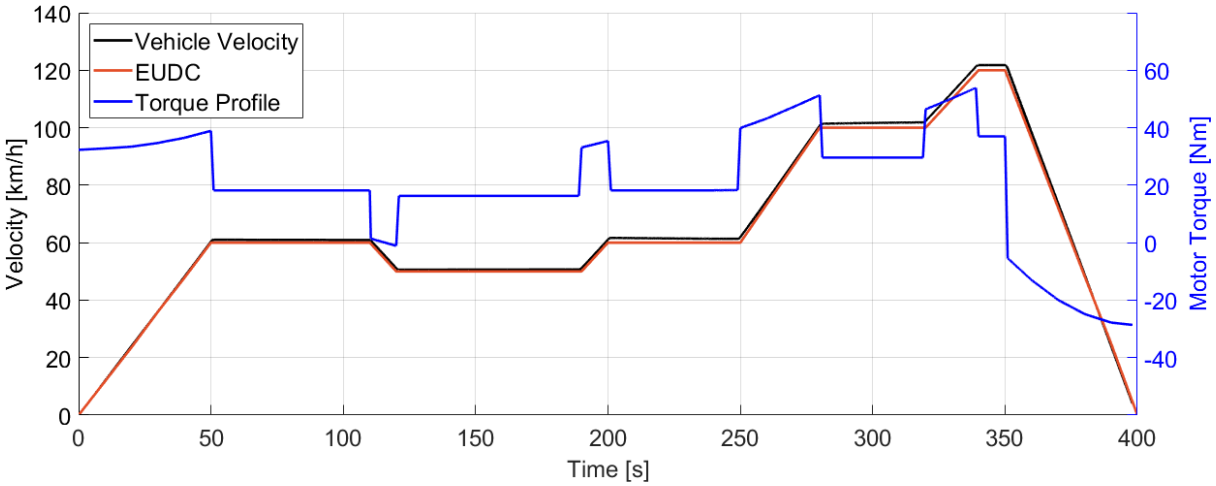

Figure 4.5 – Model validation using the data from Table 4.1 and Figure 4.4.

The results obtained in the validation simulation clearly show that the algorithm is working properly. The vehicle velocity overlaps the EUDC almost perfectly, with a maximum error of around 3%. The small deviation is most likely caused by data collection errors due to the low accuracy of the graph of Figure 4.4, from where the torque profile was extracted.

4.5 Fuel Cell to Motor Models

The present section describes the selected fuel cell to motor models and their implementation with the model of Section 4.3. The fuel cell efficiency will also be discussed briefly at the end of this section.

The fuel cell to motor model is what closes the gap between the hydrogen consumption, which is ultimately what is to be minimized, and the motor to wheel model developed in the previous section. These FC-motor models run in parallel with the motor to wheel model, as they use the data it provides for the motor energy consumption and input power to calculate the energy output and hydrogen consumption of the fuel cell.

Of the four configurations introduced in Section 2.2, only two FC-to-motor models will be analysed in detail in this section. One is the active fuel cell configuration of Section 2.2.1 and the other, the active parallel hybrid of Section 2.2.3. Both semi-active hybrid topologies, mentioned in Section 2.2.2, will not be tested for the vehicle's powertrain due to their disadvantages, when compared to the fuel cell active and active parallel hybrid configurations:

FC semi-active hybrid (Figure 2.10 (b)) – The supercapacitor is mostly unused, making it very similar to the FC active system, except with the added cost and weight of the supercapacitor.

Parallel semi-active hybrid (Figure 2.10 (a)) – This configuration might be of more interest than the FC semi-active hybrid because of the higher energy usage of the supercapacitor and its synergy with the fuel cell. However, it is less efficient than the FC active system and less controllable than the parallel active hybrid. Nevertheless, many of the conclusions reached in this work from analysing the FC active and the parallel active hybrid should be valid for this topology as well, meaning it could be a great choice for a good compromise of performance, cost and complexity.

4.5.1 Fuel Cell Active Model

The FC active model (Figure 2.9) is very simple and straightforward: the energy consumed by the electric motor E_M is simply divided by the efficiency of the DC-DC converter to calculate the energy that the fuel cell "gave" the system E_{FC}. To determine the amount of hydrogen consumed, in Joules, the energy output of the fuel cell, measured at each one metre segment, is divided by its efficiency, which is determined in function of the FC's average power output per segment. The hydrogen consumed by the fuel cell can be easily converted from Joules to kg or m^3 with its NCV and density (Table 1.2).

A schematic of the energy flow for this model is given in Figure 4.6. The arrows represent the flow of energy in the system, which slightly decreases as it goes through the powertrain components, as a consequence of their efficiency.

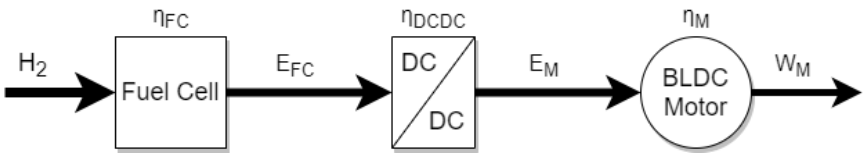

Figure 4.6 - Fuel Cell active configuration energy flow.

Following the direction of the energy flow arrows, the model is represented by equations (4.7) and (4.8):

$$E_{FC,i} = E_{H_2,i} \cdot \eta_{FC}(P_{FC,i}) \tag{4.7}$$

$$E_{M,i} = E_{FC,i} \cdot \eta_{DCDC} \tag{4.8}$$

4.5.2 Parallel Active Hybrid Model

The parallel active hybrid model (Figure 2.11) is moderately more complex than the FC active one. The introduction of the supercapacitor in the powertrain introduces a new degree of freedom to the system, requiring the implementation of a control strategy to determine the flow of energy. For this model, the control of the energy flow is driven by the energy consumed and the average input power of the motor, as well as the state of charge of the supercapacitor, at each iteration.

As in the previous model, following the energy flow arrows, the energy downstream of a component, is calculated by multiplying the energy upstream of the component by its efficiency. However, since there is energy storage in the supercapacitor and there are multiple paths for the energy flow, certain rules must be established for the model to work as intended (control strategy).

The schematic of the energy flow for this model is given in Figure 4.7. In this configuration, energy can flow in and out of the supercapacitor branch, which means that it flows through the SC's DC-DC converter in both directions, losing more energy due to its efficiency. If regenerative braking is used, the flow arrow between the BLDC motor and the junction (circled cross used to connect the energy flow paths) is bi-directional.

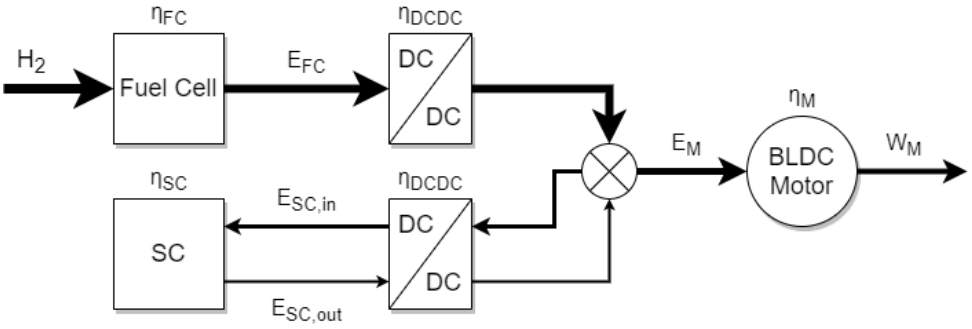

Figure 4.7 - Parallel active hybrid configuration energy flow.

Following the direction of the energy flow arrows, the equations that describe the model are:

Eq. (4.7)

$$E_{SC,i+1} = E_{SC,i} + E_{SC_{in},i} \cdot \eta_{SC} - E_{SC_{out},i} \tag{4.9}$$

$$E_{FC,i} \cdot \eta_{DCDC} + E_{SC_{out},i} \cdot \eta_{DCDC} - E_{M,i} - \frac{E_{SC_{in},i}}{\eta_{DCDC}} = 0 \tag{4.10}$$

where equation (4.9) describes the evolution of the usable energy stored in the supercapacitor, and equation (4.10) the energy balance in the junction, which must be equal to zero since, other than the energy that flows in and out of the powertrain components around it, there is no energy loss or gain.

The control strategy shown in Figure 4.8 was used to simulate the behaviour of the powertrain as it responds to the change in the power requested by the electric motor. As mentioned, this model was designed to run in parallel with the motor to wheel model and, as such, it is also a discreet model.

Since the control input of the FC-motor model is the energy consumed by the electric motor per iteration, as determined by the motor to wheel model, the parallel active hybrid model uses energy per iteration for its calculations. This might not be practical to use in the control of the real vehicle's powertrain, however, the equations used in the model can be easily converted to use with power instead of energy, simply by dividing the energy flow per iteration by the time of the iteration, which is also provided by the motor to wheel model. The equations and relations of the model remain basically the same.

The main goal of the control strategy used is to maintain the power output of the fuel cell constant at its maximum efficiency operating point. Furthermore, it also guarantees that the state of charge of the supercapacitor ends the lap at a value equal or slightly above the value at the beginning of the lap. This requirement comes from a competition rule for the powertrain which states that, at the end of the run, the SOC of the supercapacitor must be equal or higher than at the beginning of the run (Appendix A). Considering the vehicle model simulates only one lap of the run, and the run is a repetition of identical laps, this solution was considered the best to minimize energy consumption and supercapacitor size.

The simulation of the fuel cell to motor model runs without known values for the energy storage capacity of the supercapacitor. Hence, the specifications of the SC are also an output of the model. This is achieved by starting the simulation with a symbolic value of the energy stored in the SC equal to zero. Then, as the simulation progresses, the maximum (positive) and minimum (negative) values of the energy stored in the supercapacitor are registered, yielding its minimum required capacity according to Eq. (2.7), which assumes a 75% capacity usage. In this way, the driving strategy optimization not only minimizes the energy consumed, but also gives the requirements needed for the supercapacitor.

To calculate the energy input or output of the SC, Eq. (4.10) is used with the output or the input equal to zero, respectively. The energy stored in the supercapacitor uses Eq. (4.9) in a similar way.

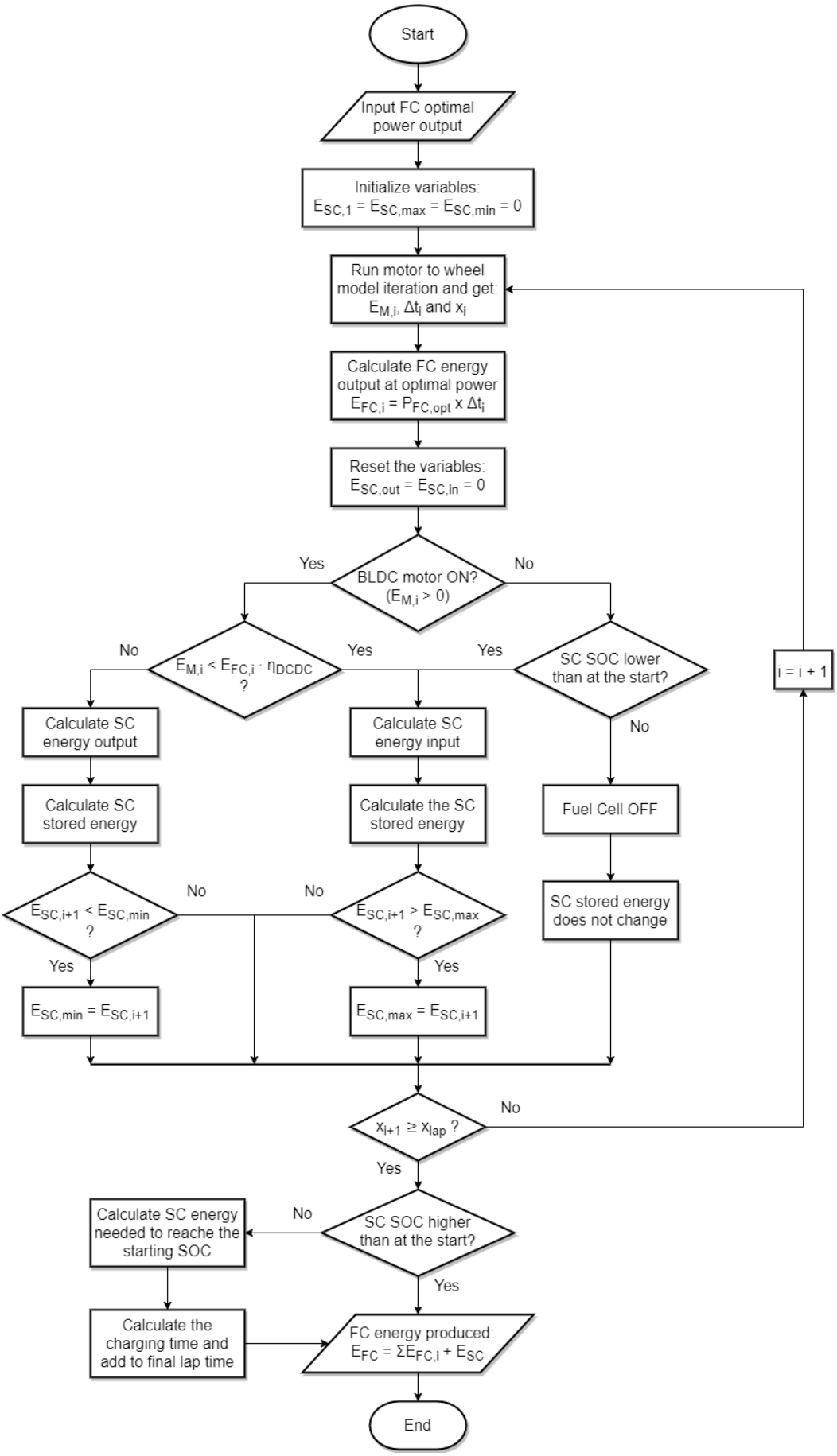

Figure 4.8 – Flowchart of the parallel active hybrid model.

4.5.3 Fuel Cell Hydrogen Consumption

For the fuel cell hydrogen consumption, the values provided by the manufacturer were used because no mathematical model of the fuel cell was developed. However, for the best results, it is recommended that the acquired fuel cell is rigorously tested to obtain the real performance curves. Then, a statistical model of the fuel cell can be built and used with the vehicle model, so the best and most realistic results possible are achieved.

The used fuel cell hydrogen conversion efficiency, shown in Figure 4.9, was extracted from the "average fuel consumption" values (blue line) given by the manufacturer in the fuel cell's manual [57].

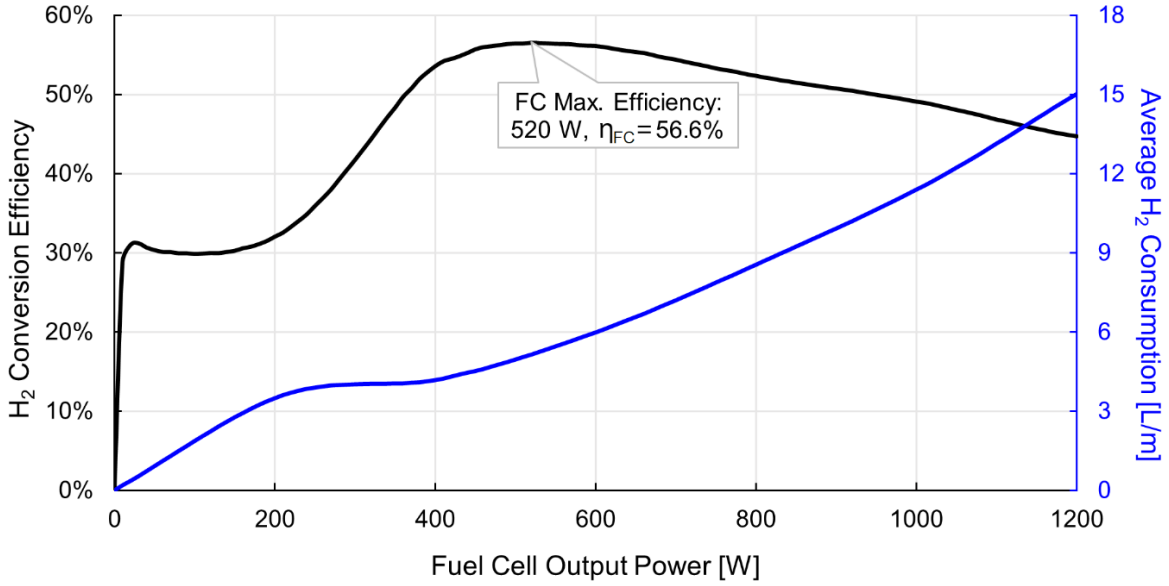

Figure 4.9 – Horizon H-1000XP fuel cell performance versus power output.

5 Driving Strategy and Powertrain Design

The optimization of the mission the vehicle is designed to complete is one of the most important steps to achieve the best possible performance. Even the most optimized and fine-tuned vehicle imaginable will perform poorly if the driving strategy is inadequate.

To simplify and make the optimization problem manageable, the optimization of the driving strategy was done assuming that, independently of the results given by the optimization, the powertrain (from fuel cell to motor) guarantees the availability of sufficient power and energy. In this way, the powertrain is not a constraint of the optimization problem but is rather an output of the same, i.e., the optimized driving strategy will dictate the requirements that the powertrain needs to fulfil.

To attain higher energy efficiencies, the optimization of the driving strategy and the selection of some of the powertrain components, e.g., electric motor and transmission, was done simultaneously. This approach was chosen to maximize the synergy between components and the optimized driving strategy.

5.1 Optimization Problem Formulation

An optimization problem (OP) is described by the objective function to minimize or maximize, the constraints it is subjected to and the relevant system or model. Considering that the prime goal of the Shell Eco-marathon competition is to achieve maximum energy efficiency, one of the most direct and commonly used objective functions is the minimization of the energy consumption of the motor, E_M, for which the optimization problem can be written as:

$$\min_{I_d(x)} E_M\big(I_d(x)\big) \tag{5.1}$$

s.t.

$$t(x) \in \left[0, t_{lap}^{max}\right] \tag{5.2}$$

$$v(x) \in [0, v^{max}] \tag{5.3}$$

$$|F_x(x)| \leq F_x^{max}\big(W_r(x)\big) \tag{5.4}$$

$$|I_d(x)| \leq I_d^{max}\big(v(x)\big) \tag{5.5}$$

However, even though optimizing the energy consumption of the electric motor without considering the rest of the powertrain gives the minimum achievable consumption of the motor-vehicle pair, this can be misleading because, when the rest of the powertrain is added to the problem, the driving strategy optimized for the motor alone may cease to be the optimal for the complete system. For this reason, both optimizations are done to check if this hypothesis is valid and to inspect how much the full vehicle optimization (from fuel cell to wheel) diverges from the motor to wheel optimal one.

One of the main advantages of the models developed in Chapter 4 is that, to change between objective functions, the user needs only to select which of the variables is to be used, i.e., fuel cell or electric

motor energy consumption. This is because the FC-motor model only estimates the energy consumed by the fuel cell and has no influence on the driving cycle, i.e., for a given duty cycle, the velocity profile and the energy consumed by the electric motor remain the same, regardless of the changes made to the FC-motor model. Hence, to optimize the energy consumed by the fuel cell, the objective function shown in Eq. (5.1) is substituted by:

$$\min_{I_d(x),P_{FC}} E_{H_2}(I_d(x), P_{FC}) \tag{5.6}$$

where P_{FC} is the selected optimal power output of the fuel cell used for the parallel active hybrid (Section 4.5.2). For the FC active configuration (Section 4.5.1), the power output of the fuel cell is directly related to the power input of the electric motor and the FC selected optimal power output is not used.

For the design variable, i.e., the system input, many options are available, e.g., traction force (used in [40]), motor torque (used in [33]), vehicle velocity (used in [58]), etc. The design variable chosen to optimize the driving strategy was the motor input current, I_d, with the vehicle velocity, v, as the output of the system. This decision was based on its ease of use with BLDC motor model (Section 3.5.4) and the significance of the variable, i.e., the motor input current can later be used to control the powertrain of the real vehicle, as it is directly linked to the electromagnetic torque output of the electric motor.

5.1.1 Optimization Problem Constraints

The constraints the optimization problem is subjected to are the same for both objective functions. The first two are imposed by the competition rules, meanwhile the third and fourth come from technical or physical limitations. All the constraints are described in this section.

The first constraint (Eq. (5.2)) can be derived from the main goal of any fuel-economy marathon, which is to achieve the minimum average velocity:

$$\bar{v}^{min} = \frac{N_{lap} d_{lap}}{t_{lap}^{max}} \tag{5.7}$$

where:

$\bar{v}^{min}$ = Lap minimum average velocity; N_{lap} = Number of laps;

t_{lap}^{max} = Time limit of the race; d_{lap} = Length of one lap.

From equation (5.7) it is easy to see that, to achieve the minimum average velocity, the time at the end of the race should be the maximum accepted by the rules, resulting in the first constraint of the optimization problem:

$$t(x_{lap}) \leq t_{lap}^{max} \tag{5.8}$$

The second constraint (Eq. (5.3)) comes from a competition rule which states that the vehicle velocity can never be greater than 40 km/h. However, since the goal of the optimization problem is to minimize the average velocity, this constraint should not have any influence on the final optimized driving strategy.

The third and fourth constraints are caused by the limits of the traction force available at the wheel (Eq. (5.4)) and the motor maximum input current (Eq. (5.5)). The maximum traction force can be calculated by equation (3.4), and the maximum input current is determined by the motor's limits of operation.

5.1.2 Discretization of the OP

The optimization problem formulation described in Section 5.1 is in the continuous domain. Thus, to apply the OP to the discrete vehicle models developed in Chapter 4 and use numerical optimization algorithms, it must be converted to a discrete domain. Other than the objective functions, the equivalent discrete OP is trivial to formulate since the only difference is that the continuous distance 'x' is substituted by the iteration number, i.

The discrete objective function is different depending on the model used.

For the energy consumed by the electric motor alone:

$$\min_{I_{d_i}} E_M(I_{d_i}) = \min_{I_{d_i}} \sum_{i=1}^{N} E_{M_i} \tag{5.9}$$

For the fuel cell active model:

$$\min_{I_{d_i}} E_{H_2}(I_{d_i}) = \min_{I_{d_i}} \sum_{i=1}^{N} \frac{E_{M_i}}{\eta_{FC}(P_{FC_i}) \cdot \eta_{DCDC}} \tag{5.10}$$

For the parallel active hybrid model:

$$\min_{I_{d_i}, P_{FC}} E_{H_2}(I_{d_i}, P_{FC}) = \min_{I_{d_i}} \sum_{i=1}^{N} \frac{E_{M_i} + \frac{E_{SC,in_i}}{\eta_{DCDC}} - E_{SC,out_i} \cdot \eta_{DCDC}}{\eta_{FC}(P_{FC}) \cdot \eta_{DCDC}} + E_{SC_N} \tag{5.11}$$

where i is the sample or iteration, the distance travelled is given by $x_i = (i - 1) \cdot \Delta x$ and N is the number of samples ($x_{lap} = x_N = N \cdot \Delta x$). $P_{M,i}$ is the motor input power and t_i is the time at x_i, counting from the start of the lap.

5.2 Optimization Strategies

One of the biggest deciding factors to achieve an efficient driving strategy is the optimization strategy (OS) used to determine where on the track and how much torque the motor produces. The optimization strategy is ultimately what determines the way in which the vehicle is controlled, i.e., maintaining an average velocity, accelerating or freewheeling, depending on the track section, etc. Since there are many ways of controlling the motor torque other than the used motor input current, and the optimization strategies discussed being transversal to almost all of them, the general term duty cycle will be used.

In this section, the main optimizations strategies used by other Shell Eco-marathon teams, as well as the one developed in this thesis, will be discussed and compared.

5.2.1 Prevalent Optimization Strategies of SEM

The main methods used or that have been used by other SEM teams or for similar applications are:

Fixed Sections: Simple “brute-force” strategy, where the duty cycle is evaluated in predefined sections, reducing the effective number of elements that the optimization algorithm has to evaluate. However, this strategy can give poor results because it is very difficult to predict where to break up the track effectively and, as the number of sections increases to improve the results, so does the computational time, exponentially. Even so, this strategy can be useful for simple tracks where the change in road grade is very small [59], [60]. Heuristic optimization algorithms, such as particle swarm optimization and genetic algorithms, are commonly employed to solve this type of optimization problems.

Average Velocity: Another simple but effective strategy is to control the vehicle speed according to preselected minimum and maximum velocities for the run. The duty cycle for accelerating can be kept the same or can vary across the sections, e.g., higher duty cycle when accelerating from the start-line. Many SEM teams have used this strategy, or some derivation of it, to some extent [58], [61]–[63]. The optimization algorithms used for this method are usually the same as in the Fixed Sections method.

Dynamic Programming: A more advanced method to generate the duty cycle is the use of a dynamic programming optimization algorithm to evaluate the optimal driving strategy. This method has the advantage of giving the global optimal solution of the optimization problem [64]. However, since the computational complexity rises exponentially with the number of states and inputs [65], several simplifications must be adopted to keep the computational time acceptable, making the resulting solution diverge from the true global optimal solution. Even so, this method produces excellent results and is used by many teams as a benchmark to create or compare their driving strategies [34], [40].

Of the three discussed methods, the dynamic programming approach is by far the one that offers the best results. However, the resulting duty cycle is usually highly fluctuating and, for that reason, often is impractical to implement and must be further simplified to create a usable driving strategy. This was exactly what the PAC-Car II team did for their driving strategy with high success, mainly by recognizing that at some sections of the track the vehicle was approximately at a constant velocity or accelerating and controlling the vehicle speed accordingly [40]. The PAC-Car II achieved the world-record for fuel efficiency in 2005, which stood for 13 years.

5.2.2 New Optimization Strategy

After investigating and testing all three of the optimization strategies discussed in the previous section, and finding that none satisfied all the desired objectives, a new unique optimization strategy was developed for the vehicle. The main objectives for the new strategy are:

1. Effectiveness – The resulting optimized driving strategy must be competitive;
2. Versatility – It can be used for any track;
3. Ready-to-use – The generated duty cycle can be directly used for the driving strategy;
4. Customizable – The number of “motoring” sections is defined by the user.

The new optimization strategy, which will also be referred to as “Adaptive Sections”, can be considered an upgraded version of the Fixed Track Sections method introduced in Section 5.2.1. Since, in addition to the independent duty cycle for each section, this new method dynamically defines the sections by specifying the location, x_k, and length, d_k, of each of the “active” sections, as is shown in Figure 5.1.

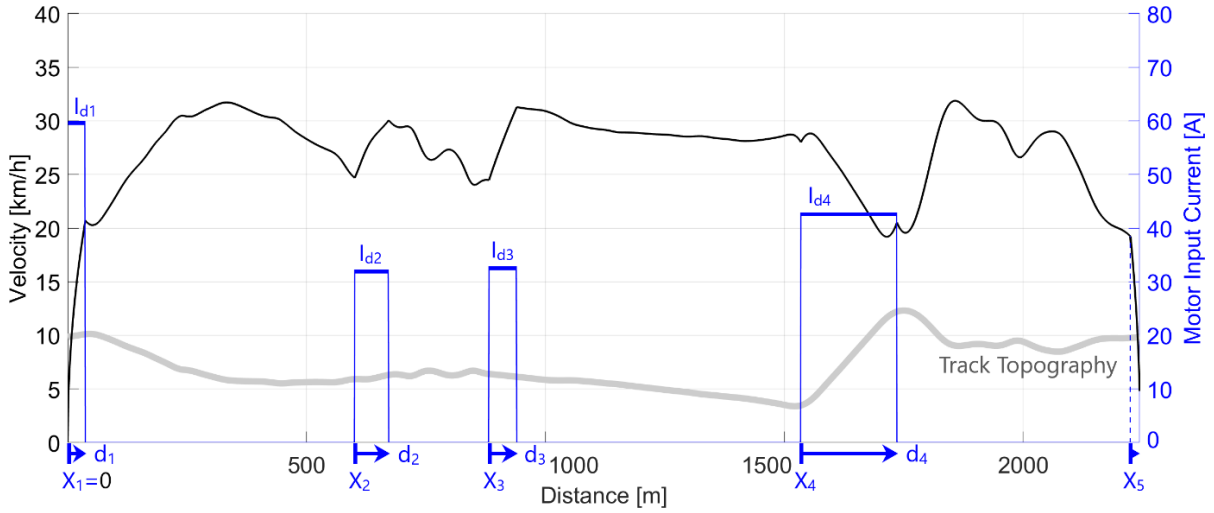

Figure 5.1 – Example of the Adaptive Sections strategy with five active sections (four motoring and one braking).

For the five sections example shown in Figure 5.1, the duty cycle data for the optimization problem is:

$$DutyCycle = \left[x_2, x_3, x_4, x_5, d_1, d_2, d_3, d_4, I_{d_1}, I_{d_2}, I_{d_3}, I_{d_4}, I_{d_5}\right] \tag{5.12}$$

The values for x_1 and for d_5 do not appear in the duty cycle vector because they coincide with the start and finish line distances. Also, the value for the last motor input current variable, I_{d5} in the five sections example, is negative to generate a braking torque and, if regenerative braking is considered, the recuperated energy is subtracted to the total energy consumption of the lap.

Since the user can select the number of active track sections used in the optimization N, the general vector for the duty cycle is represented by:

$$DutyCycle = \left[x_2, \dots, x_N, d_1, \dots, d_{N-1}, I_{d_1}, \dots, I_{d_N}\right] \tag{5.13}$$

For this optimization strategy, new constraints need to be added to the optimization problem of Section 5.1. These constraints ensure that the N sections do not overlap and are all within the track range.

$$d_1 \in \,]0, x_2[\tag{5.14}$$

$$x_2 + d_2 < x_3 \tag{5.15}$$

$$\vdots$$

$$x_{N-1} + d_{N-1} < x_N \tag{5.16}$$

$$x_N \leq x_{lap} \tag{5.17}$$

This new optimization strategy makes it possible for the optimization algorithm to change the duty cycle value, position and length of the sections dynamically to adapt the driving strategy to the track’s topography and shape, which can clearly be observed in the example shown in Figure 5.1.

5.2.3 Optimization Algorithm

Having established the optimization problem, an optimization algorithm must be selected to perform the optimization task. For this, several algorithms available in MATLAB's Optimization Toolbox were evaluated on the quality of their results and computational run time, i.e., their performance and efficiency. Of all the algorithms tested, which include Genetic Algorithm (GA), Particle Swarm (PSO), Pattern Search, Surrogate Optimization and fmincon, only the first two (GA and PSO) showed real promise in solving the optimization problem efficiently. However, due to the discrete nature of the optimization problem, and the inability of MATLAB´s PSO algorithm to handle integer decision variables, the Mixed Integer GA (a GA variant for integer and mixed integer constrained optimization problems – also available in MATLAB's Optimization Toolbox), proved to be the best choice to solve the OP.

An introduction to the genetic algorithm used to solve the OP is presented in Appendix L.

5.3 Powertrain Design

In this section, all the remaining design considerations of the powertrain and the driving strategy will be discussed and defined according to the optimization results given by the models developed in this thesis. The order of appearance of the topics discussed and the decisions taken in this section aims to preserve the logic and sequence of the decision-making process used to reach the final powertrain design. The vehicle specifications used for the simulations are shown in Appendix M.

5.3.1 Fuel Cell Selection

The fuel cell selected for the vehicle is Horizon's H-1000XP, shown in Figure 5.2. It is a high efficiency system developed specifically for Shell Eco-marathon Urban Concept vehicles that has proven itself with several vehicles achieving podium placement, including several wins. This system is most likely the best choice for the team since it is purposefully customized for the competition and also comes with every component needed to plug it on the vehicle and go.

Figure 5.2 - Horizon fuel cell system, image from [66].

The fuel cell is an open-cathode PEMFC with a nominal power output of 1 kW, it has a voltage range of 25V to 48V and the full system weighs approximately 6.8kg. The fuel cell consumption rate and efficiency for different power outputs is shown in Figure 4.9. More information on the fuel cell on [57].

Other fuel cells from other manufacturers were also investigated. However, none showed the potential of the H-1000XP and most of them were not a complete system and would require the purchase of many other components, which are already included in the H-1000XP package from the get-go.

5.3.2 Number of Active Sections

The first driving strategy design consideration chosen to optimize is the number of active sections used in the Adaptive Sections optimization strategy (Section 5.2.2). To do this, the optimization algorithm was used in the "electric motor alone" mode for three and up to eight active sections. This mode was selected to analyse the minimum achievable energy consumption of the vehicle-motor system.

As expected, the optimal energy consumed per lap decreases as the number of active sections used in the driving strategy is increased, as can be seen in Figure 5.3. This result is explained by the vehicle having more flexibility to adapt to the track as the number of active sections increases. However, it was observed that for more than five active sections the minimum energy consumed per lap remains practically constant and there is no real advantage in further increasing the number of active sections.

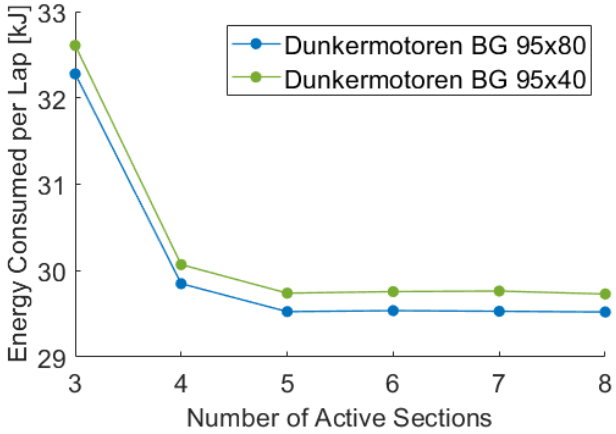

Figure 5.3 - Optimization of the number of active sections of the driving strategy for the Dunkermotoren BG 95x80 and BG 95x40 motors with a transmission gear ratio of 8:1 and 11:1, respectively.

Based on this, and since the main objective of this thesis is to maximise energy efficiency, a driving strategy with five active sections (four motoring and one braking) would be the most obvious choice. However, the four active sections driving strategy reduces the number of power cycles used by 25% (from 4 motoring sections to 3) with a minimal increase in energy consumption of around 1%. For this reason, a driving strategy with four active sections is considered to be the best compromise between energy efficiency and fuel cell lifetime. Furthermore, since the model used does not take into account the transient of operation of the fuel cell, the fact that one less power cycle is used per lap can make the four active sections driving strategy the actual best option in terms of fuel efficiency.

The number of motoring cycles per lap should not constitute a problem for the fuel cell since its use is not intensive and only at partial load [57].

5.3.3 BLDC Motor Selection

To select the best BLDC motor for the vehicle, the energy consumed per lap by the three pre-selected BLDC motors (Section 3.5.2) was evaluated for different transmission gear ratios by running the driving strategy optimization algorithm with gear ratios ranging from 3:1 to 16:1. The data generated is plotted in the graph shown in Figure 5.4, where it can be observed that the Dunkermotoren BG 95X80 has the biggest potential for fuel efficiency for the majority of gear ratios, with the optimal gear ratio of 11:1.

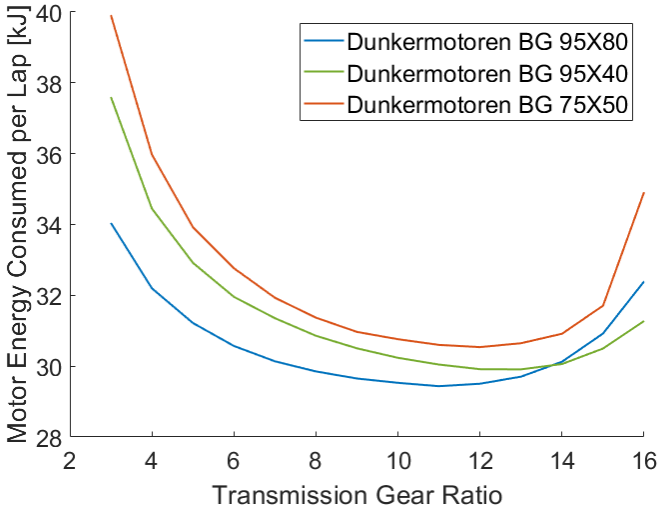

Figure 5.4 - Comparison of the electrical energy consumption per lap of the Dunkermotoren BG 95X80, BG 95X40 and BG 75X50 models, for different transmission gear ratios.

Even though this analysis strongly indicates that the BG 95X80 is the best of the three motors evaluated, further examination is required to confirm the motor selection. This is because the comparison displayed in Figure 5.4 only evaluates the energy consumption of the motors, i.e., it does not take into consideration the powertrain from fuel to motor and the energy losses associated to it. These losses depend on the input power demand of the motor, which in turn is affected by the transmission gear ratio.

The confirmation of the selected electric motor, the optimal transmission gear ratio and the selection of the best powertrain configuration is handled in the next section.

5.3.4 Powertrain Configuration and Transmission Selection

Comparing the parallel active hybrid and the fuel cell active configurations for the Dunkermotoren BG 95X80 for transmission gear ratios ranging again from 3:1 to 16:1 (Figure 5.5), it can be concluded that both configurations generate very similar results in terms of fuel efficiency, with the parallel active hybrid producing slightly better results for an optimal transmission gear ratio of approximately 15:2. With this knowledge, and considering that the parallel active hybrid has a higher flexibility to respond to changing conditions in the track and/or during the race and that it isolates the fuel cell from the motor electric load, allowing it to work in more favourable conditions and avoiding surges of power that may reduce the fuel cell's life or even damage its performance, the parallel active hybrid was the chosen configuration.

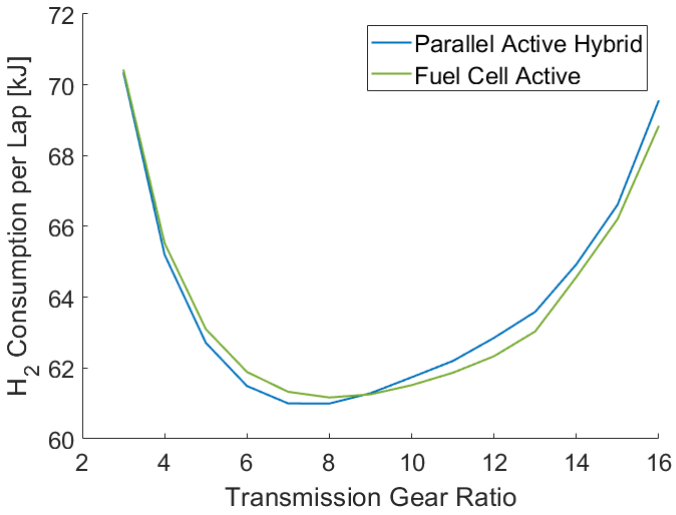

Figure 5.5 – Comparison of the hydrogen consumption per lap of the BG 95X80 motor for powertrains in parallel active hybrid and fuel cell active configurations, for different transmission gear ratios.

Inspecting the data from Figure 5.5 and comparing it to Figure 5.4, it can be observed that the optimal transmission gear ratio of the BG 95X80 motor decreased from 11:1 when only the energy consumed by the motor was considered, to approximately 15:2 where the complete powertrain is simulated to estimate the final hydrogen consumption. This results from the fact that, when the full powertrain (from fuel cell to wheel) is considered, the optimization of the driving strategy attempts to match the motor power input to the optimal fuel cell power output, avoiding the unnecessary use of the supercapacitor DC-DC converter pair that, even as efficient as they are, constitute a source of energy loss. In conclusion, the BLDC motor should be used at considerably lower input power values than in the driving strategy considering electric motor alone, as can be observed in Figure 5.6 where the two optimal driving strategies are shown along with the power input of the electric motor for both cases. It must be added that for the optimization of the driving strategy for the electric motor alone, the estimated hydrogen consumption in Joules per lap, applying the parallel active hybrid powertrain configuration model afterwards, is 68033 J, comparing to 60915 J when the optimization is done taking into account the model of the powertrain in the parallel active hybrid configuration from the beginning.

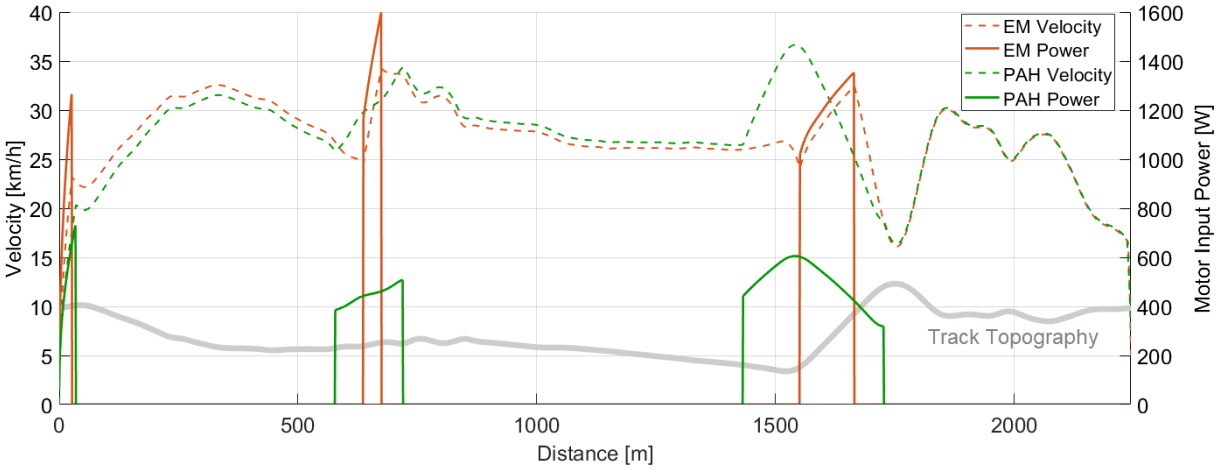

Figure 5.6 – Comparison of the optimal driving strategies for the BG 95X80 as a parallel active hybrid (PAH) and for the electric motor alone (EM).

Finally, to confirm that the Dunkermotoren BG 95X80 has the best performance of the three BLDC motors evaluated using both the FC-motor models (Section 4.5), the same optimization performed for the BG 95X80 shown Figure 5.5 was repeated for the other two motors. The results, including the one already shown in Figure 5.5, are displayed in Figure 5.7 in two graphs, one for the parallel active hybrid configuration (a) and the other for the fuel cell active configuration (b).

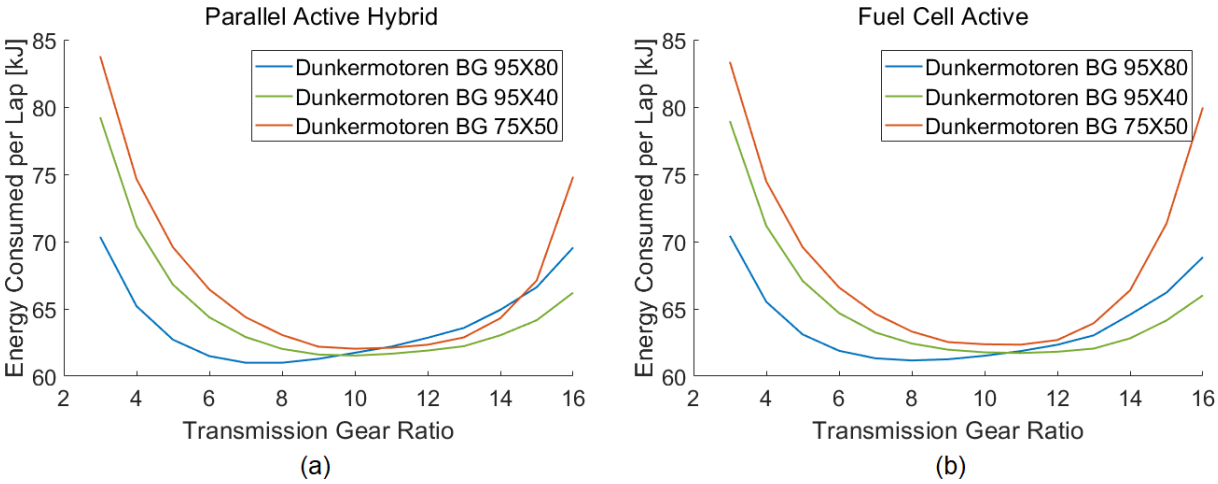

Figure 5.7 – Vehicle energy consumption optimization versus transmission gear ratio for the three motors in the two configuration: (a) parallel active hybrid configuration and (b) fuel cell active.

From these results it can be concluded that the BG 95X80 motor is clearly the best performing motor of the three for the application, if the correct transmission gear ratio is used.

Summarizing the analysis done until this point, the optimal powertrain design uses the BG 95X80 motor in a parallel active hybrid configuration with the fuel cell and the supercapacitor and a transmission gear ratio of 15:2, running a driving strategy with three motoring and one braking sections, for each lap.

5.3.5 Regenerative Braking

One other aspect to consider is if the vehicle should have regenerative braking capabilities or not. At first glance it might seem obvious that it is desirable that it does since the energy recuperated would otherwise be lost as heat in the disk brakes. However, after a deeper analysis the conclusion is that adapting the vehicle to be able to recuperate the braking energy might do more harm than good to the vehicle global efficiency. The main reason is that, even for perfect conditions where the driving strategy is unaltered and all the energy used for braking is recuperated, i.e., no mechanical brakes are used, the energy recuperated amounts to less than 3% of the total energy consumed by the electric motor and, in reality, this value would be considerably lower. The fact that this value is so low makes any slight drop in the vehicle performance caused by regenerative braking or due to its installation not worth having it.

One other element to consider is that a clutch system would be required if regenerative braking were to be used. This is evident after studying what would happen to the vehicle's velocity profile if the drivetrain were still connected to the driving wheel(s) when the vehicle is freewheeling, i.e., the motor is off and the vehicle keeps moving due to inertia and/or the track slope. As can be seen in Figure 5.8, the vehicle keeps losing speed in the motor "off" sections as a result of the electric motor and transmission friction

losses. These losses are so severe that, for the optimized driving strategy with drivetrain losses and regenerative braking to respect the imposed time restriction, the hydrogen consumption would increase approximately 20% compared to the optimal driving strategy with frictionless freewheeling sections and without energy recuperation during braking.

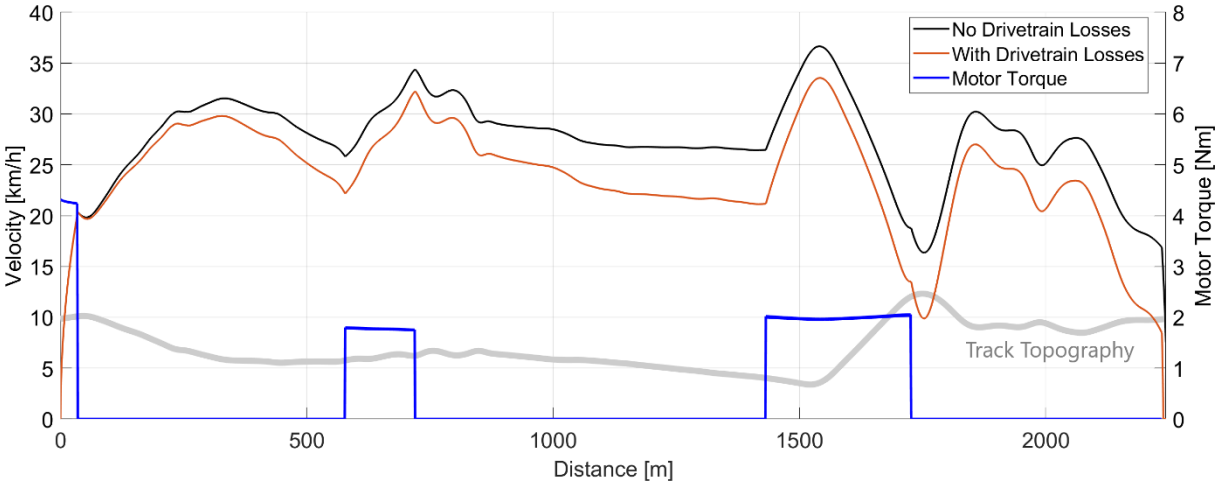

Figure 5.8 – Comparison of the optimal driving strategy with the drivetrain disconnected from the driving wheel(s) during freewheeling and with the drivetrain always connected (transmission gear ratio of 15:2).

If a clutch system is used, it should be positioned in the drivetrain as close to the driving wheel(s) as possible to minimize friction losses. A feasible solution can be a type of clutch or brake system that activates when the electric motor is used, locking the driving wheel(s) to the drivetrain. However, this solution makes the system more complex and, if any losses arise from the use of the clutch, the advantage of using regenerative braking is most likely lost, as previously mentioned.

5.3.6 Supercapacitor Selection

To determine the required capacity of the supercapacitor for the optimal run with the powertrain design selected so far, the maximum and minimum charge levels of the supercapacitor are registered in relation to the state of the SC at the start of the lap. This is explained in detail in Section 4.5.2. For the mentioned driving strategy, the evolution of the energy stored in the supercapacitor is shown in Figure 5.9, as well as the motor input and the fuel cell output power. It should be noted that the SC charge level is measured in relation to a fictitious zero charge, which represents the initial state of the supercapacitor's charge level, i.e., on the starting line of the track.

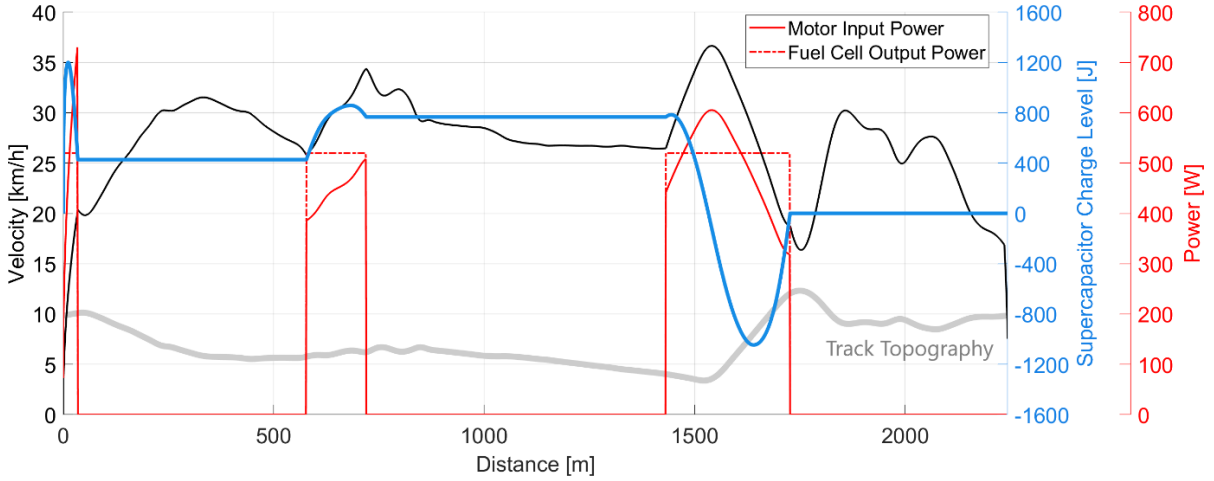

Figure 5.9 – Evolution of the supercapacitor charge level for the optimal driving strategy with the BG 95X80 in a parallel active hybrid with a transmission gear ratio of 15:2.

Examining the evolution of the supercapacitor charge level, it can be noted that, when the fuel cell power output is greater than the electric motor power input, the supercapacitor is generally charging. The only exception to this rule is when the motor input power is just slightly lower than the FC output power and, because of the powertrain's efficiency, the FC output that reaches the motor is lower than what is requested and the supercapacitor steps in to make up for the difference.

The maximum and minimum charge levels of the supercapacitor during the run shown in Figure 5.9 are 1200.5 J and -1046.5 J, respectively. Knowing that 25% of the SC capacity is not used, the minimum required energy storage capacity of the SC is approximately 3000 J. With this value, Eq. (2.5) gives the relation between voltage and capacitance to be used in the selection of the best fitting supercapacitor. For example, for the 1.25 F supercapacitor that can be bought as part of the Horizon fuel cell package, the SC would have to be at approximately 69.3 V to reach the maximum charge required during the lap, which not only surpasses the maximum allowed voltage for the competition of 60 V but is also higher than what the SC can reach. Hence, a higher capacitance supercapacitor should be procured.

5.3.7 Number of Driving Wheels

The last decision to be considered is if the vehicle should have one or two driving wheels, which will be decided based on the necessity of having two driving wheels or not. Therefore, if one driving wheel is sufficient in terms of performance and safety, it will be the preferred choice of the two since the drivetrain is remarkably simpler and lighter.

To verify if one-wheel drive is sufficient, two parameters were evaluated for the optimal driving strategy using the powertrain selected so far. The parameters are the maximum available traction and the added tire drag caused by the turning of the front wheels to compensate for having only one rear driving wheel.

Traction Verification: To check if tractive force available for one wheel is sufficient, the highest tractive force required by the vehicle during the run was calculated with Eq. (3.13) and compared to the maximum available traction determined with Eq. (3.4) for the same conditions, i.e., at the same acceleration, velocity and position on the track. For the optimal run, the maximum registered tractive

force produced by the driving wheel occurs on the starting line during acceleration and is approximately 100 N, which is considerably lower than the maximum tractive force available of approximately 426 N for dry and 266 N for wet conditions (assuming the track surface is asphalt or concrete).

Compensation Tire Drag: Having only one driving rear wheel causes the total tractive force produced by the vehicle to not be in line with its the centre of mass, creating a momentum around the centre of mass that must be counterbalanced by slightly steering the front wheels to the same side of the driving wheel, as shown below in Figure 5.10 for a right-side driving rear wheel.

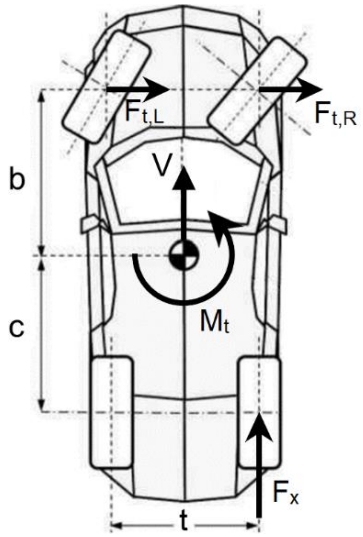

Figure 5.10 - Vehicle one

The equilibrium for the vehicle, when the electric motor is powering the wheel, is described by:

$$M_t = \frac{t}{2} \cdot F_x - b \cdot 2 \cdot F_t = 0 \tag{5.18}$$

where $F_{t,L}$ and $F_{t,R}$ are approximately equal and represent lateral forces produced by the left and right tires counteracting the turning moment M_t generated by the misaligned traction force F_x.

Using the equilibrium shown in Figure 3.4 for one tire, with F_c equal to F_t and the rolling resistive force equal to zero, and applying equations (3.19) and (3.21) assuming small slip angles, the additional tire drag caused by the turning of the wheels, T, can be determined for the sections of the track where the electric motor is used (in Figure 3.4 T is named tractive cornering force and is described as the force needed to counteract the tire resistive forces to maintain the vehicle velocity constant; not to be confused with F_x from Figure 5.10 which is the tractive force produced by the rear wheel propelling the vehicle forward). Finally, since the length of each iteration is equal to 1 metre, the additional energy lost due to having only one driving wheel is equal to the sum of T for every iteration along the track.

For the same driving strategy used before, the energy lost due to the cornering effect of having one-wheel drive is negligible, representing less than 0.06% of the total energy consumed by the electric motor. Also, the maximum slip angle registered is approximately 0.5º, validating the use of the linear relation for small slip angles of Eq. (3.19) for the situation.

To possibly reduce the energy loss even further, the chosen driving wheel should be on the “outside” of the track, i.e., the wheel that will be on the outside of the majority of the corners, in this way, if a motoring section coincides with a corner, the turning momentum generated by the traction force will help the vehicle to corner, which reduces the cornering tire drag. However, this effect is so minimal that it is probably undetectable.

Concluding the analysis done in this section, a one-wheel drive is the best solution since it has a negligible impact on the performance of the vehicle and makes the drivetrain remarkedly simpler when compared to the two-wheel drivetrain, as already mentioned. Hence, the author considers that the best solution for the drivetrain, considering the choice of motor and transmission gear ratio, is a combination of the Dunkermotoren PLG 80 LB planetary gearbox with an 8:1 gear ratio (Figure 5.11) for the first stage and, for the second, a roller chain connecting directly to the freehub (as in a bicycle) with a gear ratio of 15:16, making up the final transmission gear ratio of 15:2. This system considerably reduces the number shafts needed and, since the chain can withstand the movements of the wheel due to it having a suspension system, it avoids the use of universal joints and other complex mechanisms, making the powertrain simple, lightweight and very efficient. Also, it allows for the fine-tuning of the final transmission gear ratio by changing the number of teeth of the roller chain gears, making it possible to adapt the vehicle to any track. A simple schematic of the drivetrain system is also shown in Figure 5.12.

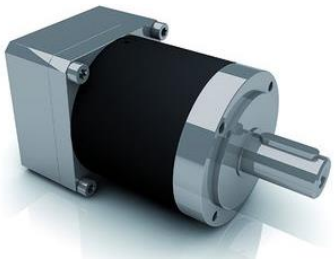

Figure 5.11 - Dunkermotoren PLG 80 LB, 8:1 planetary gearbox [55].

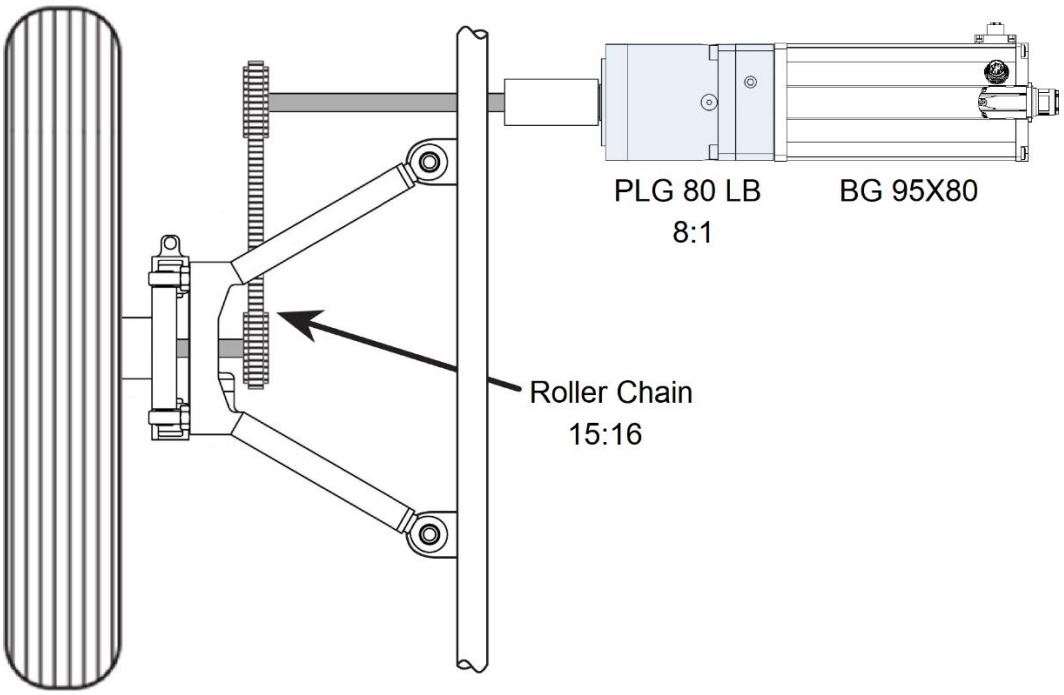

Figure 5.12 - Schematic of the drivetrain system viewed from the top (suspension model from [5]).

5.4 Optimized Driving Strategy

The final optimized driving strategy of the vehicle with the powertrain design considerations of section 5.3, i.e., Horizon H-1000XP fuel cell, BG 95X80 motor, three motoring sections, parallel active hybrid, transmission gear ratio of 15:2, no regenerative braking and one driving rear wheel, for the duty cycle control vector DutyCycle = [578, 1432, 2236, 35, 142, 295, 71.2, 32.9, 36.5, -128.6] is shown in Figure 5.13. The resulting graph shows the velocity profile of the vehicle for one lap, the fuel cell output and motor input power, the motor torque and, for reference, the track topography (which can be read on the velocity axis in meters). For more detailed information about the track topography, see Appendix B.

The hydrogen consumption per lap is 60915 J, which is equivalent to a fuel efficiency of 370.2 km/m^3 of hydrogen (converted using the values from Table 1.2 in Section 1.3.4) and the lap time is 310 seconds, 12.5 seconds less than the maximum time per lap to end the 8-lap race in exactly 43 minutes. This slightly higher lap time was chosen to give some margin for unforeseeable events or conditions during the race, e.g., other vehicle obstructing the track, adverse weather conditions, vehicle malfunctions, etc.

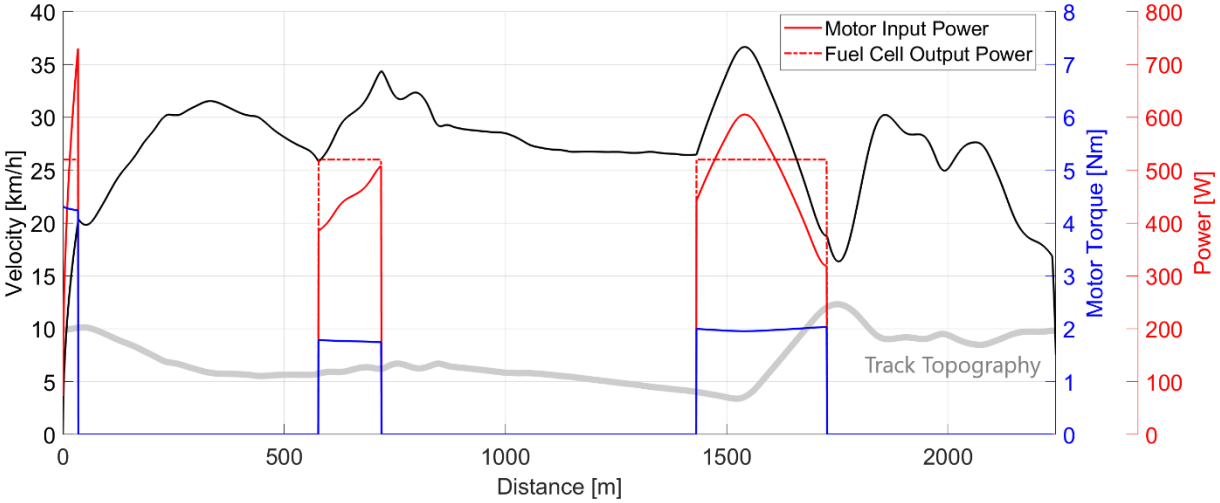

Figure 5.13 - Final optimal driving strategy for one lap of the 2016 London track.

Analysing the graph, it is interesting to observe how the optimization algorithm adapted the duty cycle to the track topography. A similar solution for the driving strategy around the same track was obtained with a different and slightly less optimized method in [32], which gives confidence in the obtained results.

5.4.1 Energy Consumption Breakdown

The energy consumption of the vehicle can be broken-down into the various sources of energy loss that occur along the path energy takes until it reaches its final intended use, i.e., opposing the resistive forces that act on the vehicle. For a better visualization of the vehicle's energy flow, the Sankey diagram of Figure 5.14 was drawn for the optimal driving strategy of Figure 5.13, where at the left is the hydrogen consumption and at the right, the blue paths are the energy spent on the resistive forces that oppose movement and the red paths are the losses due to the efficiency of the powertrain components. It should be noted that, even though driving in a track with a variable grade considerably increases the energy

consumption, it does not appear in the diagram bellow. This is because every time the vehicle goes up a slope, it must come down, cancelling each other out and making the net energy loss equal to zero.

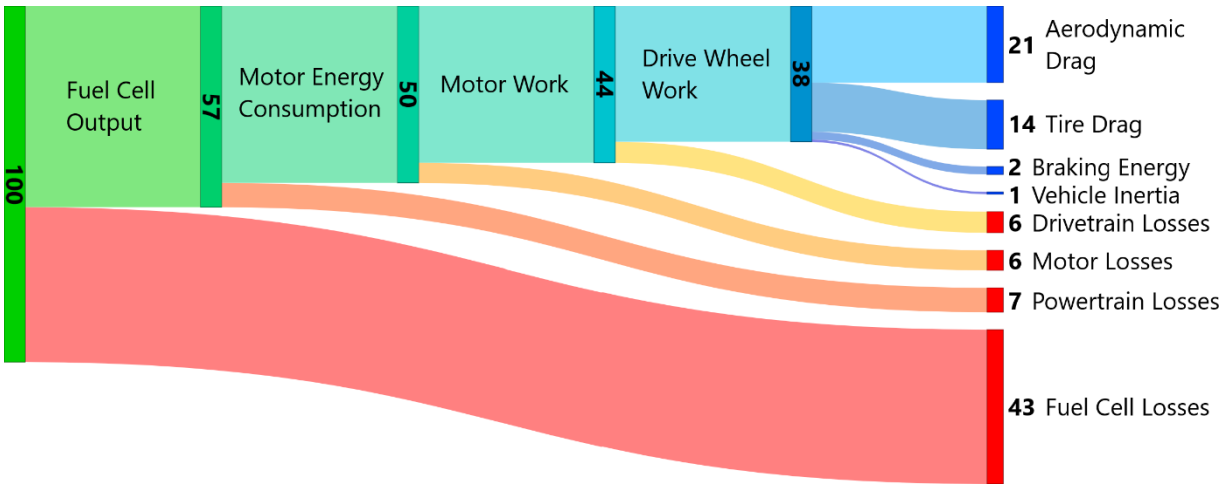

Figure 5.14 – Vehicle energy consumption breakdown for the driving strategy of Figure 5.13.

It is interesting to note that, even though the average cruising speed of the vehicle is between 25 and 30 km/h, which is considerably lower than that of a regular road car, the aerodynamic drag is still the predominant resistive force acting on the vehicle, even considering that the body shape is highly aerodynamic [6]. This shows the importance that aerodynamics have on the fuel consumption and serves as a warning that every change to the vehicle's body surface must be carefully studied to avoid worsening the aerodynamic drag.

After the aerodynamic drag, the resistance caused by the tires under "normal" rolling conditions and when cornering (approximately 11% of the total tire drag), is by far the largest cause of energy loss. Furthermore, special attention should be given to the tires and the steering system to ensure that everything is perfectly lined up and working flawlessly because, if any misalignment or tire wobbling occurs, the rolling resistance increases significantly, easily surpassing the energy loss due to aerodynamics and possibly even ruining the run.

5.4.2 Energy Consumption Compared to an Average Velocity OS

To proof the viability of the optimization strategy described in Section 5.2.2, which is used to generate the optimal driving strategy, an analysis similar to the one shown in Figure 5.5 for the parallel active hybrid was carried out using an average velocity optimization strategy, which has seen widespread use among SEM teams (Section 5.2.1). The powertrain design used is exactly the same as before.

The chosen average velocity optimization strategy consists of a minimum and a maximum velocity under or over which the motor is turned on or off, respectively, a fixed value for the motor input current for when the motor is on, a track distance after which the motor is always off and the braking distance and force to stop the vehicle at the end of the lap. The optimal driving strategy for this average velocity OS is shown in Figure 5.15. It uses a transmission gear ratio of 10:1, minimum and maximum velocities of 25-30 km/h and a motor input current of 41 A.

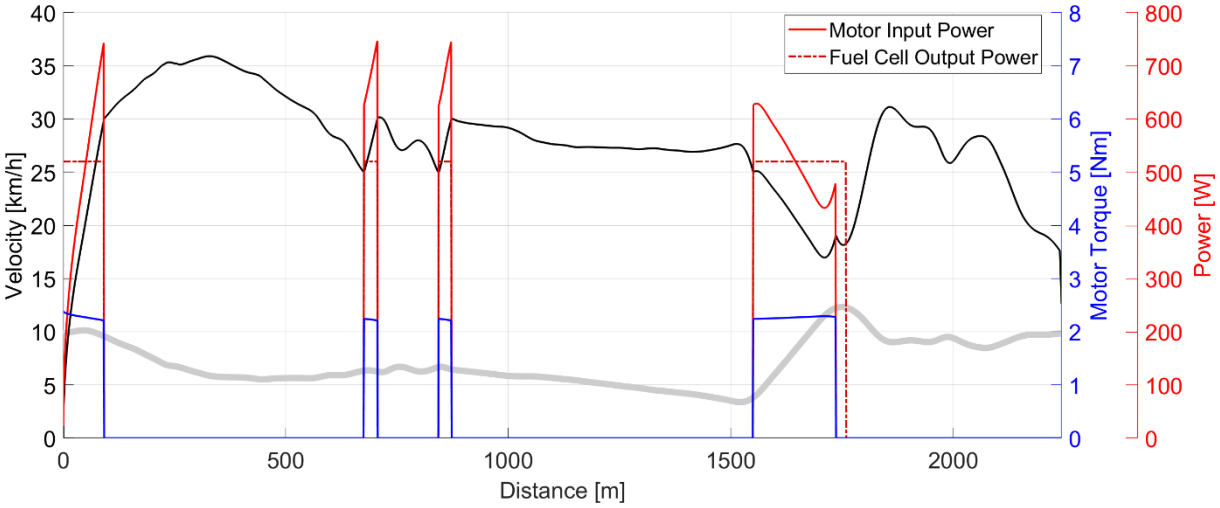

Figure 5.15 – Optimal driving strategy using an average velocity OS.

The fuel consumption obtained with the average velocity OS is 63264 J, which is approximately 4% higher than that of the new OS discussed in Section 5.2.2. This difference is small, however, since the average velocity OS uses more motoring sections than the optimal driving strategy developed with the new OS (Figure 5.13), there should be some impact on the efficiency of the fuel cell, which is expected widen the difference in fuel consumption of the two strategies, as also mentioned in Section 5.3.2.

Another thing to point out is that, even though the average velocity OS efficiently adapts the driving strategy to the SEM London 2016 track, there is no guarantee that the same will occur for a different track. On the other hand, since the new OS proposed in this thesis has a customisable number of motoring sections that are dynamic and adapt to the track, it should have no problem generating optimal driving strategies for any track.

5.4.3 Energy Consumption Compared to Other Teams

If the vehicle discussed in this thesis were to compete in the 2016 London edition of the Shell Eco-marathon, and assuming it was able to perfectly execute the optimal driving strategy of Figure 5.13, it would achieve a second place with a fuel efficiency of 370.2 km/m^3, slightly lower than the winning team's fuel efficiency of 389.3 km/m^3. In fact, analysing Table 1.1 that shows the competition results of that year for the hydrogen urban concept class, it can be seen that the winning fuel efficiency was considerably higher than the other competing teams (39% higher than the second place), showing that expected fuel efficiency of the TFC vehicle, which is just 5% lower than the winning team, would be an excellent result and, with further optimization of the vehicle, it could easily win the competition.

5.5 Sensitivity analysis

In this section, the simulating capabilities of the model developed in Chapter 4 will be used to analyse the impact that modifications to the vehicle's characteristics and to the track conditions have on the energy consumption. To do this, the chosen parameter to be evaluated is changed to values below and

above the initial considered value, e.g., vehicle mass changed from 70 kg to 140 kg, and the new optimal driving strategy will be calculated accordingly, maintaining the other parameters unchanged. The powertrain design used for the sensitivity analysis is the optimal one selected in Section 5.3.

The study developed in this section highlights where the major efforts for the improvement of the vehicle should be focused on and also points out possible areas that are not worth investing in.

5.5.1 Vehicle Mass

The results of the sensitivity analysis done for the vehicle mass, displayed in Figure 5.16, show that the fuel consumption increases linearly with the vehicle mass, as expected. Comparing the expected mass of the vehicle developed in this project of 100 kg (plus a driver of 70 kg) with the maximum and minimum vehicle masses of the vehicles discussed in Section 2.4 (Table 2.3), for a lighter vehicle with 70 kg the fuel consumption would decrease 7.7% and for a heavier vehicle with 135 kg it would increase 9.5%. In other words, the amount of hydrogen consumed is expected to increase 2.7% with each 10 kg increment to the mass of the vehicle.

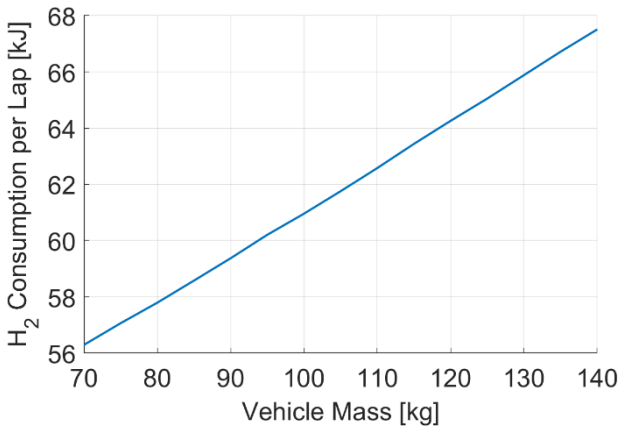

Figure 5.16 – Sensitivity analysis of the fuel consumption to the change of the vehicle mass.

According to the sensitivity analysis displayed in Figure 5.16, the mass influence on the vehicle's fuel efficiency is not as severe as initially expected. This means that, even though it is evident that the vehicle mass should be reduced as much as possible, some upgrades to the vehicle that cause an increase in weight should be adopted because the improve in performance can outweigh the reduction of fuel efficiency due to the weight increase, e.g., the increase in performance of using the BG 95X80 motor comparing with the BG 95X40 outweighs consequence of the weight difference of the motors, even if the differences in performance are small.

5.5.2 Quality of the Tires

One of the reoccurring themes that was encountered during the research of ultra-efficient vehicles is the major role that the tires have on fuel efficiency. It was even found that many of the vehicles that have reached podium placement or even won the SEM use the same specially designed Michelin tires.

The sensitivity analysis for the rolling resistance of the tires, shown in Figure 5.17, clearly reveals why the tires are so important. A mere increase of the rolling resistance from 0.002 to 0.004 causes an increase in fuel consumption of 27%. It should be noted that 0.004 is a very low value of rolling resistance for a tire, roughly half than that of the best energy-efficient car tires available on the market [67].

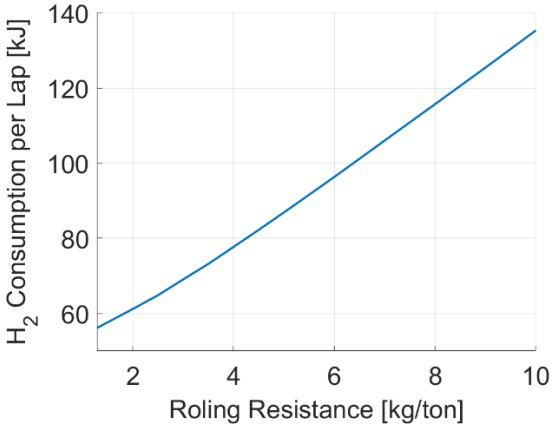

Figure 5.17 – Sensitivity analysis of the fuel consumption to the tires rolling resistance coefficient.

In conclusion, the rolling resistance sensitivity analysis alerts to the heavy influence that the tires have on the vehicle's performance, which makes them one of the most critical components to achieve high fuel efficiencies. Hence, if the goal is to reach the lowest fuel consumption and to compete with the best teams of Shell Eco-marathon, the team should spare no effort to acquire the mentioned Michelin tires and to thoroughly test them to ensure that the maximum possible performance is attained.

5.5.3 Temperature of the BLDC Motor

As temperature increases, all metal conductors suffer from an increase in electrical resistance. This phenomenon can be described by the following expression:

$$R_{s_f} = R_{s_i} \cdot \left[1 + \alpha_{cond} \cdot \left(T_f - T_i\right)\right] \tag{5.19}$$

where R_{sf} is the conductor resistance at a temperature different than the original, R_{si} is the original temperature for which the value of resistance is known (20 ºC for the Dunkermotoren motors) and α_{cond} is the temperature coefficient of resistance of the conductor, which is equal to 0.004 $ºC^{-1}$ for copper [68].

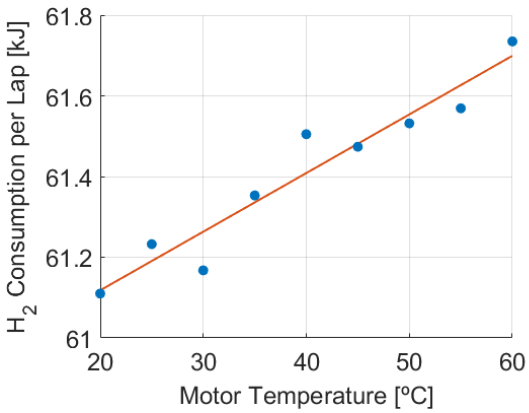

Figure 5.18 – Sensitivity analysis of the fuel consumption to the electric motor temperature.

The sensitivity analysis of the fuel consumption as temperature is increased from 20 ºC to 60 ºC (which is a safe maximum temperature for the electric motor) is visible in Figure 5.18. The data shows a clear and expected trend (approximated by the orange linear trendline in Figure 5.18) of a decrease in fuel efficiency as temperature rises. However, this effect is minimal, with fuel consumption increasing just 1% when comparing the motor at 20 ºC and 60 ºC.

5.5.4 DC-DC Converters Efficiency

Since the totality of the electrical energy output of the fuel cell passes through a DC-DC converter, its efficiency should have a considerable effect on the fuel efficiency of the vehicle. This relation can be seen in the sensitivity analysis of the fuel consumption per lap to the efficiency of the DC-DC converters (two converters are used in the parallel active hybrid configuration) shown in Figure 5.19.

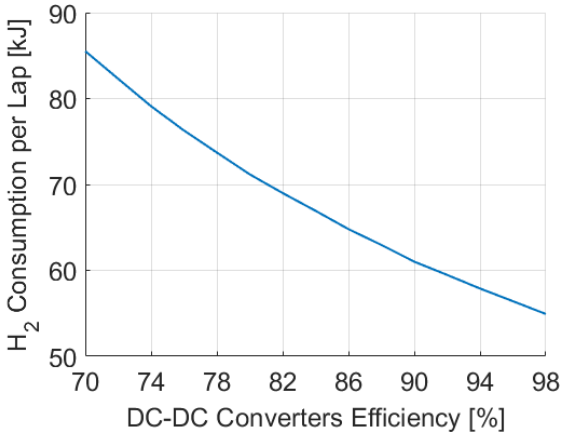

Figure 5.19 - Sensitivity analysis of the fuel consumption to the efficiency of the DC-DC converters.

As can be observed in Figure 5.19, the change in fuel consumption in relation to the efficiency of the DC-DC converters is severe and slightly deviates from a linear relation. This occurs because the energy from the fuel cell can go directly to the motor, passing only once through the “main” DC-DC converter, or it can go to the supercapacitor, where it will pass through the second DC-DC converter two additional times, which is what causes the positive concavity of the relationship. The non-linearity is small because only about 10% of the energy output of the fuel cell goes through the supercapacitor, whereas the rest goes directly to the electric motor, passing only once through a DC-DC converter.

Compared to the assumed converter efficiency of 90%, an increase in efficiency to 96% (+6%) would result in a reduction in fuel consumption of 7.5%, while a reduction to 84% (-6%) results in an increase in fuel consumption of 9.7%. This shows the importance of keeping the converters efficiency as high as possible, giving priority to the main DC-DC converter that is right after the fuel cell, since about 90% the FC energy output goes through it directly into the electric motor.

5.5.5 Supercapacitor Efficiency

As expected, the sensitivity analysis of the fuel consumption in relation to the efficiency of the supercapacitor, presented in Figure 5.20, shows that the efficiency of the supercapacitor plays a minor

role in the total fuel efficiency of the vehicle, varying linearly according to the orange trendline shown. This is because only about 10% of the total energy output of the fuel cell goes to the supercapacitor, as was mentioned in the previous section. For example, comparing a supercapacitor with an efficiency of 80% with one 98% efficient, the fuel consumption reduction is only 2%.

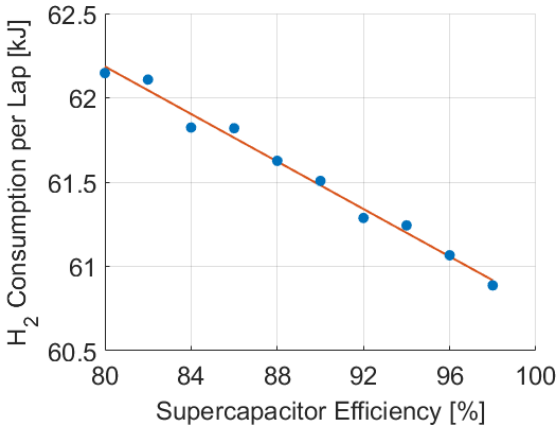

Figure 5.20 - Sensitivity analysis of the fuel consumption to the efficiency of the supercapacitor.

In conclusion, knowing that the supercapacitor's efficiency has little influence on the final fuel consumption, and considering that it is generally a high-efficiency component, the most important considerations when choosing the supercapacitor are its voltage, capacitance and weight. The minimum required capacity of the SC is determined in Section 5.3.6.

5.5.6 Aerodynamic Drag Coefficient

As can be expected from the aerodynamic drag equation (Eq. (3.17)), the sensitivity analysis of the vehicle fuel consumption shows an approximately linear relationship with the aerodynamic drag coefficient, for the range of values evaluated (Figure 5.21). The range of aerodynamic drag coefficients chosen span from 0.14, which is the best theoretical value that can be achieved by the TFC vehicle developed in [6], to a mediocre 0.3, easily achieved by many production cars.

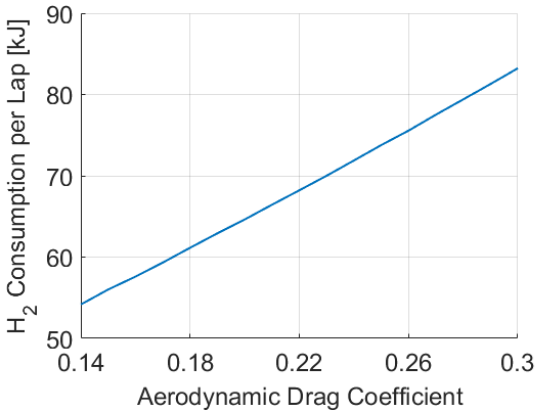

Figure 5.21 - Sensitivity analysis of the fuel consumption to the aerodynamic drag coefficient.

The analysis shows that the fuel consumption can be an expected increase approximately 14.5% per 0.05 increase in the aerodynamic drag coefficient, which goes to show how important it is to keep it as low as possible to be able to compete with other teams in terms of fuel efficiency.

6 Conclusions

From the get-go, one of the main realizations of this thesis is that, in efficiency competitions as matured as the Shell Eco-marathon is, the top performing teams have often been competing for many years or even decades and, with all the accumulated experience have developed highly optimized vehicles that can achieve astonishing fuel efficiencies. In this very competitive atmosphere, any small increment to the fuel efficiency that is obtained through the optimization of the many parts that make the vehicle can make the difference in the chase for higher fuel efficiencies.

Other than the actual efficiency of the vehicle, the main deciding factor that differentiates the teams that have the most success from the rest is the development of an efficient driving strategy around the track. When reading the reports and papers available from other teams, it was surprising to find that many teams neglect the driving strategy. The reasons for this vary from the lack of an accurate enough model of the vehicle or the lack of time to develop the strategy before the race.

The work developed in this thesis brings a new perspective to the development of high fuel efficient vehicles by combining the powertrain design and component selection process with the development of the optimum driving strategy. This method ensures that the powertrain of the vehicle is a perfect match for the driving strategy, which enables the vehicle to reach maximum fuel efficiency.

Vehicle Components

In the selection process, the main components that stood out are: the Horizon H-1000XP fuel cell, due to its very high efficiency and pedigree (several teams have competed with this fuel cell and won); the Dunkermotoren BG 95X80 BLDC motor, a high efficiency and versatile motor that will give the vehicle the means to overcome any track; the PLG 80 LB planetary gearbox from the same brand as the motor, a high quality component which ensures a perfect coupling to the motor and maximum efficiency; the DC-DC converter that stands between the FC and the motor should be as efficient as possible since it directly affects the performance of the vehicle; finally, the low rolling resistance Michelin tires purposefully made for the SEM, which are considered to be a must for any team aiming for the top spots.

One observation in relation to the motor is that, if there are no severe budget limitations for the vehicle, a PMSM should be preferred over a BLDC motor since these motors can achieve higher efficiencies, have better performances and higher energy densities. Although this difference should be minimal.

The SC and its DC-DC converter can be selected based on the performance requirements and budget available, since they don't affect the fuel efficiency nearly as much as the rest of the components.

Powertrain Design Considerations

Between the compared powertrain configurations, the parallel active hybrid proved to be the best choice. It has the advantage of allowing the FC to operate constantly at maximum efficiency, as opposed to the fuel cell active configuration, where the fuel cell output must meet the demands of the motor, lowering

the fuel consumption as a result. Other reasons for selecting the hybrid are its higher flexibility to respond to changing conditions in the track and/or during the race, as well as its potential to increase the fuel cell's operational life.

The implementation of the parallel active hybrid powertrain model proved to be a great success, not only does the model effectively estimate the minimum energy storage requirements of the supercapacitor but it also efficiently controls the energy flow inside the powertrain, ensuring that the SOC of the supercapacitor is the same at the end and at the start of the race, as mandated by the competition rules.

The selected powertrain configuration (PAH) has energy storage capabilities, enabling the use of regenerative braking. However, since the maximum energy available for regenerative braking is estimated to be lower than 3% of the total energy consumed by the electric motor (being even lower than 1% in a real scenario), it is not worth the investment due the added complexity and cost of the powertrain and the fact that it might even have the opposite of the desired effect on the fuel efficiency.

One other question that was answered in this work, specifically for SEM urban concept vehicles, is that having only one rear driving wheel was found to be the best drivetrain architecture because it is much simpler, cheaper, easier to build and maintain as well as being the most efficient configuration. The tire-road traction available at just the one rear wheel is estimated to be more than sufficient for both dry and wet conditions, assuming a concrete or asphalt road, and no tire slip is expected to occur.

Optimized Driving Strategy

For the considered vehicle specifications shown in Appendix M (average for the SEM competition) and the selected powertrain design, the final optimized driving strategy achieved a fuel efficiency of 370.2 km/m^3 of hydrogen. Taking into consideration that the selected vehicle specifications are conservative and can still be subjected to considerable optimization, the fuel consumption obtained proved to be excellent, being just 5% lower than the winning team of the SEM London 2016. It should be pointed out that in that year, the winning team achieved and impressive result of 389.3 km/m^3, which was 39% higher than the vehicle that placed in second.

In the optimal driving strategy, it was observed that the power demand of the BLDC motor was always very close to the optimum power output of the fuel cell for the highest efficiency. This occurs because it is more efficient to avoid the supercapacitor branch of the powertrain when possible, using it only to stabilize the power output of the fuel cell in its optimum point of operation;

Breaking down the energy consumption of the vehicle, it is interesting to point out that, even though the vehicle has a fairly low average velocity, the aerodynamic drag was still the major source of energy loss, responsible for approximately 21% of the hydrogen consumption, followed by the tire drag with 14% (1.5% caused by the cornering drag). However, the biggest and unavoidable source of energy loss was by far the efficiency of the fuel cell, which was responsible for around 43% of the energy lost.

Comparing the expected fuel efficiency of the driving strategy developed with the new Adaptive Sections strategy to a more basic average velocity strategy, the improvement in fuel consumption was minor (only around 4%). However, this is believed to be misleading because the developed model does not account

for the transient behaviour of the fuel cell and, since the average velocity driving strategy uses 25% more motoring sections, its fuel consumption is expected to increase due the transient effect on the fuel cell efficiency. Also, it was observed that the average velocity strategy was “lucky” in adapting its sections to the topography of track; there is no guarantee that the same will occur for different circuits.

In the development of the driving strategy it was observed that there is no benefit in increasing the number of motoring sections of the driving strategy to more than three, since the electric motor energy consumption remains basically the same.

Sensitivity Analysis

The study done on the sensitivity analysis of the fuel consumption to selected parameters concluded that the main factors that have the highest influence on the fuel efficiency of the vehicle are the rolling resistance of the tires, the efficiency of the primary DC-DC converter and the aerodynamic drag coefficient. The vehicle mass also affects the fuel consumption; however, this effect was considerably lower than what was expected. On the other hand, the efficiency of the supercapacitor and the temperature of the BLDC motor had little effect on the fuel efficiency.

With the sensitivity analysis in mind, it was concluded that if the values for any of the three main parameters that influence the fuel efficiency were slightly improved, the TFC vehicle could have easily surpassed the fuel efficiency of the winner of SEM London 2016 hydrogen Urban Concept class.

6.1 Recommendations for Future Work

The recommendations for future work are listed below:

- Development of a working dynamic model of the PEM fuel cell to complete the vehicle model;
- The construction of a laboratory testbench to run preliminary tests on the powertrain components to validate and fine-tune the powertrain models;
- When the vehicle is ready to be tested, a series of tests should be executed to validate and optimize the full vehicle model and to fine-tune the model’s parameters to improve accuracy;
- If costs are not a severe limitation for the project, the possibility of substituting the BLDC motor for a PMSM to improve performance should be evaluated;
- A thorough analysis on the rolling resistance of the acquired tires should be made to ensure that maximum performance is obtained. If the Michelin Urban Concept are unavailable, a study should be performed on other low rolling resistance non-flat profile tires. However, it should be noted that if the tire profiles used are non-flat, the cornering drag model might be inappropriate.

The work developed in this thesis accomplished all the proposed objectives. However, the greatest limitation of this thesis is the fact that it has been completely theoretical, i.e., no validation of any of the data or models used was done due the fact that, at the time of the writing of this thesis, TFC had no vehicle or components to do the necessary tests. This limitation is hoped to be surpassed when the team acquires all the equipment needed to do real tests to assess the validity of the models developed and the conclusion derived from them.

7 References

[1] European Commission, “Transport in the European Union - Current Trends and Issues,” 2019.

[2] European Environment Agency, “EEA greenhouse gas - data viewer,” *Jun. 2*, 2020. https://www.eea.europa.eu/data-and-maps/data/data-viewers/greenhouse-gases-viewer (accessed Oct. 07, 2020).

[3] Shell Eco-marathon, “Shell Eco-marathon 2021 Official Rules, Chapter 1.” 2020.

[4] B. Widera, “Renewable hydrogen implementations for combined energy storage, transportation and stationary applications,” *Therm. Sci. Eng. Prog.*, vol. 16, May 2020, doi: 10.1016/j.tsep.2019.100460.

[5] P. D. de Matos, “Metodologias Integradas de CAD , CAE e PDM para o Projeto de um Veículo de Competição,” M.S. thesis, Instituto Superior Técnico, Univ. Lisboa, Lisboa, 2020.

[6] C. A. Mesquita, “Projecto de um veículo eléctrico de competição movido a hidrogénio,” M.S. thesis, Instituto Superior Técnico, Univ. Lisboa, Lisboa, 2021.

[7] ECO-JÁNDULA Team, “Documentation for the pilot candidates to visualize the track (translated from Spanish),” *Nov. 25*, 2015. http://lince-jandula.blogspot.com/2015/11/documentacion-para-la-visualizacion-del.html (accessed Jan. 14, 2021).

[8] “Results and awards: Shell Eco-marathon,” *Make the Future*. https://www.shell.com/make-the-future/shell-ecomarathon/europe/results-and-awards/_jcr_content/par.html (accessed Jan. 15, 2021).

[9] M. M. Mench, *Fuel Cell Engines*. Hoboken, NJ: John Wiley & Sons, Inc., 2008.

[10] P. Corbo, F. Migliardini, and O. Veneri, *Hydrogen Fuel Cells for Road Vehicles*. London: Springer, 2011.

[11] IEA (2017), “World Energy Outlook 2017,” IEA, Paris, 2017. [Online]. Available: https://www.iea.org/reports/world-energy-outlook-2017.

[12] IEA (2016), “World Energy Outlook 2016,” IEA, Paris, 2016. [Online]. Available: https://www.iea.org/reports/world-energy-outlook-2016.

[13] J. Edmondson and A. Holland, “Materials for Electric Vehicles: Electric Motors, Battery Cells & Packs, HV Cabling 2020-2030,” IDTechEx, 2020.

[14] J. Larminie and A. Dicks, *Fuel cell systems explained*, 2nd ed. Chichester, UK: John Wiley & Sons Ltd, 2003.

[15] W. Liu, *Hybrid Electric Vehicle System Modeling and Control*, 2nd ed. Chichester, UK: John Wiley & Sons, Ltd, 2017.

[16] M. Ehsani, Y. Gao, S. Longo, and K. M. Ebrahimi, *Modern Electric, Hybrid Electric, and Fuel Cell*

Vehicles, 3rd ed. New York: Taylor & Francis Group, LLC, 2018.

[17] P. Yedamale and Microchip Technology Inc., “Brushless DC (BLDC) Motor Fundamentals.” Microchip Technology Inc., 2003.

[18] K. Krykowski, Z. Gałuszkiewicz, P. Gałuszkiewicz, J. Hetmańczyk, and D. Całus, “High-speed Permanent Magnet Brushless DC Motors, Properties and Prospective Applications,” *Prz. Elektrotechniczny*, vol. 95, no. 8, pp. 139–145, Aug. 2019, doi: 10.15199/48.2019.08.30.

[19] A. Kuperman and I. Aharon, “Battery-ultracapacitor hybrids for pulsed current loads: A review,” *Renew. Sustain. Energy Rev.*, vol. 15, no. 2, pp. 981–992, Feb. 2011, doi: 10.1016/j.rser.2010.11.010.

[20] C. Mi and M. A. Masrur, *Hybrid Electric Vehicles: Principles and Applications with Practical Perspectives*, 2nd ed. Hoboken, NJ: John Wiley & Sons Ltd., 2018.

[21] J. Libich, J. Máca, J. Vondrák, O. Čech, and M. Sedlaříková, “Supercapacitors: Properties and applications,” *J. Energy Storage*, vol. 17, no. June, pp. 224–227, 2018, doi: 10.1016/j.est.2018.03.012.

[22] A. Emadi *et al.*, *Advanced Electric Drive Vehicles*. New York: Taylor & Francis Group LLC, 2015.

[23] H. Zhang, D. Cao, and H. Du, *Modeling, Dynamics and Control of Electrified Vehicles*. Duxford, UK: Elsevier, 2018.

[24] J. G. Hayes and G. A. Goodarzi, *Electric Powertrain: Energy Systems, Power Electronics and Drives for Hybrid, Electric and Fuel Cell Vehicles*. Hoboken, NJ: John Wiley & Sons Ltd, 2018.

[25] M. Alaküla, K. Jonasson, C. Andersson, and B. Simonsson, “Hybrid Drive Systems for Vehicles - Part I: System Design and Traction Concepts.” Lund University, Lund, 2006.

[26] S. Dorel *et al.*, “Torque and Power-Velocity Relationships in Cycling: Relevance to Track Sprint Performance in World-Class Cyclists,” *Int. J. Sports Med.*, vol. 26, no. 9, pp. 739–746, Nov. 2005, doi: 10.1055/s-2004-830493.

[27] A. S. Gardner, J. C. Martin, D. T. Martin, M. Barras, and D. G. Jenkins, “Maximal torque- and power-pedaling rate relationships for elite sprint cyclists in laboratory and field tests,” *Eur. J. Appl. Physiol.*, vol. 101, no. 3, pp. 287–292, 2007, doi: 10.1007/s00421-007-0498-4.

[28] Michelin, “No need for speed as teams rely on Michelin tires to take top spots in shell’s super-mileage race,” *Apr. 29*, 2014. https://michelinmedia.com/speed-teams-rely-michelin-tires-top-spots-shells-super-mileage-race/ (accessed Jan. 14, 2020).

[29] L. Bertini, “Modeling and Optimization of a Fuel Cell Hybrid System,” M.S. thesis, KTH Royal Institute of Technology, Stockholm, 2011.

[30] J. Raychev, G. Hristov, P. Zahariev, and D. Kinaneva, “Design, Development and Evaluation of an Electric Urban Concept Vehicle Prototype Powered by a Hydrogen Fuel Cell,” Sep. 2018, doi: 10.1109/EAEEIE.2018.8534240.

[31] E. Grudic, “Electric Propulsion System for the Shell Eco-marathon PureChoice Vehicle,” M.S. thesis, Norwegian University of Science and Technology, Trondheim, 2008.

[32] B. D. Carlsen and O. J. Oma, “Development, Building and Competing with a New Car in Shell Eco-marathon,” M.S. thesis, Norwegian Univ. of Science and Technology, Trondheim, 2017.

[33] E. Grunditz and E. Jansson, “Modelling and Simulation of a Hybrid Electric Vehicle for Shell Eco-marathon and an Electric Go-kart,” M.S. thesis, Chalmers Univ. of Tech., Gothenburg, 2009.

[34] T. Liu, “Energy Management Strategy of a Hybrid Vehicle for Shell Eco-marathon,” M.S. Thesis, KTH Royal Institute of Technology, Stockholm, 2017.

[35] T. Liu, L. Feng, M. Hellgren, and J. Wikander, “Increasing Fuel Efficiency of a Hybrid Electric Competition Car by a Binary Equivalent Consumption Minimization Strategy,” in *IEEE International Conference on Automation Science and Engineering*, 2018, no. August, doi: 10.1109/COASE.2018.8560378.

[36] Green Team Twente, “The Car.” https://www.greenteamtwente.nl/car/ (accessed Jan. 10, 2021).

[37] T. D. Gillespie, *Fundamentals of Vehicle Dynamics*. Warrendale, PA: SAE International, 1992.

[38] SAE International, “SAE J670 JAN2008: Surface Vehicle Recommended Practice.” 2008.

[39] J. P. Pauwelussen, *Essentials of Vehicle Dynamics*. Oxford, UK: Elsevier Ltd, 2015.

[40] J. J. Santin *et al.*, *The World’s Most Fuel Efficient Vehicle: Design and Development of PAC-Car II*. Zürich: VDF Hochschulverlag AG an der ETH Zürich, 2007.

[41] H. B. Pacejka, *Tyre and Vehice Dynamics*, 2nd ed. Oxford, UK: Elsevier Inc., 2006.

[42] L. Nakuçi and A. Spahiu, “Saving Energy by Replacing IM with BLDC Motor in Fan Application,” *European Journal of Electrical Engineering and Computer Science*, vol. 2, no. 5, Aug. 2018.

[43] M. Zeraoulia, M. E. H. Benbouzid, and D. Diallo, “Electric motor drive selection issues for HEV propulsion systems: A comparative study,” *IEEE Trans. Veh. Technol.*, vol. 55, no. 6, pp. 1756–1764, Nov. 2006, doi: 10.1109/TVT.2006.878719.

[44] K. T. Chau and W. Li, “Overview of electric machines for electric and hybrid vehicles,” *Int. J. Veh. Des.*, vol. 64, no. 1, 2014, doi: 10.1504/IJVD.2014.057775.

[45] S. Derammelaere, M. Haemers, J. De Viaene, F. Verbelen, and K. Stockman, “A quantitative comparison between BLDC, PMSM, brushed DC and stepping motor technologies,” *2016 19th Int. Conf. Electr. Mach. Syst.*

[46] *Handbook for selection of motors*. Bonndorf, Germany: Dunkermotoren GmbH., 2018.

[47] Dunkermotoren GmbH, “Brushless DC motors.” https://www.dunkermotoren.com/en/products/brushless-dc-motors/ (accessed Feb. 18, 2021).

[48] S. Baldursson, “BLDC Motor Modelling and Control – A Matlab®/Simulink® Implementation,” M.S. thesis, Chalmers University of Technology, Gothenburg, 2005.

[49] Z. Meng, R. Chen, C. Sun, and Y. An, “The mathematical simulation model of brushless DC motor system,” in *2010 International Conference on Computer Application and System Modeling*, vol. 12, pp. 625–629, doi: 10.1109/ICCASM.2010.5622430.

[50] A. Tashakori, M. Ektesabi, and N. Hosseinzadeh, “Modeling of BLDC motor with ideal back-EMF for automotive applications,” in *World Congress on Engineering*, 2011, vol. 2, pp. 1504–1508.

[51] K. Krykowski, J. Hetmańczyk, Z. Gałuszkiewicz, and R. Miksiewicz, “Computer analysis of high-speed PM BLDC motor properties,” *COMPEL Int. J. Comput. Math. Electr.*, vol. 30, no. 3, pp. 941–956, May 2011, doi: 10.1108/03321641111110906.

[52] K. Krykowski and J. Hetmańczyk, “Constant Current Models of Brushless DC Motor,” *Electr. Control Commun. Eng.*, vol. 3, no. 1, pp. 19–24, Sep. 2013, doi: 10.2478/ecce-2013-0010.

[53] Toshiba, “120° Square-Wave Commutation for Brushless DC Motors.” Toshiba Electronic Devices & Storage Corporation, Aug. 03, 2018.

[54] T. Verstraten, R. Furnémont, G. Mathijssen, B. Vanderborght, and D. Lefeber, “Energy Consumption of Geared DC Motors in Dynamic Applications: Comparing Modeling Approaches,” *IEEE Robotics and Automation Letters*, vol. 1, no. 1, pp. 524–530, Jan. 2016.

[55] Dunkermotoren GmbH, “Motors | Gearboxes Controllers | 2020 Catalogue.” Bonndorf, Germany, pp. 78–79, 2020.

[56] T. V. Sarathkumar, M. Poornanand, and A. K. Goswami, “Modelling and Simulation of Electric Vehicle Drive Through SAEJ227 & EUDC Cycles,” *2020 IEEE Students’ Conf. Eng. Syst.*, Jul. 2020, doi: 10.1109/SCES50439.2020.9236717.

[57] Horizon Educational, “User Manual H-1000XP Fuel Cell System.” Aug. 05, 2013.

[58] J.-C. Olivier *et al.*, “Multiphysics Modeling and Driving Strategy Optimization of an Urban-Concept Vehicle,” *2015 IEEE Veh. Power Propuls. Conf.*, Oct. 2015, doi: 10.1109/VPPC.2015.7352981.

[59] M. Targosz, W. Skarka, and P. Przystałka, “Model-Based Optimization of Velocity Strategy for Lightweight Electric Racing Cars,” in *Journal of Advanced Transportation*, Jun. 2018, no. 4b, doi: 10.1155/2018/3614025.

[60] D. T. Manrique Espindola, “Real-time optimal control of a low consumption electric vehicle,” Ph.D. dissertation, Université de Lorraine, Nancy, 2014.

[61] S. Ferreira, “Desenvolvimento de software para simulação e otimização de consumo de veículos: Aplicação à Shell Eco-Marathon realizada em Londres,” M.S. thesis, Univ. da Beira Interior, Covilhã, 2017.

[62] S. M. H. S. Omar, N. M. Arshad, M. H. A. M. Fakharuzi, and T. A. Ward, “Development of an Energy Efficient Driving Strategy for a Fuel Cell Vehicle over a Fixed Distance and Average Velocity,” in *2013 IEEE Conference on Systems, Process & Control*, Dec. 2013, pp. 117–120, doi: 10.1109/SPC.2013.6735115.

[63] C. L. Bickel, “Optimizing Control of Shell Eco-marathon Prototype Vehicle to Minimize Fuel Consumption,” M.S. thesis, Fac. of Cali. Polytech. State Univ., San Luis Obispo, CA, 2017.

[64] R. Bellman, “The Theory of Dynamic Programming,” *Bull. Am. Math. Soc.*, vol. 60, no. 6, pp. 503–515, Nov. 1954.

[65] O. Sundstrom and L. Guzzella, “A generic dynamic programming Matlab function,” in *2009 IEEE Multi-conference on Systems and Control*, Jul., no. 7, pp. 1625–1630, doi: 10.1109/CCA.2009.5281131.

[66] Horizon Fuel Cell Technologies, “Horizon Fuel Cell - XP Series,” *10 Feb.*, 2014. https://www.horizonfuelcell.com/xp-series (accessed May 22, 2021).

[67] Transportation Research Board, “Tires and Passenger Vehicle Fuel Economy: Informing Consumers, Improving Performance,” Washington, D.C., 2006.

[68] D. Montone, “Temperature Effects on Motor Performance,” *Haydon Kerk Motion Solutions / Pittman Motors*. AMETEK Advanced Motion Solutions, 2014.

[69] A. Rohatgi, “WebPlotDigitizer,” *28 Nov.*, 2020. https://automeris.io/WebPlotDigitizer/.

[70] R. Álvarez Fernández, S. Corbera Caraballo, F. Beltrán Cilleruelo, and J. A. Lozano, “Fuel optimization strategy for hydrogen fuel cell range extender vehicles applying genetic algorithms,” *Renew. Sustain. Energy Rev.*, vol. 81, no. Part 1, pp. 655–668, Jan. 2018, doi: 10.1016/j.rser.2017.08.047.

[71] The MathWorks Inc, “Global Optimization Toolbox TM User’s Guide R2020a.” Natick, MA, Mar. 2020.

[72] K. Deep, K. P. Singh, M. L. Kansal, and C. Mohan, “A real coded genetic algorithm for solving integer and mixed integer optimization problems,” *Appl. Math. Comput.*, vol. 212, no. 2, pp. 505–518, Jun. 2009, doi: 10.1016/j.amc.2009.02.044.

Appendix A SEM Rules & Regulations

The most important rules and specifications to consider when developing a hydrogen urban concept are listed below in two sections; one for powertrain specific rules and the other more general rules.

A.1 Powertrain Regulations

- Maximum voltage must not exceed 48 Volts nominal or 60 Volts max;
- If an embedded electric storage device is part of the powertrain, it must be of capacitor type. Any other electric storage devices, like Pb, NiMh, and other types of batteries, are forbidden;
- The state of charge (SOC) of the supercapacitor (SC) will be checked before and after each run by measuring its voltage. If the voltage registered after the run is lower than the one at the start, the supercapacitor must be re-charged by running the fuel cell until the voltage is equal to the voltage registered before the run and the additional time required to recharge the SC is added to the recorded time of the relevant run;
- An accessory battery provides all allowed electrical needs such as safety devices (windscreen wipers, lights, hydrogen sensors, hydrogen relays and hydrogen shutdown valve);
- The fuel cell must run by itself. The electricity needed for temperature regulation, fan, compressor, electronic management system for the fuel cell and the electric motor must be supplied by the fuel cell or supercapacitor, and not by the accessory battery;
- If the accessory battery can be electrically isolated from the fuel cell output and, consequently, the electric motor, it can be used to start the fuel cell. If not, an external battery must be used on the starting line to start the fuel cell system;
- Oxygen for the fuel cell's operation must be obtained from the surrounding air;
- The vehicle must make use of a sole compressed hydrogen cylinder (cartridges and other means of hydrogen storage are not permitted). In Europe, a 1 L and a 0.4 L cylinder at 200 bar, weighing 2.57 kg and 1.4 kg, respectively, will be provided for the competition;
- The hydrogen system must be designed as follows:
  H_2 cylinder → Pressure regulator directly attached to the cylinder → Emergency shutdown valve directly attached to the outlet of the pressure regulator → Flow meter → Fuel Cell
- The flow meter must be fixed at the inlet of the fuel cell. Both must be at the same pressure.

The energy consumption results will be calculated bases on the hydrogen consumed, measured by the flow meter, plus the electrical energy consumed from accessory battery and the external starter battery (if used), measured by the joulemeter. Since the results are expressed in km/m^3 of hydrogen, the net calorific value[10] (NCV) of H_2 will be used to convert the electrical energy consumed, in Joules, to the equivalent volume of hydrogen at 15 ºC and 1 atm.

[10] The net calorific value (also known as lower heating value) is defined as the amount of heat released by the combustion of a fuel, assuming the latent heat of vaporization of water in the reaction products is not recovered.

A.2 Miscellaneous

Other information of interest is presented in this section:

- Maximum vehicle weight of 225 kg (without the driver);
- Fully equipped driver with a minimum weight of 70 kg (if the driver is not heavy enough, ballasts must be fitted to the vehicle to make up for the weight difference);
- At no point during the run can the vehicle go over the imposed speed limit of 40 km/h;
- Wet weather capability;
- A parking brake function is required to provide a brake force of at least 50 N (the brake can be embedded in the transmission);
- The vehicle must be equipped with a “dead man’s safety device” or sometimes referred to as “operator presence control”;
- A hydrogen sensor must be installed in the fuel cell compartment, near the main ventilation orifice on the top of the vehicle;
- Guards for transmission chains and/or belts are mandatory and all parts of the drive train must be within the confines of the body cover.

Appendix B SEM London 2016 Track Map

The Shell Eco-marathon Europe 2016 track elevation map is shown in Figure B1

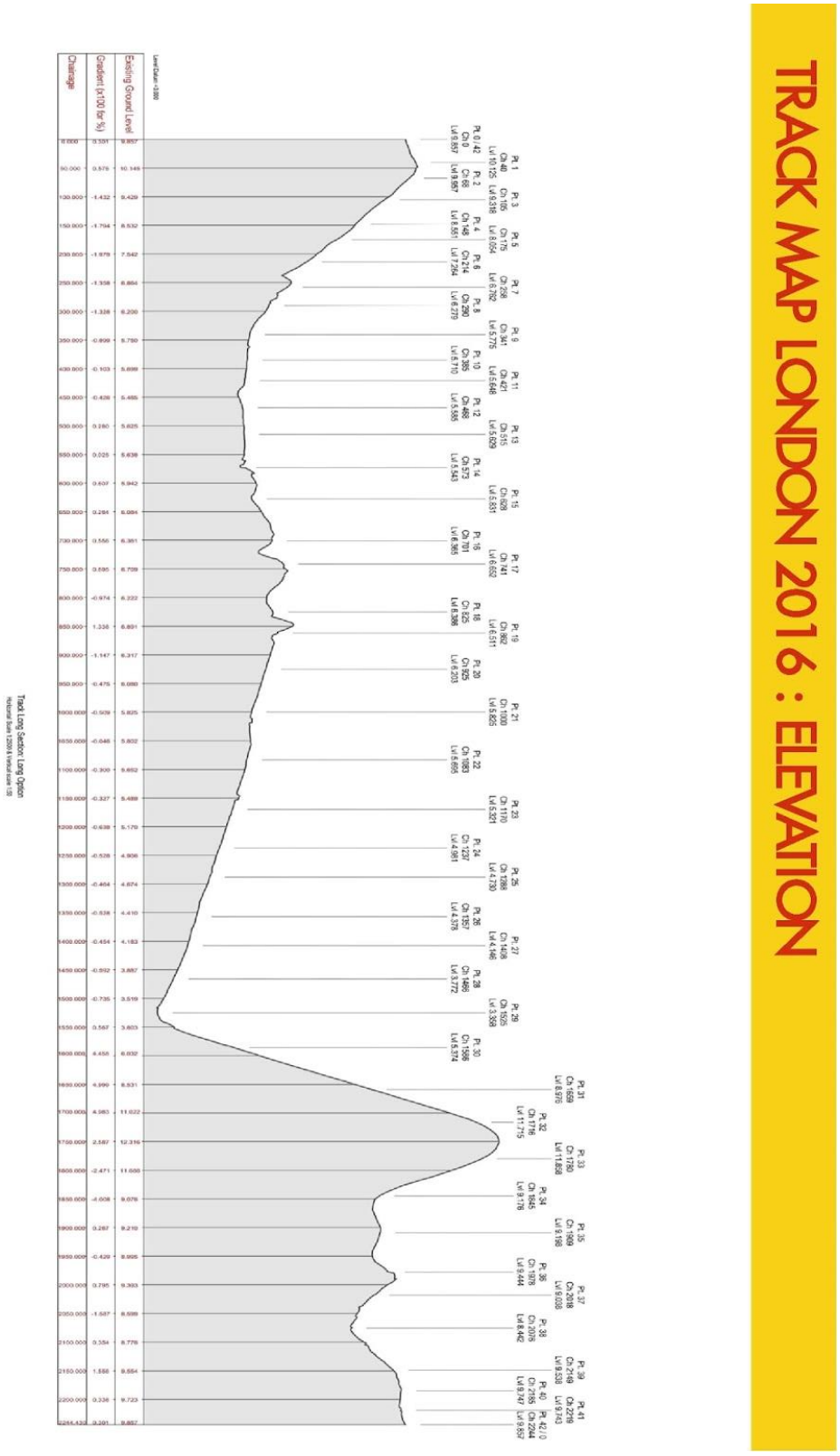

Figure B1 - Shell Eco-marathon Europe 2016: London elevation track map [7].

Appendix C Dynamics Theoretical Background

Describing the dynamics of a vehicle can be achieved in two ways; the empirical and the analytical. The empirical method is gaining knowledge of the factors that influence the vehicle performance by means of direct or indirect observation and trial and error. It is simple and does not require a deep understanding of the complex physical phenomena and mechanics behind the object of interest, but it can quite often lead to failure. For this reason, engineers avoid this method when possible and favour the analytical approach, which attempts to characterize the behaviour of the object by describing the mechanics of interest behind it, based on known laws of physics. The resulting analytical model can often be represented by a set of algebraic or differential equations that, in the case of a vehicle, relate the forces or motions of interest to control inputs and its characteristics, e.g., torque output, mass, tire properties, aerodynamic shape, to name a few. The model gives the opportunity to evaluate the role of each of the vehicle properties and components, and to use its predictive capabilities to identify the design characteristics required to reach the performance goals.

It must be noted that analytical models seldomly describe the real processes they intend to perfectly and only emulate the behaviours that are of interest to the functions they were designed for. This is because real situations are of extreme complexity and only in very controlled and simple experiments can models achieve an almost perfect description of reality. For this reason, to avoid errors and ultimately an ineffective model, it is essential to understand the assumptions and simplifications used when modelling the physical phenomena and to establish the conventions used in describing the motions, forces and all other relevant aspects.

C.1 Newton's Second Law

The fundamental law that most vehicle dynamics models start with is Sir Isaac Newton's second law. Applying Newton's Second Law is done by surrounding the object of interest in a boundary and applying the appropriate forces and moments on each point of contact with the outside world, as well as the forces that act on the centre of mass, i.e., gravitational and acceleration forces, forming a free-body diagram. This can be done for each of the three independent directions (x, y, z).

The law can be applied to both translational and rotational systems:

a. Translational Systems – The sum of the forces acting on a body along a direction is equal to the product of its mass and the acceleration in that direction.

$$\sum F_x = M \cdot a_x \tag{C1}$$

where:

F_x = Forces in the direction of x;

M = Mass of the body;

a_x = Acceleration in the direction of x.

b. Rotational Systems – The sum of the torques acting on a body about a given axis is equal to the product of its rotational moment of inertia and the rotational acceleration about that axis.

$$\sum T_x = I_{xx} \cdot \alpha_x \quad \text{(C2)}$$

where:

T_x = Torques about the x-axis;

I_{xx} = Moment of inertia about the x-axis;

α_x = Angular acceleration about the x-axis.

C.2 Lumped Mass

A vehicle is a complex mechanism of many moving parts, contained within an exterior envelope or body. However, when analysing its dynamic behaviour, one can often represent it as one lumped mass located at its centre of gravity[11] (CG), as all components move together (Figure D1). This is valid for acceleration, braking and most turning analyses; however, for ride analyses it is often necessary to treat the wheels and the vehicle body as separate lumped masses [37]. In this case, the lumped masses representing the wheels are named the “unsprung masses” and the one representing the vehicle’s body the “sprung mass”.

[11] In Mechanics, the centre of mass is the imaginary point in an object or system of objects where, for convenience in many calculations, one can assume the total mass is concentrated, as it is the point where any uniform force on the object or system acts. Assuming a uniform gravitational field, which is perfectly acceptable in most mechanics problems, the centre of mass and the centre of gravity are exactly the same point.

Appendix D Vehicle Coordinate System

The coordinate system used throughout this work is defined with reference to a right-hand orthogonal coordinate system. The vehicle-fixed and the earth-fixed coordinate systems can be seen in Figure D1 and Figure D2, respectively:

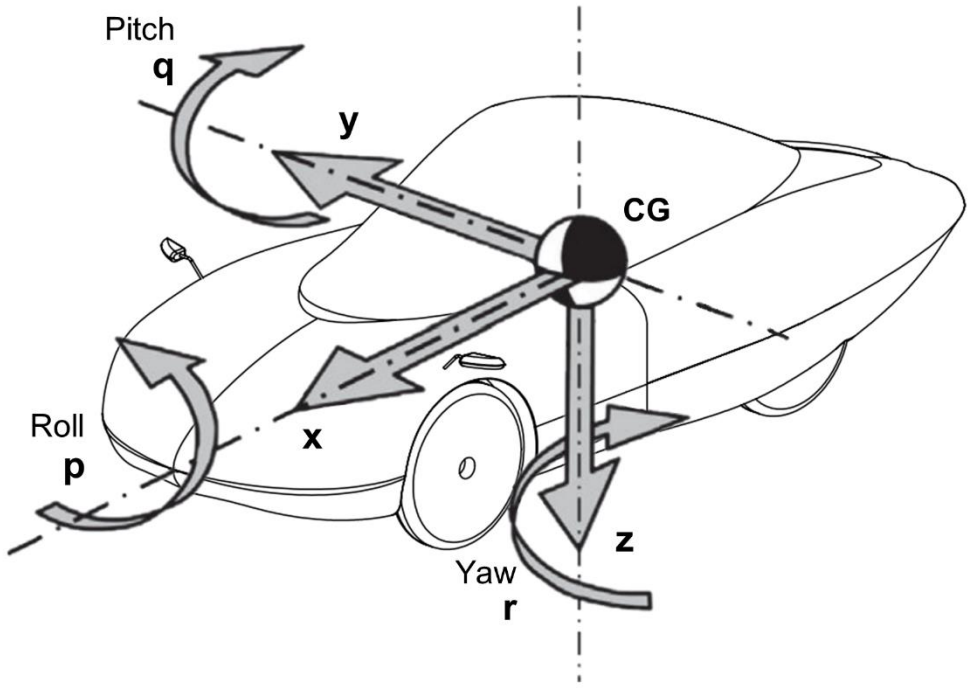

Figure D1 - SAE vehicle axis system [38], vehicle model from [6].

x - Forward and on the longitudinal plane of symmetry;
y - Lateral out the right side of the vehicle;
z - Downward with respect to the vehicle;
p - Downward with respect to the vehicle;
q - Pitch velocity about y axis;
r - Yaw velocity about the z axis.

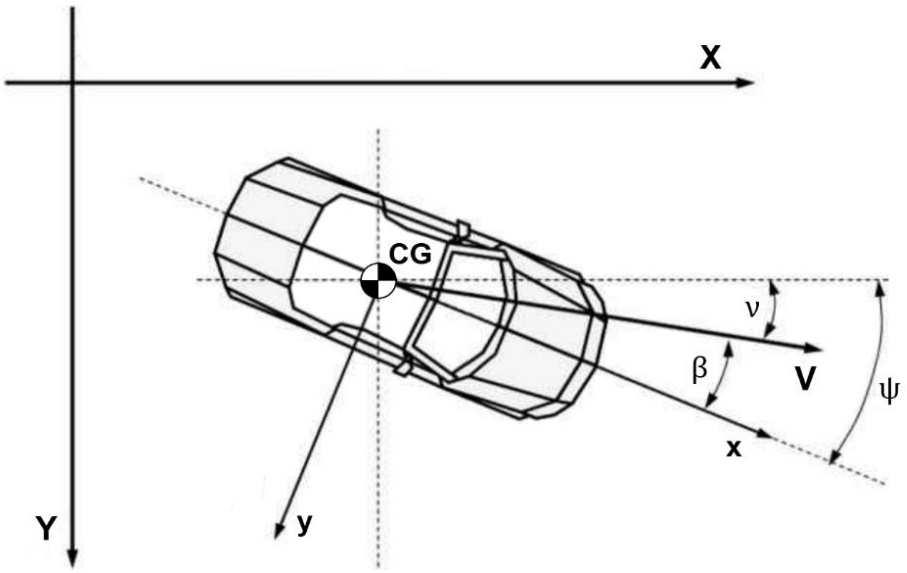

Figure D2 - Vehicle in an earth-fixed coordinate system, adapted from [39].

X - Forward travel;

Y - Travel to the right;

Z - Vertical travel (positive downward);

V - Projection of instantaneous velocity;

ψ - Heading angle (angle between x and X in the ground plane);

ν - Course angle (angle between the vehicle's velocity and X axis);

β - Sideslip angle (angle between x axis and vehicle velocity vector).

Appendix E Density Correction

Being the air density, ρ, dependant on the temperature, pressure and humidity, to estimate its value more precisely one can use the following expression, found in [37]:

$$\rho = 1.225 \cdot \frac{P_r}{101.325} \cdot \frac{288.16}{273.16 + T_r} \quad \text{(E1)}$$

where:

P_r = Atmospheric pressure in kPa;

T_r = Air temperature in ºC.

At standard sea-level pressure (1 atm) and 15 ºC, the density of air is equal to 1.225 kg/m^3.

Appendix F Magic Formula Coefficients

```
% Tire                   95 / 80 R 16 URBANCONCEPT
% Manufacturer           MICHELIN
% Infl. pressure (Pa)    400000
% Test speed (m/s)       10'
% Road surface           Safety walk'
% Road condition         Dry'

% [UNITS]
% LENGTH  = 'meter'
% FORCE   = 'newton'
% ANGLE   = 'radians'
% MASS    = 'kg'
% TIME    = 'second'

Fzn       = 588.6; %Nominal wheel load
CfRoll    = 0.002; %Rolling resistance coefficient

%[SLIP_ANGLE_RANGE]
ALPMIN    = -0.16; %Minimum valid slip angle
ALPMAX    = 0.16; %Maximum valid slip angle

%[VERTICAL_FORCE_RANGE]
FZMIN     = 14.0161; %Minimum allowed wheel load
FZMAX     = 702.914; %Maximum allowed wheel load

%[LATERAL_COEFFICIENTS]
PCY1      = 2.6757; %Shape factor Cfy for lateral forces
PDY1      = 0.9415; %Lateral friction Muy f
PDY2      = -0.1242; %Variation of friction Muy with load
PEY1      = 1.3904; %Lateral curvature Efy at Fznom
PEY2      = -0.4098; %Variation of curvature Efy with load
PEY3      = 0.0356; %Zero order camber dependency of curvature Efy
PKY1      = -77097.6066; %Maximum value of stiffness Kfy/Fzo
PKY2      = 6483.5045; %Load at which Kfy reaches maximum value
PKY4      = 2; %Generic value


%FORMULAS TO CALCULATE THE COEFFICIENTS OF MAGIC FORMULA

dfz       = (Fz/2-Fzn)/Fzn; %Load correction parameter
C         = PCY1;
u         = PDY1 + PDY2*dfz;
D         = u*Fz/2;
E         = (PEY1+PEY2*dfz)*(1-PEY3);
Ca        = PKY1*Fzn*sin(PKY4*atan((Fz/2)/(PKY2*Fzn))); %Cornering
%stiffness
B         = Ca/(C*D);
```

Appendix G Optimum Motor Technology Table

The table found in Dunkermotoren's "Handbook for selection of motors" [46] to select the optimum motor technology is shown below in Figure G1.

			Series-wound DC motor on DC grid	Shunt-wound DC motor on DC grid	Shunt-wound DC motor on DC gridwith start-up resistor	Permanent magent DC motor (GR) on DC grid	Permanent magent DC motor with pulse converter and open loop voltage control (GR)	Permanent magent DC motor with pulse converter and closed loop control (GR)	External excited DC motorwith power converter	Reluctance motor on frequency converterwith V/f-Control	Stepper motor with control device	Brushless DC motor (BG)with power electronics and open loop V-Control	Brushless DC motor with servo amplifier (BGE/DME)	Brushless DC motor (BG)with integrated power electronics dMove	Permanent magnet synchronous motor with sinusoidal commutation (BG) and integrated servo amplifier dPro	External excited synchronous motor with sinusoidal commuation and frequency converter	Capacitor motor on AC grid	Shaded pole motor on AC grid	Universal motor on AC grid	3-phase asynchronous motor on AC grid (DR)	3-phase asynchronous motor on AC gridwith soft starter (DR)	3-phase asynchronous motor on AC gridwith star-delta start-up (DR)	3-phase asynchronous motor on frequency converter with V/f-Control	3-phase asynchronous motor on frequency converter with vector control	3-phase asynchronous motor with servo frequency converter	3-phase asynchronous motor with slip ringson AC grid with resistor start-up
Exclusion criteria	Application																									
		Constant speed motor	x	x	x	x						x		x	x		x	x	x	x	x	x	x	x	x	x
	x	Variable speed motor					x	x	x	x	x	x	x	x	x	x								x	x	x	
		Servo motor						x	x	x	x		x	x	x											x	
	Power range																									
		< 100 W	x			x	x	x		x	x	x	x	x	x		x	x	x	x						
	x	< 1 kW		x	x	x	x	x	x	x	x	x	x	x	x		x		x	x	x	x	x	x	x	x
		< 50 kW		x	x	x	x	x	x	x			x		x	x					x	x	x	x	x	x
		< 500 kW							x							x						x	x		x	x	
		> 500 kW							x							x						x			x		
	Start-up																									
		Without or with low load	x	x	x	x	x	x	x	x	x	x	x	x	x	x	x	x	x	x	x	x	x	x	x	x	x
	x	With load	x	x	x	x	x	x	x			x	x	x	x	x								x	x	x	x
	Energieversorgungsnetz																									
	x	DC-grid	x	x	x	x	x	x		x	x	x	x	x	x									x	x	x	
		1-phase AC grid					x	x	x	x			x				x	x	x					x	x	x	
		3-phase AC grid					x	x	x	x			x			x					x	x	x	x	x	x	x
	Suitability																									
Performance criteria	Features																									
	10	Small size	1	1	1	4	4x10	4x10	1	2	2	5x10	5x10	5x10	5x10	3	2	2	2	2	2	2	2x10	2x10	3x10	3
	6	High speed accuracy and high dynamics	0	0	0	0	2x6	5x6	3	3	2	2x6	5x6	3x6	5x6	4	0	0	0	0	0	0	2x2	3x2	4x2	0
	2	Low grid disturbances	0	0	1	0	2x2	2x2	2	2	2	2x2	2x2	2x2	2x2	2	0	0	0	0	1	1	2x2	2x2	2x2	1
	4	Low cost	4	4	3	5	4x4	3x4	1	4	4	4x4	1x4	2x4	1x4	0	5	5	4	5	4	4	3x4	3x4	2x4	3
	8	Low complexity	4	5	4	4	3x8	2x8	2	3	3	4x8	1x8	3x8	2x8	1	5	5	5	5	4	4	3x8	2x8	0x8	4
	2	Long life time, low maintenance efforts	0	0	0	1	1x2	1x2	0	5	5	5x2	5x2	5x2	5x2	0	5	5	0	5	5	5	5x2	5x2	5x2	0
	Ranking						98	104				124	106	114	114								82	80	76	

Figure G1 - Dunkermotoren form for selecting the optimum motor technology [46]

Appendix H BLDC Motors Technical Data

The main specifications for selected BLDC motors are shown in Table H1.

Table H1 - Dunkermotoren BLDC motors technical data [47].

Technical Data	**BG 95X80**	**BG 95X40**	**BG 75X40**
Nominal voltage [V]	24	24	24
Nominal current [A]	47.2	33.3	21
Nominal torque [Nm]	2.44	1.7	1.09
Nominal speed [rpm]	3890	3940	3780
Maximum torque [Nm]	10	6.45	5
Nominal output power [W]	1000	701	431
Maximum output power [W]	3000	1819	860
No load speed [rpm]	4150	4400	4660
No load current [A]	4.2	2.8	1.76
Torque constant [Nm/A]	0.06	0.057	0.052
Phase resistance [ohm]	0.013/2	0.023/2	0.04/2
Phase inductance [oh]	0.037/2	0.067/2	0.25/2
Rotor inertia [gcm^2]	1890	950	437
Motor weight [kg]	5.1	3.5	2.2

Appendix I 120-degree Commutation BLDC

The phase currents, EMFs waveforms and electromagnetic torque production in an ideal BLDC motor (no induction) with square wave phase currents and a 120-degree commutation is shown in Figure I1.

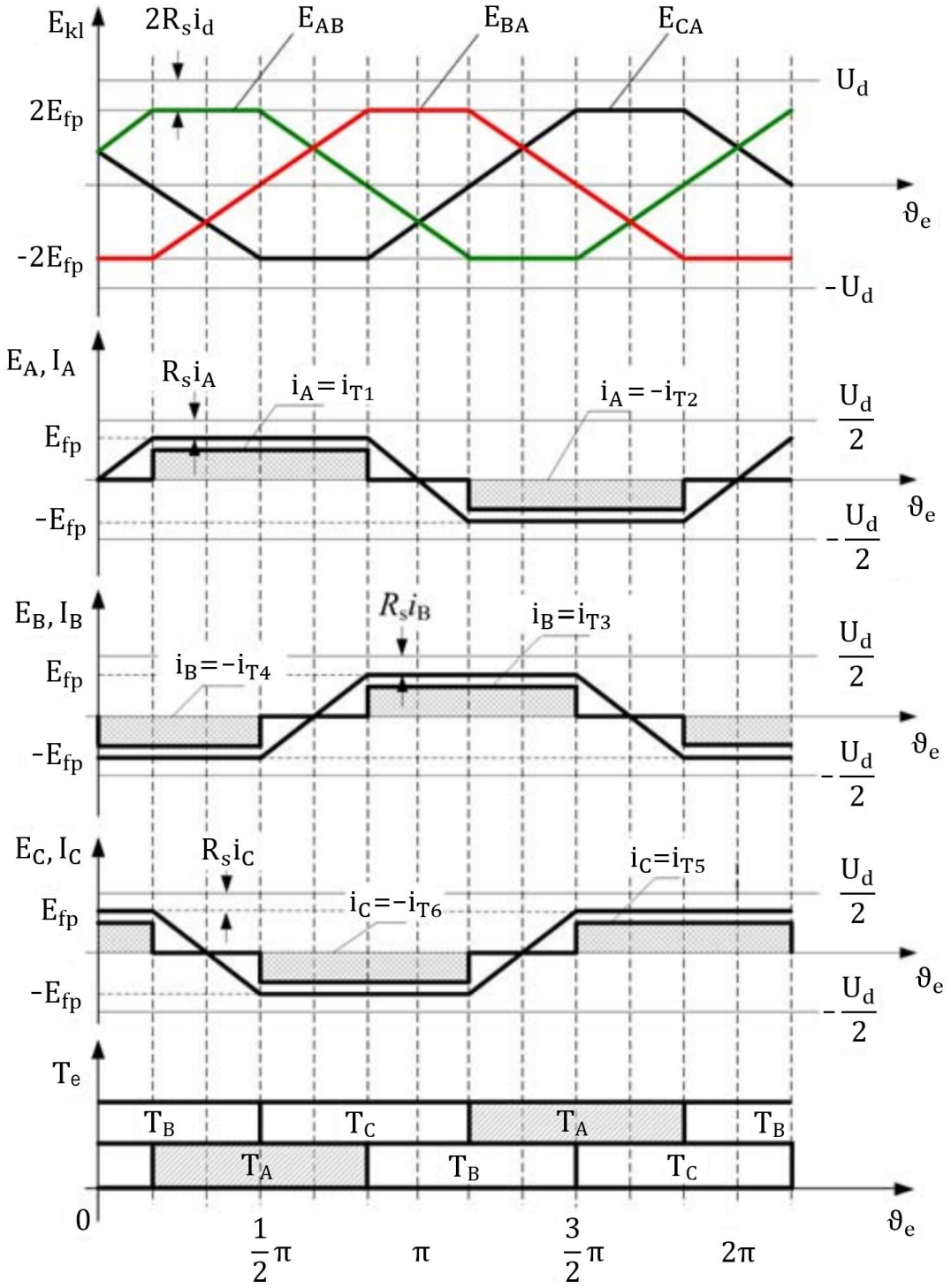

Figure I1 - Phase currents, EMFs waveforms and electromagnetic torque in an ideal BLDC motor with a 120-degree commutation.

Appendix J BLDC Motor Freewheel Current

The example of the freewheel effect in a BLDC motor between phases A and C is shown in Figure J1 and Figure J2. In the first figure both transistors 1 and 6 are open and the flow of current is “normal”; in the second figure the transistor 1 is closed and the flow continues through the diode 2.

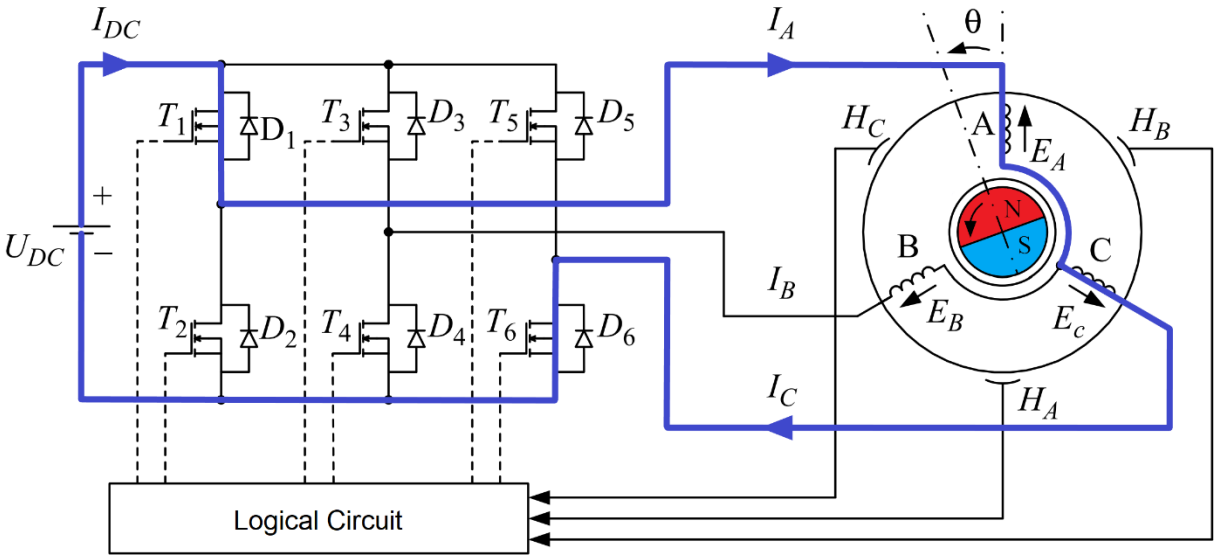

Figure J1 - Normal current flow (T_1 and T_6 open).

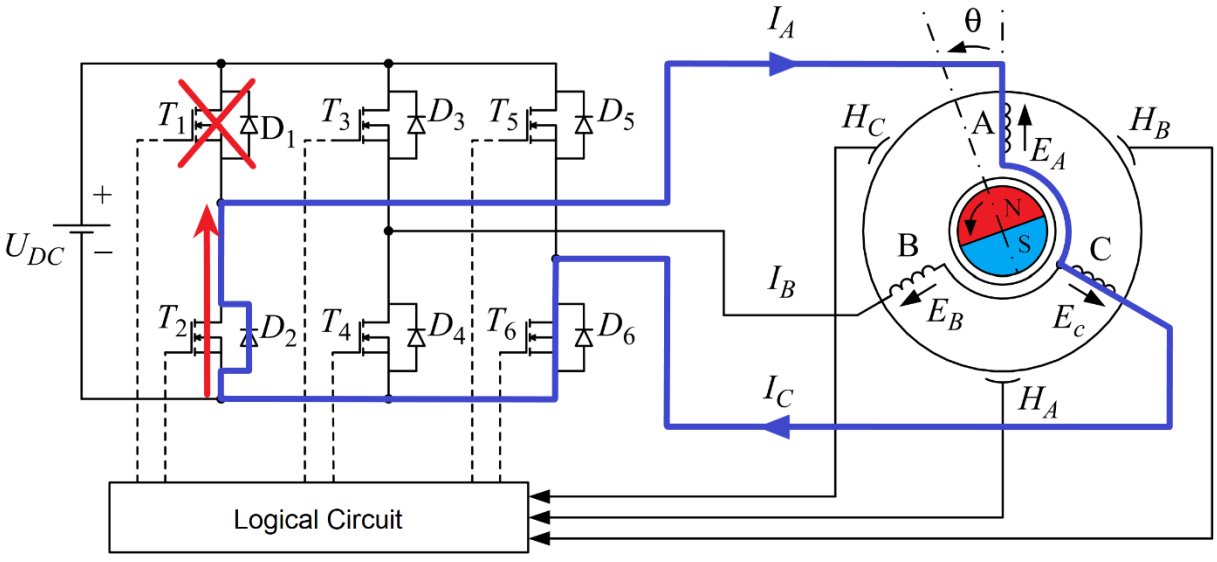

Figure J2 - Freewheel current flow (T_1 closed and T_6 open).

Appendix K Method to Model the Track

To obtain a sufficiently accurate model of the track, two variables, i.e., elevation and radius of turn, need to be determined as function of distance travelled. The first, and most consequential, is provided by the event's organization in the elevation map shown in Appendix B. For the second, since no data is given for the cornering radius along the track, it was determined using the method described in Section K.2.

K.1 Elevation Data

To extract the information from the topography map, the web based tool WebPlotDigitizer, an open source application excellent for extracting the underlying numerical data from plots, images and maps [69], was used. The elevation data was taken from the graph at every 4 metres and then transferred to MATLAB, where it was smoothed to eliminate small high-frequency height irregularities that could have been originated from the data extraction or measurement errors.

The data was then converted to the slope angle using basic trigonometry shown in Eq. (K1) and stored in a vector with slope values for every metre of the track.

$$\theta_i = \sin^{-1}\left(\frac{h_{i+1} - h_i}{x_{i+1} - x_i}\right) \tag{K1}$$

where:

θ_i = Slope at point i [rad];

i = Index of the point where slope is calculated (i+1 indicates the point after);

h = Height of the points;

x = Distance from the starting-line of the points.

In this case, since the data is collected for every metre, the distance on the track of every point is equal to its index minus one and the distance between points is always equal to one metre.

K.2 Cornering Radius Data

Considering that only Figure 1.5 is provided regarding the track route, it was used as the starting point to determine the cornering radius data. However, to extract any valid information it was necessary to determine its scale first, which was achieved using Google Earth and the "Image Overlay" tool.

The track map was overlayed and meticulously adjusted on the real location and two perpendicular lines of known length were drawn for reference, as seen in Figure K1.

Figure K1 - SEM London track map 2016, Google Earth overlay.

Afterwards, the image was exported to the WebPlotDigitizer, put to scale using the mentioned reference lines and, with its automatic extracting tool, the dataset of 177 points that defines the track was created with reference to XY coordinates (Figure K2). Some of the generated points were manually adjusted, mainly around the corners for a more efficient driving line (line that crosses all the points in the dataset).

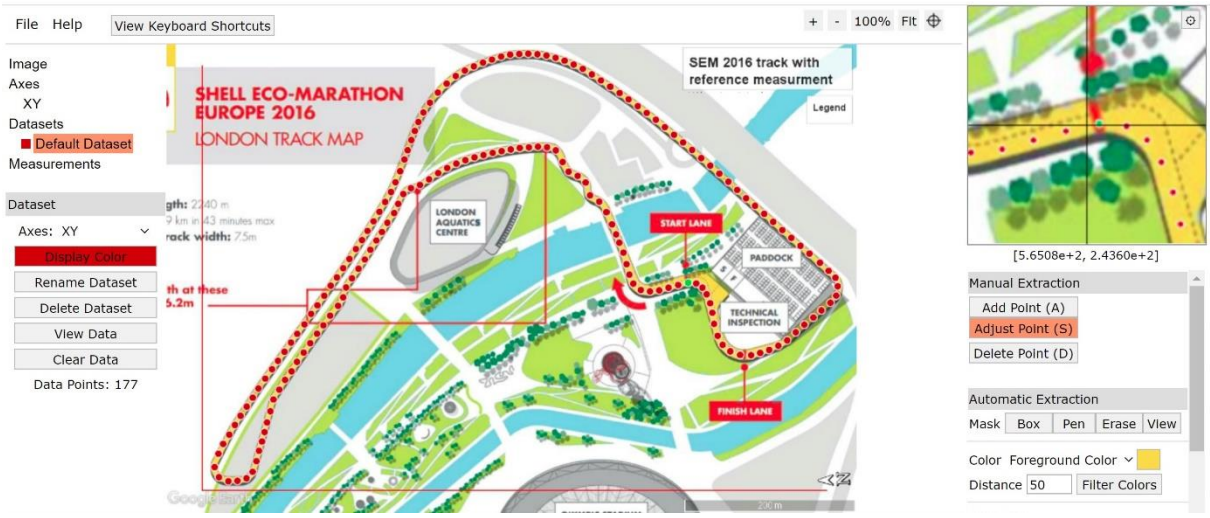

Figure K2 - SEM London track map 2016, data extraction with WebPlotDigitizer.

The resulting dataset was then processed in MATLAB, the data points were organized from start to finish-line and the distance of every point to the start-line, following the driving line, was calculated by summing the segments of length between all the previous points (Eq. (K2)). The length of each segment can be determined applying Pythagoras' Theorem, as seen in equation (K3).

$$L_{1,n} = \sum_{j=1}^{n} L_{j,j+1} \tag{K2}$$

$$L_{j,j+1} = \sqrt{\left(X_j - X_{j+1}\right)^2 + \left(Y_j - Y_{j+1}\right)^2} \tag{K3}$$

where:

$L_{1,n}$ = Distance of point n to the start-line;

$L_{j,j+1}$ = Length of the segment between points j and j+1;

X_j = Horizontal coordinate of point j on the track map;

Y_{j+1} = Vertical coordinate of the point after point j on the track map.

Lastly, to find the radius of turn of each point a system of three equations must be solved for every point, using its XY coordinates and the ones from the points immediately before and after, as seen below:

$$\begin{cases} (X_{j-1} - X_C)^2 + (Y_{j-1} - Y_C)^2 = {R_j}^2 \\ (X_j - X_C)^2 + (Y_j - Y_C)^2 = {R_j}^2 \\ (X_{j+1} - X_C)^2 + (Y_{j+1} - Y_C)^2 = {R_j}^2 \end{cases} \quad \text{(K4)}$$

where:

R_j = Cornering radius of point j;

X_C = X coordinate of the centre point of the circle that forms the turn;

Y_C = Y coordinate of the centre point of the circle that forms the turn;

Appendix L Genetic Algorithm

Genetic algorithms are adaptive heuristic search algorithms based on the biological evolution principles of natural selection and genetics [70]. In GAs, a population of potential solutions, known as individuals or chromosomes, “evolves” towards an optimal solution over consecutive generations, through simulated processes of survival of the fittest, reproduction and mutation, until a stopping criterion is met.

The main three types of rules used to create the next generation from the current population are [71]:

- **Selection rules**: The fittest individuals have a higher change of being selected as parents, contributing to the population of the next generation (the individuals with the best fitness values automatically survive to the next generation as elite children);
- **Crossover rules**: Pairs of parents are combined to form children for the next generation;
- **Mutation rules**: Changes are applied at random to individual parents to form children.

In the reproduction process, new individuals (children) are generated using crossover and mutation operators. The crossover operator mixes the genes of the parents to explore the search space, while the mutation operator maintains an adequate population diversity to avoid premature convergence [72].

In the case of a Mixed Integer GA Optimization algorithm, the only distinction lies in the methods used to generate a new population, namely the crossover and mutation operations which are required to create new individuals whose genes, i.e., the decision variables, are integer values.

For the driving strategy optimization problem proposed, the GA individuals have the structure of the duty cycle vector shown in Eq. (5.13). The number of genes, i.e., the number of decision variables, of an individual is equal to three times the number of active sections N minus two (13 for a five section OP).

For a more effective use of the genetic algorithm for integer problems (Mixed Integer GA), MATLAB’s guide for the algorithm [71] suggests a new set of parameters for integer optimization problems with a high number of decision variables (more than 10). The new tweaked set of parameters proved to be very effective at generating consistent, nearly identical solutions for the OP, which gives confidence that the solutions generated by the algorithm are very close to the global optimal.

The flowchart for the genetic algorithm used is shown in Figure L1.

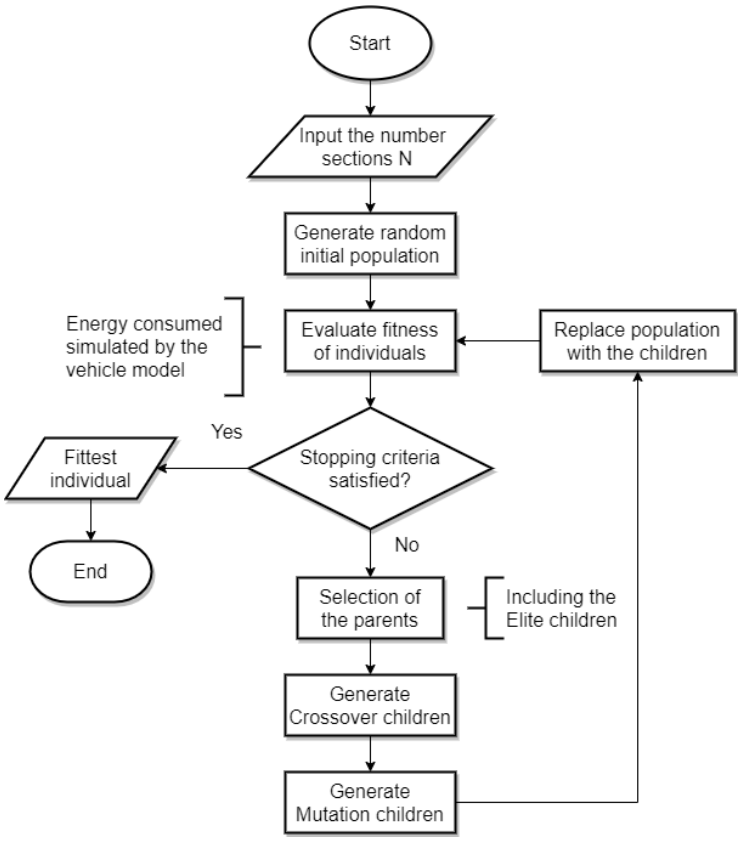

Figure L1 – Genetic Algorithm flowchart for the OP.

Appendix M Vehicle Specifications

The specifications used for the vehicle dimensions and aerodynamics are based on a colleague's master thesis on the aerodynamics of the same car. Other specifications used are based on real components or general approximated values. The values are shown below in Table M1.

Table M1 - Vehicle specifications used for the simulations and driving strategy optimization.

Specifications	**Value**
Mass of the Vehicle[1]	100 kg
Mass of the Driver	70 kg
Wheelbase[1]	1.57 m
Track Front Wheels[1]	1.00 m
Track Rear Wheels[1]	0.80 m
Height of the CG[1]	0.343 m
Rear Wheel to CG[1]	0.587 m
Aerodynamic Drag Coefficient[1]	0.18
Frontal Area of the Vehicle[1]	0.9 m^2
Radius of the Wheel[2]	0.275 m
Rolling Resistance Coefficient[2]	0.002
DC-DC Converter Efficiency	90 %
Supercapacitor Efficiency	95 %
Gearbox Efficiency[3]	97 %
Chain Transmission Efficiency	90 %

[1] Values used from a colleague master thesis [6];

[2] Michelin SEM Urban Concept tires;

[3] Dunkermotoren PLG 80 Planetary gearbox [55].